

Growth of 2D silicon structures by molecular beam epitaxy

Doctoral Thesis of
Daniele Nazzari, M.Sc

Supervisor:
Ao.Univ.Prof. Dipl.-Ing. Dr.techn. Alois Lugstein

Institute of Solid State Electronics
Technische Universität Wien



Die approbierte gedruckte Originalversion dieser Dissertation ist an der TU Wien Bibliothek verfügbar.
The approved original version of this doctoral thesis is available in print at TU Wien Bibliothek.

Statutory declaration

I declare that I have authored the present work independently, according to the code of conduct, that I have not used other than the declared sources and that I have explicitly marked all material which has been quoted either literally or by content from the used sources. This work was not yet submitted to any examination procedure neither in Austria, nor in any other country.

Erklärung zur Verfassung der Arbeit

Hiermit erkläre ich, dass die vorliegende Arbeit gemäß dem Code of Conduct - Regeln zur Sicherung guter wissenschaftlicher Praxis - ohne unzulässige Hilfe Dritter und ohne Benutzung anderer als der angegebenen Hilfsmittel, angefertigt wurde. Die aus anderen Quellen direkt oder indirekt übernommenen Daten und Konzepte sind unter Angabe der Quelle gekennzeichnet. Die Arbeit wurde bisher weder im In- noch im Ausland in gleicher oder in ähnlicher Form in anderen Prüfungsverfahren vorgelegt.

Vienna, January 2021

.....
Daniele Nazzari

Abstract

The continuously expanding portfolio of 2D materials represents a precious set of building blocks for engineering next generation electronic and optical devices.

A recent addition to this family is represented by silicene, the 2D allotrope of silicon. This material is characterised by a structure similar to the one of graphene, showing a hexagonal arrangement of Si atoms, albeit slightly buckled out of plane.

This new, synthetic material combines an ultrahigh carrier mobility with the unique opportunity to tune its band gap by applying an external electric field. For these reasons it could be exploited to realise field effect transistors with a two-dimensional channel.

Silicene still remains a vastly unexplored material: to fully unleash its potential, it is crucial to acquire additional knowledge regarding its chemical and physical properties as well as optimised growth processes and substrates. Furthermore, it is of pivotal importance to develop and investigate processes that allow to integrate this 2D material in functional devices.

In this thesis, the well-known growth of silicene on Ag(111) is firstly replicated. The grown layer is thoroughly analysed by means of low energy electron diffraction, X-ray photoemission spectroscopy, angle resolved UV photoemission spectroscopy and low energy electron microscopy.

Additionally, a novel method for encapsulating silicene and protecting it from oxidation is developed: the 2D layer is capped, directly in-UHV, by exfoliated few-layer graphene or hBN flakes, enabling the utilisation of *ex situ* analysis tools, such as Raman spectroscopy and spectroscopic ellipsometry. The vibrational properties of silicene are studied, with particular focus on the polarisability properties, which strictly reflect the two-dimensional nature of the grown layers.

In the second part, the growth of silicene on Au(111) is explored. By using a combination of LEED, LEEM, ARUPS and Raman analysis, as well as first principle calculations, the grown layer is fully characterised, showing that it comprises a highly biaxially strained silicene phase. This offers a powerful new platform for future investigations of the effects of strain in 2D silicon-based materials.

In the final part of the thesis, CaF₂ is epitaxially grown on silicene/Ag(111), to study the possibility of engineering a gate insulation layer to efficiently control the flow of carriers through the two-dimensional material.

The presented data show that CaF₂ grows well on silicene, forming an ordered structure and maintaining its insulating properties. At the same time, silicon atoms in the silicene layer do not change their chemical state due to the presence of CaF₂. Raman spectroscopy data reveal that the buried silicene layer undergoes a structural modification, due to the presence of the insulating layer, nevertheless maintaining a 2D configuration. It is shown that the modified silicene layer possesses an enhanced optical absorption in the visible range, if compared to crystalline-diamond or amorphous silicon thin layers. The results pave the way for combining CaF₂ and silicene in next-generation electronic devices.

Acknowledgments

Firstly, I would like to thank my supervisor, Alois Lugstein, for giving me the opportunity of working on such an exciting topic. Through these years, he has always been ready to help me to overcome all the scientific obstacles and problems that I had to face, promoting a constructive dialogue. I would also like to thank him for the wonderful working environment that he was able to build in his lab, always permeated by a positive attitude, with friendly and helpful coworkers.

Speaking of coworkers, I would like to thank Jakob Genser and Viktoria Ritter for the wonderful time that we spent working together. These guys were incredibly helpful and always supportive, even in the worst moments - yes, I am talking about the cleanroom move! It has been very important for me to have the company of such motivated colleagues thorough the whole time.

But the group does not end here! Special thanks also to Masiar Sistani and Max Bartmann for all the technical help as well as for the chats and laughs - and obviously for all the beers! Also, thanks to A. M. Andrews and W. Schrenk for the precious technical help! Thanks to R. Rurali and M. Kolibal for the scientific discussions and fruitful collaboration. A special thanks goes to Emmerich Bertagnolli and to Gottfried Strasser for building such a inspiring and supporting environment at the institute. Also thanks to Walter Weber, for all the precious advices and for having brought new energy and motivation to the institute.

None of this would have been possible if I wouldn't have had the luck of being supported by my amazing family. They were always there for me, allowing me to always follow my dreams and always being close in the spirit, despite the physical distance. For this, grazie davvero Ma, Pa e Ale.

Lastly, but just because it is the most important element on this list, I would like to thank the person that, since 10 years, has always accompanied me along many adventures. Alessia, you have been truly the cornerstone of everything good that happened to me in these last years and for this I cannot thank you enough. This work was made it possible by your continuous support, help, dialogue and love. From the bottom of my heart, truly thank you.

Contents

Introduction	1
1 Theory	3
1.1 2D materials	3
1.1.1 Silicene	6
1.2 Raman Spectroscopy	14
1.3 Photoemission Spectroscopy	17
1.4 Low Energy Electron Diffraction	20
2 Experimental Methods	23
2.1 Molecular Beam Epitaxy	23
2.2 Raman Spectroscopy	26
2.3 Photoemission Spectroscopy	27
2.4 Low Energy Electron Diffraction	31
2.5 Low Energy Electron Microscopy	32
2.6 Growth Parameters	33
2.6.1 Temperature Control	33
2.6.2 Evaporation Rate	35
2.6.3 Base Pressure and Substrate Preparation	36
2.7 <i>In Situ</i> encapsulation	38
3 Results and Discussion	41
3.1 Silicene on Ag(111)	41
3.1.1 Epitaxial Growth	41
3.1.2 Photoemission Spectroscopy Measurements	49
3.1.3 Vibrational Properties	53
3.2 Silicene on Au(111)	55
3.2.1 Epitaxial Growth	55
3.2.2 Vibrational Properties	60
3.2.3 Photoemission Spectroscopy Measurements	65
3.3 Integration of Silicene and Calcium Fluoride	71
3.3.1 Epitaxial Growth	72
3.3.2 Photoemission Spectroscopy Measurements	74
3.3.3 Vibrational Properties	77
3.3.4 Optical Properties	78

4 Summary and Outlook	81
List of abbreviations	86
Appendix	88
MATLAB script for ARUPS data	88
Bibliography	105
Curriculum Vitae	106

Die approbierte gedruckte Originalversion dieser Dissertation ist an der TU Wien Bibliothek verfügbar.
The approved original version of this doctoral thesis is available in print at TU Wien Bibliothek.

List of Figures

1.1	Examples of 2D materials	4
1.2	Freestanding silicene's unit cell and band structure	6
1.3	Phonon dispersion curves for freestanding silicene	7
1.4	Band structure of graphene near Fermi level	9
1.5	DFT calculations of freestanding silicene's band structure	10
1.6	Silicene phases on Ag(111)	11
1.7	Formation energy of silicene phases on Ag(111)	13
1.8	Schematic representation of a Raman process	14
1.9	Schematic representation of a photoemission spectroscopy experiment . . .	17
1.10	Examples of LEED signals	20
2.1	Photo of UHV system and its main components	24
2.2	E-beam evaporator	25
2.3	WITEC Raman setup	26
2.4	X-ray source	27
2.5	Phoibos 150 spectrometer	28
2.6	ARUPS measurements setup	30
2.7	ErLEED 1000A apparatus	31
2.8	P90 LEEM Microscope	32
2.9	Photo of sample mounting configuration	34
2.10	Ellipsometry measurements for the calibration of the evaporation rate . . .	35
2.11	Ag(111) surface during the cleaning process	37
2.12	Tape preparation for the encapsulation process	39
2.13	Optical and AFM images of few-layer hBN and graphene flakes encapsulating silicene	39
3.1	LEED patterns of silicene phases on Ag(111)	43
3.2	LEEM micrograph of silicene growth on Ag(111) at 260°C	44
3.3	LEEM micrograph of silicene growth on Ag(111) at 300°C	45
3.4	LEED pattern of 3 ML silicene grown on Ag(111)	46
3.5	LEEM micrographs of silicene growth prolonged above 1 ML coverage . . .	47
3.6	XPS spectrum of 1 ML silicene on Ag(111)	49
3.7	ARUPS scan of 1 ML silicene on Ag(111)	51
3.8	Raman spectra of silicene on Ag(111)	53
3.9	LEED pattern of a Au(111) substrate	56

3.10	LEED pattern of 1 ML silicene on Au(111) confronted with different simulated diffraction patterns	57
3.11	Silicides' unit cells	58
3.12	Raman spectra of silicene grown on Au(111)	61
3.13	First-principle calculations of the Raman response of 1 ML silicene grown on Au(111)	64
3.14	XPS spectrum of 1 ML silicene on Au(111)	65
3.15	ARUPS scan of 1 ML silicene grown on Au(111)	68
3.16	Representation of biaxially strained silicene on Au(111)	70
3.17	Representation of the fluorite structure and of a possible interface between CaF ₂ and silicene	71
3.18	LEED patterns for CaF ₂ grown on 1 ML silicene on Ag(111)	73
3.19	XPS spectrum of silicene covered by CaF ₂	74
3.20	UPS spectrum of CaF ₂ grown on silicene on Ag(111)	76
3.21	Raman spectra of 1 ML silicene covered by CaF ₂	77
3.22	Ellipsometry measurements of 1 ML silicene covered by CaF ₂ and the derived absorbance	80

Introduction

The success of the semiconductor industry has been directly connected to the capability of constantly scaling the components in integrated circuits. In 1965, Gordon Moore, director of research at Fairchild Semiconductor and later co-founder of Intel Corp., famously predicted that this would lead to the doubling of the density of the components every 18 months [1]. This forecast proved correct for more than 50 years, making it one of the most important technological prediction of the last half-century. A constant increase in the components' density steadily reduced their performance-to-cost ratio, fostering the adoption of integrated circuits in many everyday-life objects and rapidly boosting the industry. As an example, in 1954 the average selling price of a transistor was 5.52 \$. Fifty years later, in 2004, this had dropped to a billionth of a dollar. This process has, undoubtedly, fuelled the prosperity of the last 50 years.

Moore's law is, however, bound to fail: the capacity of doubling the number of components is strictly dependent on the technological capability of scaling - i.e. reducing - the components' dimensions. The fabrication of FETs with gate lengths smaller than 10 nm proved to be extremely challenging, as indicated by the long delayed delivery of the latest Intel 10-nanometer chip generation. A further reduction of the critical dimensions of the components of integrated circuits down to the 5 nm node might be out of reach, unless more disruptive routes are considered.

The use of two-dimensional (2D) structures could prove essential to achieve this goal [2]. A single layer of graphene, the firstly isolated and most studied 2D material, appear to be inappropriate, due to the lack of a bandgap. After graphene, many other 2D materials have been proposed, isolated, synthesised and analysed. Within this large family, the 2D allotrope of silicon, commonly referred as silicene, has attracted great attention. This 2D material, experimentally observed for the first time in 2012 [3], is predicted to possess an extremely high carrier mobility as well as a linear band dispersion near the Fermi level, forming a Dirac cone [4]. Most importantly, silicene is expected to show a sizeable bandgap, induced by a strong spin orbit interaction [5]. Its bandgap can be tuned through the application of an external electric field [6], making it a promising material for the realisation of an atomically-thin transistor channel. Early reports proved the feasibility of this approach, showing the realisation of a silicene-based transistor working at room temperature, albeit showing drastically lower carrier mobilities compared to the theoretical expectations [7]. Silicene is also expected to show quantum spin Hall effect [8], chiral superconductivity [9] and giant magnetoresistance [10].

Silicene still remains a vastly unexplored material. To fully unleash its potential, it is crucial to acquire additional knowledge regarding its chemical and physical properties as well as optimised growth processes and substrates. Furthermore, it is of pivotal importance to develop and investigate processes that allow to integrate this 2D material in functional devices.

This work presents a comprehensive study on the growth of silicene by Molecular Beam Epitaxy (MBE). The 2D material is grown by e-beam evaporation of Si in an Ultra High Vacuum (UHV) environment and analysed using a large set of techniques, including Low Energy Electron Diffraction (LEED), X-ray and UV Photoemission Spectroscopy (XPS, UPS), Angle Resolved UV Photoemission Spectroscopy (ARUPS) and Raman Spectroscopy. By combining the results of all these different techniques, as well as first-principles calculations, it was possible to obtain a precise description of the structural, chemical and electrical properties of the grown layers, with particular focus on those properties that are most influenced by the two-dimensionality of the material and by the interaction with the growth substrate.

In the first chapter of this thesis a succinct introduction to the world of 2D materials is given, with the main focus on the structure and properties of silicene. The second chapter describes the experimental setup used in this work. The main results are presented and discussed in the third chapter, subdivided in three sections: in the first, the growth of silicene on Ag(111) is discussed. Different epitaxial processes are examined, for different growth temperatures and coverages. The chemical, electrical and structural properties of the grown layer are measured. In the second one, a different substrate is used: Au(111). By combining diffraction techniques with Raman spectroscopy measurements and first-principles calculations, the structure of the grown layer is revealed. Additionally, its band structure and chemical properties are analysed by ARUPS and XPS. Finally, a novel process for the realisation of an ultra-thin gate dielectric layer on silicene, based on crystalline CaF₂, is presented. The dielectric material is grown directly on silicene by MBE methods and the properties of the silicene-CaF₂ stack are characterised through a combination of LEED, XPS, UPS, Raman and Ellipsometry techniques. In the final chapter of the thesis, a recapitulation of the main results is given, as well as an outlook on the next questions that need to be answered in future works.

Chapter 1

Theory

1.1 2D materials

The quest for the exploration of the atomically-small world of 2D materials was certainly inspired by the famous lecture "There's plenty of Room at the Bottom" by Nobel laureate Richard P. Feynman [11]. In this lecture, the American physicist proposed the following question "What could we do with layered structures with just the right layers?".

2D materials are certainly the ultimate example of how thin a *layer* can be. These structures are characterised by extended crystalline planes composed by strongly covalently bonded atoms, thus truly being just 1 atom or molecule thick. Most of the experimental research on 2D materials stems from the first successful isolation of a layer of sp^2 hybridised carbon atoms, graphene, reported in 2004 by the group of A. Geim [12] and obtained by mechanical exfoliation. This remarkable result proved that 2D materials were something more than theoretical constructs and that they could be isolated despite the predicted thermodynamic instability of two-dimensional systems [13, 14].

At present, the portfolio of 2D materials has been vastly expanded, including both exfoliated and newly synthesised materials, which do not occur naturally. Additionally, many more materials are expected to be stable in a two-dimensional form [15]. The 2D materials group include all those materials that are developing along a plane and where the thickness is limited to the atomic or molecular level.

Among these materials, it is possible to find structures with very different electrical properties. One can identify semimetals (e.g., graphene), metals (e.g., NbS_2 , VSe_2), semiconductors (e.g., MoS_2 , WS_2 , silicene, germanene), insulators (e.g., HfS_2 , h-BN) and even materials displaying superconductivity (e.g., $NbSe_2$, TaS_2), just to name a few.

At the same time, 2D materials are characterised by rather different structures.

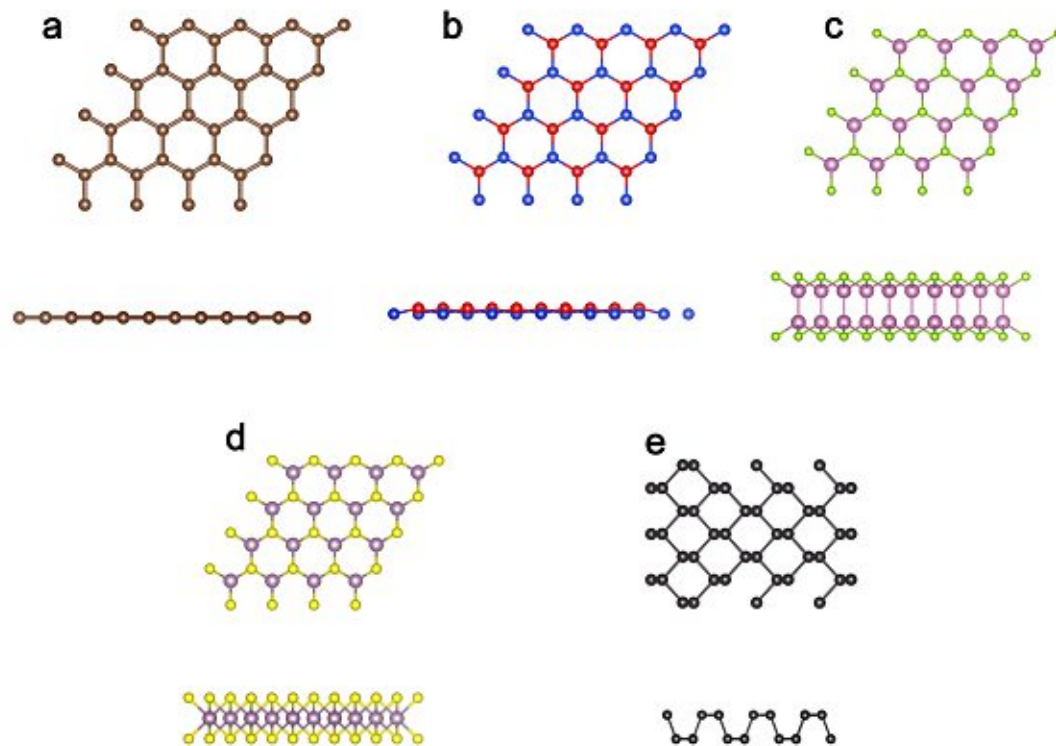


Figure 1.1: Top and side views of different 2D materials, representative of a particular structural group; a) graphene (graphene group); b) silicene (X-enes group); c) InSe (III-VI group); d) MoS₂ (MX₂ group); e) black phosphorus (BP group).

The structures of some of the most common 2D materials are shown in Fig. 1.1. In the upper-left panel it is possible to observe the structure of graphene, with an hexagonal and totally flat lattice. h-BN, a large bandgap insulator, shares the same structure. Silicene can be seen next, moving to the right. This material shares the same honeycomb structure of graphene, however showing a clear buckling - i.e. an out-of-plane protrusion - of some of the Si atoms. Other 2D materials, such as germanene and stanene, show a similar structure. In panel c, it is possible to observe the structure of InSe, belonging to the III-VI 2D materials group. Semiconducting 2D GaS shares the same structure. The lower-left panel reports the structure of MoS₂, a transition-metal-dichalcogenide (TMD) belonging to the large MX₂ group. Finally, black phosphorus is shown, with its typical puckered structure that has lost the perfect hexagonal arrangement.

The synthesis of 2D materials can be obtained using many different techniques, that can be grouped in two different categories. The first one describes *top down* methods, which start from a bulk material that is thinned down to the atomic level. This category includes the mechanical exfoliation technique that allowed to isolate graphene for the first time. Since 2004, many other 2D materials have been obtained using the mechanical exfoliation technique [16]. The yield of this technique is obviously limited and the flakes that can be obtained are relatively small. On the other side, the crystalline quality of the obtained materials is exceptionally high. Another approach that belongs to this category

is the chemical exfoliation technique, where the bulk material is dispersed in high-surface tension solvents or it is intercalated by a variety of agents that lead to exfoliation [17]. This technique can be used to produce large amounts of 2D layers, appropriate for an industrial usage. However, not all the materials can be exfoliated in this way and the quality of the produced materials is, for electrical applications, low. The second category includes those techniques that do not require a starting bulk material but are using a *bottom up* approach, where atoms and molecules are self-assembling in stable 2D structures. This second group of techniques not only allows to grow naturally occurring 2D materials - i.e. those that can be obtained by top down techniques - but can be also used to the synthesis 2D materials that are not occurring naturally. Within this group it is possible to find the Chemical Vapour Deposition (CVD) and the molecular beam epitaxy techniques. CVD grown 2D materials (graphene is an example) can be easily scaled and are characterised by exceptional electrical properties [18, 19]. On the other hand, MBE technique promises to be able to grow 2D materials on a larger number of substrates, as, differently from CVD, it does not require catalytic processes when solid sources are used. Additionally MBE allows for a precise control of the deposition rates, enabling sub-monolayer growth as well as multilayer growth of 2D materials. Moreover, since MBE is a technique that requires ultra high vacuum conditions, it allows to synthesise layers with an extreme level of purity, a perfect control of the interface as well as enabling the synthesis of extremely reactive 2D materials, of which silicene is an example [20].

1.1.1 Silicene

Si atoms are predicted to be able to form a planar structure with an sp^2 -like configuration, similarly to what happens for carbon atoms in graphene. Such a possibility was demonstrated by Takeda and Shiraishi using density functional theory [21]. Interestingly, differently from graphene, the equilibrium structure is not perfectly planar, but it possesses a slight buckling - i.e. corrugation. This structure has been described using the term *silicene*, following the name graphene, associated to a 2D arrangement of carbon atoms.

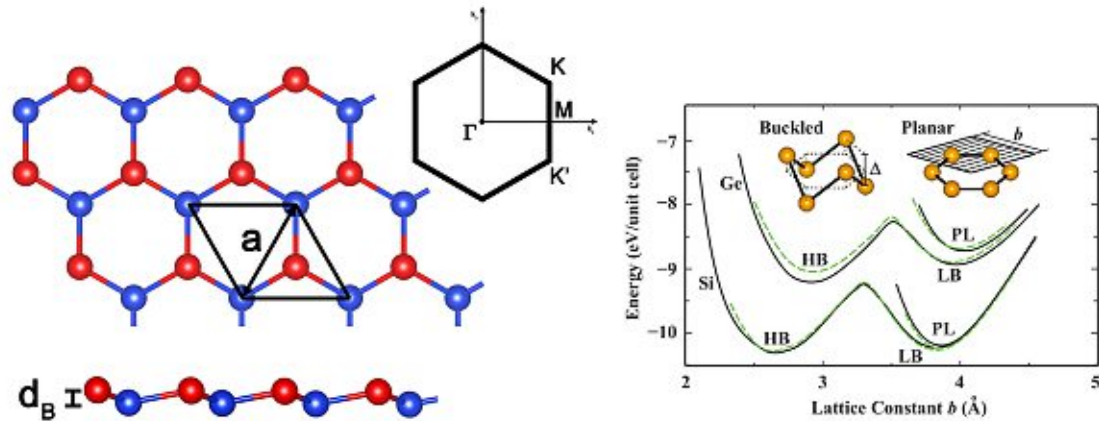


Figure 1.2: Simulated structure of a freestanding silicene layer with lattice parameter a . The silicon atoms arrange in an hexagonal fashion, with half of them showing a pronounced outwards buckling d_B . The inset shows the Brillouin zone for freestanding silicene, with the high symmetry point Γ , K and M. On the right, simulations taken from Ref.[22], show that a 2D structure of silicon atoms prefers to assume a buckled structure, to minimise the energy of the system. Two minima can be found, one for a higher buckling (HB), one for a lower buckling (LB), both lower than the one for a planar structure (PL). Similar results can be obtained also for germanene.

Fig. 1.2 shows the predicted buckled structure for freestanding silicene. Similarly to graphene, the atoms are occupying the main sites of an honeycomb lattice with two atoms per unit cell. The red atoms in the figure represent the outer-buckled ones. The equilibrium structure found through calculations within density functional theory (DFT) by Cahangirov et al. [22] is characterised by a lattice parameter $a=3.83 \text{ \AA}$ and by a buckling distance $d_B=0.44 \text{ \AA}$. This structure is described by a rhomboidal unit cell, with two atoms per cell. One can think each of the two atoms as belonging to two similar hexagonal lattices, shifted vertically between each other. The Brillouin zone of this structure is, consequently, also hexagonal. The presence of two atoms in the unit cell leads to two inequivalent K points (K and K'). Additionally, a more energetically favourable structure can be found when the buckling is increased. This structure, however, is characterised by a significantly shorter lattice constant and has not been observed experimentally yet. The buckled structure has a slightly lower formation energy, compared to a fully planar one, as evidenced in Fig. 1.2.

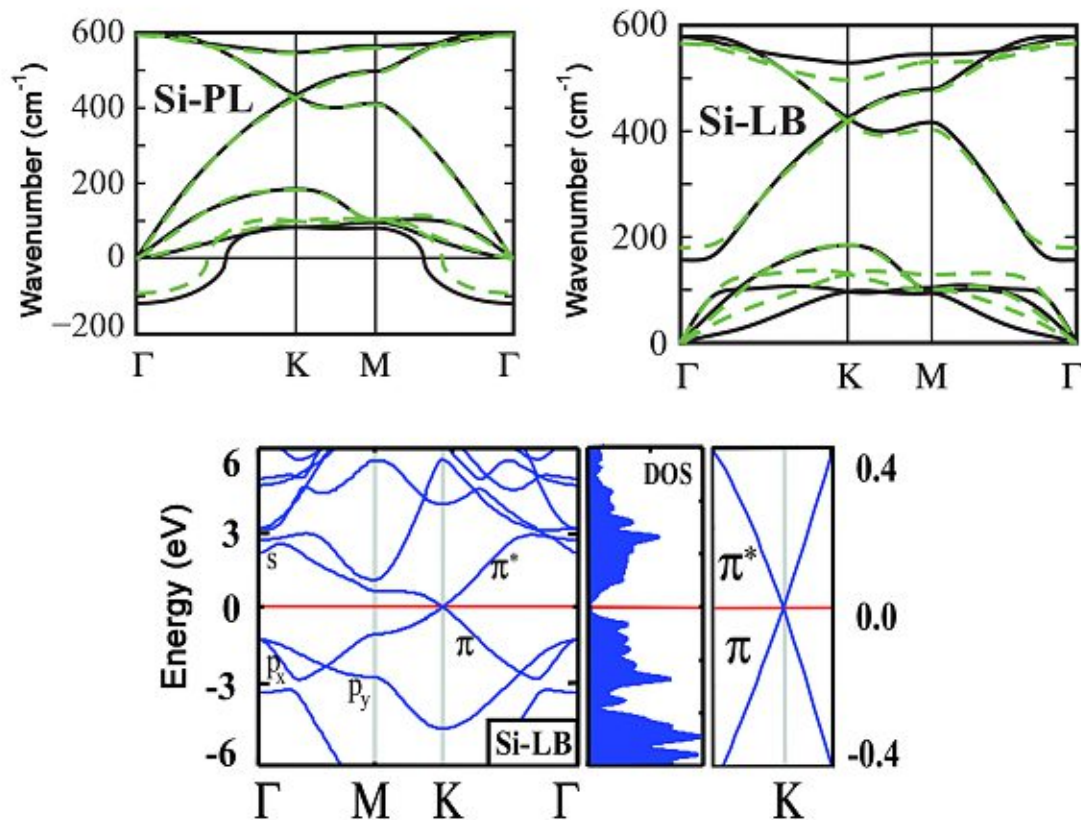


Figure 1.3: Taken from Ref.[22] - left: phonon dispersion curves calculated for a totally planar 2D silicon structure; right: phonon dispersion for a low-buckled silicene structure; below: electronic band structure, calculated in a tight binding approximation, for a low-buckled silicene structure. Linearly dispersing bands meet at the K point of the Brillouin zone, forming a Dirac cone.

Nevertheless, the simulated phonon dispersion curves for a totally planar silicene structure clearly report negative frequencies, as shown in Fig. 1.3, meaning that it cannot be considered stable. By assuming a buckled structure, silicene lowers its symmetry compared to the totally planar case of graphene. While the latter belongs to point group C_6 , freestanding silicene can be described by point group D_{3d} [23]. Symmetry properties are important as they can be used to predict many of a material properties [24]. Notably, the vibrational modes of a layer, observable using techniques such as Raman spectroscopy, and its symmetry operations are strictly related. Freestanding silicene presents two allowed vibrational modes, described by the values of the phonon curves in Fig. 1.3, at the Γ point of the Brillouin zone ($k=0$). The low-frequency mode describes out-of-plane vibrational modes and it is located at 175 cm^{-1} . The in-plane vibrational modes, which are doubly degenerate, are expected at 566 cm^{-1} . Based on the symmetry properties of the freestanding silicene layer, the out-of-plane vibrational mode is expected to be totally symmetric, showing an A symmetry, while the in-plane modes are expected to show an E symmetry [25]. Interestingly, in case of silicene, the out-of-plane vibrational mode is Raman active, where this is not true for graphene [26]. Since this mode is exclusive to

a two-dimensional silicene structure - i.e. it is not present in bulk crystals - and it is totally symmetric, meaning that it can be clearly distinguished in Raman experiments, it represents a unique opportunity for a clear identification of silicene.

Electrical properties of silicene

Besides the peculiar structural properties, silicene's most distinctive signature is certainly given by its electronic properties. The calculated band structure, shown in Fig. 1.3, is characterised by linear bands crossing at the Fermi level, with Dirac points at the K and K' points of the Brillouin zone. This particular band dispersion is very similar to the one of graphene. It is instructive to show how this result can be obtained using the tight binding approximation [27] in the case of graphene, where the total planarity of the structure allows for a simplified analytical derivation [28]. The model is derived by considering only nearest-neighbour hopping. For a given atom in a graphene structure, its 3 nearest neighbours can be reached by considering the following displacements

$$\begin{aligned}\delta_1 &= \frac{a}{2}(1, \sqrt{3}) \\ \delta_2 &= \frac{a}{2}(1, -\sqrt{3}) \\ \delta_3 &= -a(1, 0)\end{aligned}\tag{1.1}$$

Using the second quantisation formalism, the tight-binding Hamiltonian is:

$$H = -t \sum_{i,j} (a_i^\dagger b_j + b_j^\dagger a_i)\tag{1.2}$$

where i, j are indexing the sites of the two sublattices (A, B) that compose the graphene sheet, a^\dagger and b^\dagger are the creation operator for the creation of an electron at the A or B sublattice sites with position r_i , a and b are the annihilation operators for the destruction of an electron at the A or B sublattice sites with position r_i . By referring to the positions of the nearest-neighbours indicated before as δ , it is possible to rewrite the Hamiltonian as

$$H = -t \sum_{i \in A} \sum_{\delta} (a_i^\dagger b_{i+\delta} + b_{i+\delta}^\dagger a_i)\tag{1.3}$$

where the summation over delta includes all the three nearest neighbours. Accounting for the periodicity of the lattice, the creation and annihilation operators can be written as

$$a = \frac{1}{\sqrt{N/2}} \sum_k e^{ik \cdot r_i} a_k\tag{1.4}$$

where N are the number of sites of A+B sublattices. By substituting and summing the Hamiltonian becomes

$$H = -t \sum_{\delta, k} (e^{-ik \cdot \delta} a_k^\dagger b_k + e^{ik \cdot \delta} b_k^\dagger a_k)\tag{1.5}$$

This can be expressed as

$$H = \sum_k (\Psi^\dagger h(k) \Psi) \quad (1.6)$$

$$\text{with: } \Psi = \begin{pmatrix} a_k \\ b_k \end{pmatrix}, \Psi^\dagger = \begin{pmatrix} a_k^\dagger \\ b_k^\dagger \end{pmatrix}, h(k) = -t \begin{pmatrix} 0 & \Delta_k \\ \Delta_k^* & 0 \end{pmatrix}$$

where $\Delta_k = \sum_\delta e^{ik \cdot \delta}$. The off-diagonal elements in the case of graphene are zero due to the fact that the atoms from A and B sublattices are identical. From this it follows that the eigenvalues are $E_\pm = \pm t \sqrt{\Delta_k \Delta_k^*}$. Taking into account the values for Δ_k expressed before, one gets:

$$E_\pm(k) = \pm t \sqrt{1 + 4 \cos\left(\frac{3}{2} k_x a\right) \cos\left(\frac{\sqrt{3}}{2} k_y a\right) + 4 \cos^2\left(\frac{\sqrt{3}}{2} k_y a\right)} \quad (1.7)$$

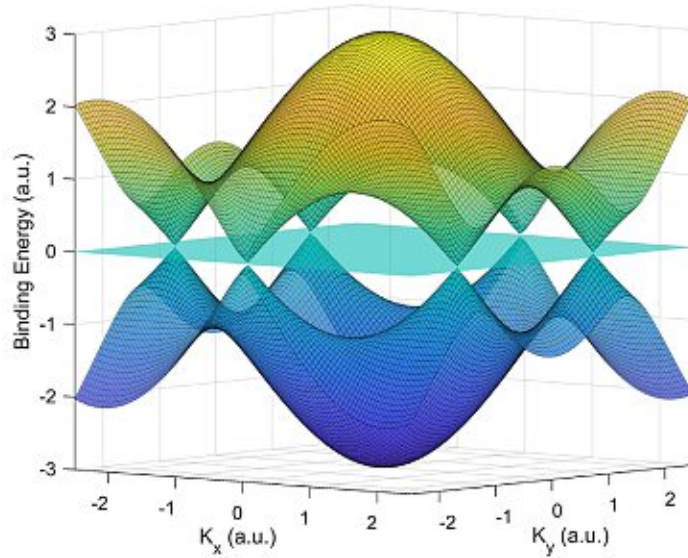


Figure 1.4: Plot of the calculated band dispersion for graphene near the Fermi level (blue plane). Valence and conduction bands touch at the K and K' points of the Brillouin zone, forming Dirac cones.

If this equation is plotted in k space, one gets the familiar bands meeting at the K point of the Brillouin zone, forming two Dirac cones with the tips joining at $E=0$, as shown in Fig.1.4

This is very similar to what happens in silicene. In that case, however, the atoms in the two sublattices are not identical, as they are displaced differently along the z direction (buckled). This important difference introduces a nonzero off-diagonal term in the $h(k)$ matrix which leads to the opening of a bandgap. Moreover, spin-orbit interaction is further widening the bandgap. The fact that bandgap opening is related to the buckling of the Si atoms is very important. By varying the buckling parameter, it is thus possible to tune the bandgap of silicene.

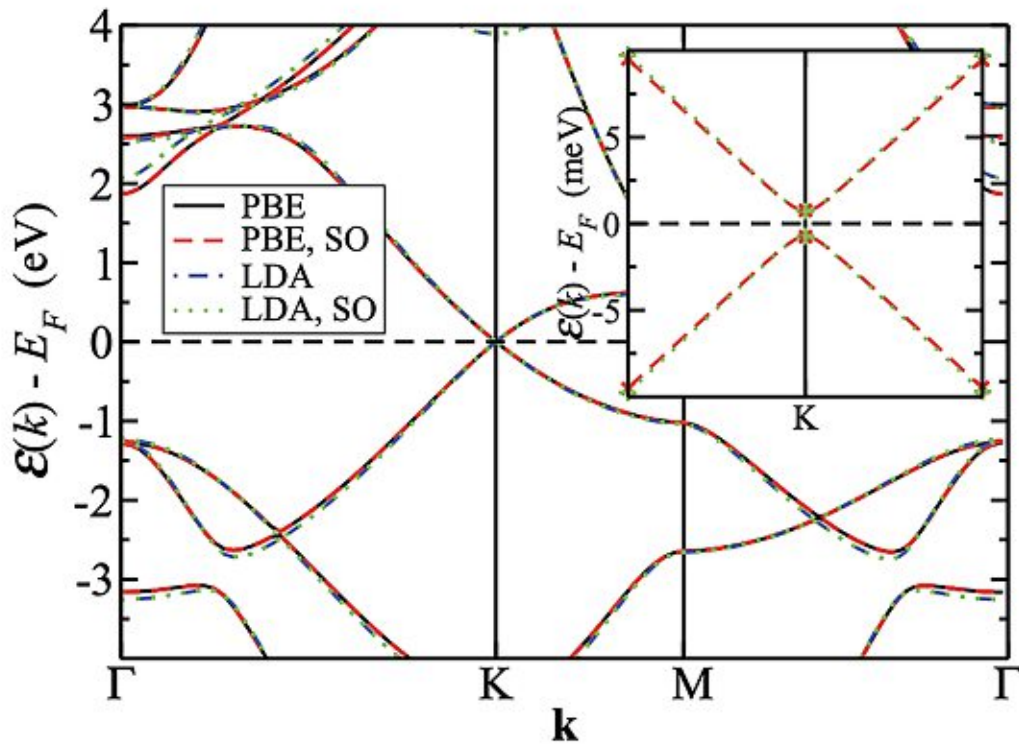


Figure 1.5: Taken from Ref. [6]. Self consistent DFT calculations of the electronic structure of a freestanding single silicene layer. Black and red lines are calculated using the Perdew-Burke-Ernzerhof (PBE) exchange-correlation functional, the blue and green lines are calculated in the Local Density Approximation (LDA). The green and red lines take the spin-orbit interaction into consideration, which leads to the widening of the band gap at the K point of the Brillouin zone.

The theoretical band structure for freestanding silicene, taken from Ref.[6], is shown in Fig. 1.5. Finally, it is worth noting that the linear bands at the K point of silicene will be responsible for the electron transport in electronic devices based on this 2D material. In case of linear bands, the Hamiltonian describing the electrons is reminiscent of the one for massless fermions. This means that, in this material, similarly to graphene, relativistic effects such as the half-integer quantum Hall effect and Klein tunnelling effect can arise [29]. It is important to note that the electrons do not move at lightspeed, despite being described as massless. They are expected to possess, however, an extremely high Fermi velocity, close to $\sim 0.6 \cdot 10^6 \frac{m}{s}$ [6], which is similar to the value measured in graphene [16].

Supported Silicene

Despite the effort, freestanding silicene has not yet been isolated. Most of the experimental results are obtained studying silicene grown on a substrate. One of the most suitable substrates for the growth of silicene layers is certainly Ag(111) [3, 30, 31]. On this substrate, different silicene phases are obtained, with structures differing from the freestanding one.

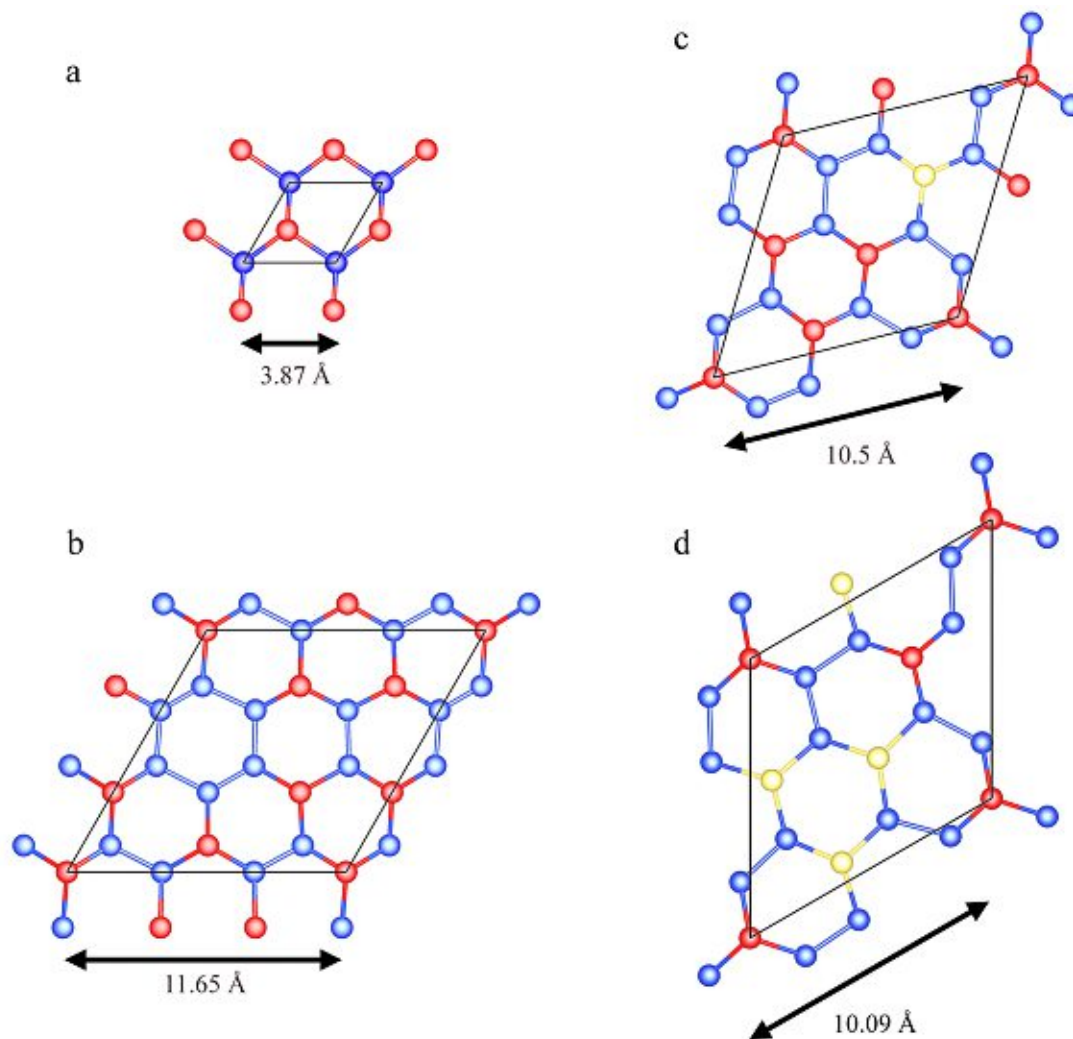


Figure 1.6: Representation of the structures obtained by growing 1 ML silicene on Ag(111), compared to the free-standing layer (a). At a growth temperature of 260 °C two phases are observed, the 4×4 phase (b) and the $\sqrt{13} \times \sqrt{13}$ R13.9° one (c). A higher growth temperature of 300 °C leads to the formation of the $2\sqrt{3} \times 2\sqrt{3}$ R30° phase (d)

Figure 1.6 shows a representation of all the silicene structures obtained on Ag(111), in comparison to the predicted structure of freestanding silicene. The freestanding phase, shown in panel a, is characterised by a unit cell with a lattice parameter of 3.87 Å. The unit cell consist of two atoms, one buckled outwards by 0.45 Å. The structure of free-standing silicene is slightly less symmetrical than graphene, due to the buckling. While graphene belongs to point group D_{6h} , having a 6-fold rotation axis plus 6 perpendicular 2-fold rotation axes, a horizontal mirror plane and 6 vertical mirror planes, free-standing

silicene belongs to group D_{3d} , characterised by a 3-fold rotation axis plus 3 perpendicular 2-fold rotation axes and 3 vertical mirror planes.

The various phases of silicene obtained on Ag(111) are described, in the following paragraphs, using the Wood notation, which provides an analytical way of expressing the relationship between the substrate crystal and the grown structure, as explained in details in Sec.1.4, directly expressing the ratio between the lattice parameters of the grown layer and the substrate, as well as the rotation of the layer with respect to the underlying crystal.

The unit cell of the 4×4 phase, shown in Fig. 1.6b, contains 18 atoms, 6 of which are buckled outwards by 0.8 \AA , as shown in red. The unit cell size is 3 times the one of freestanding silicene, with a length of 11.65 \AA . Interestingly, the structure belongs to the highly symmetrical point group C_{6v} , meaning that it has a 6-fold rotation axis and 6 vertical mirror planes. This point group, however, is not a subgroup of the D_{3d} one, [23], meaning that this phase cannot be derived from the free-standing structure through a loss of symmetry. This is a first, powerful indication of how the Ag substrate is substantially modifying the silicene structure, differentiating it from the freestanding one.

The other two phases (panels c and d) belong to point group C_1 and are therefore characterised by a drastic reduction of the symmetry. The $\sqrt{13} \times \sqrt{13}$ phase is characterised by a unit cell with an edge length of 10.5 \AA , containing 15 atoms, with 4 atoms buckled outwards by 0.78 \AA and 1 atom with an intermediate position, shown in yellow. The $2\sqrt{3} \times 2\sqrt{3}$ phase is described by a unit cell with an edge of 10.09 \AA , containing 14 atoms, with 2 buckled outwards by 1.12 \AA (red) and 3 atoms buckled at an intermediate position (yellow).

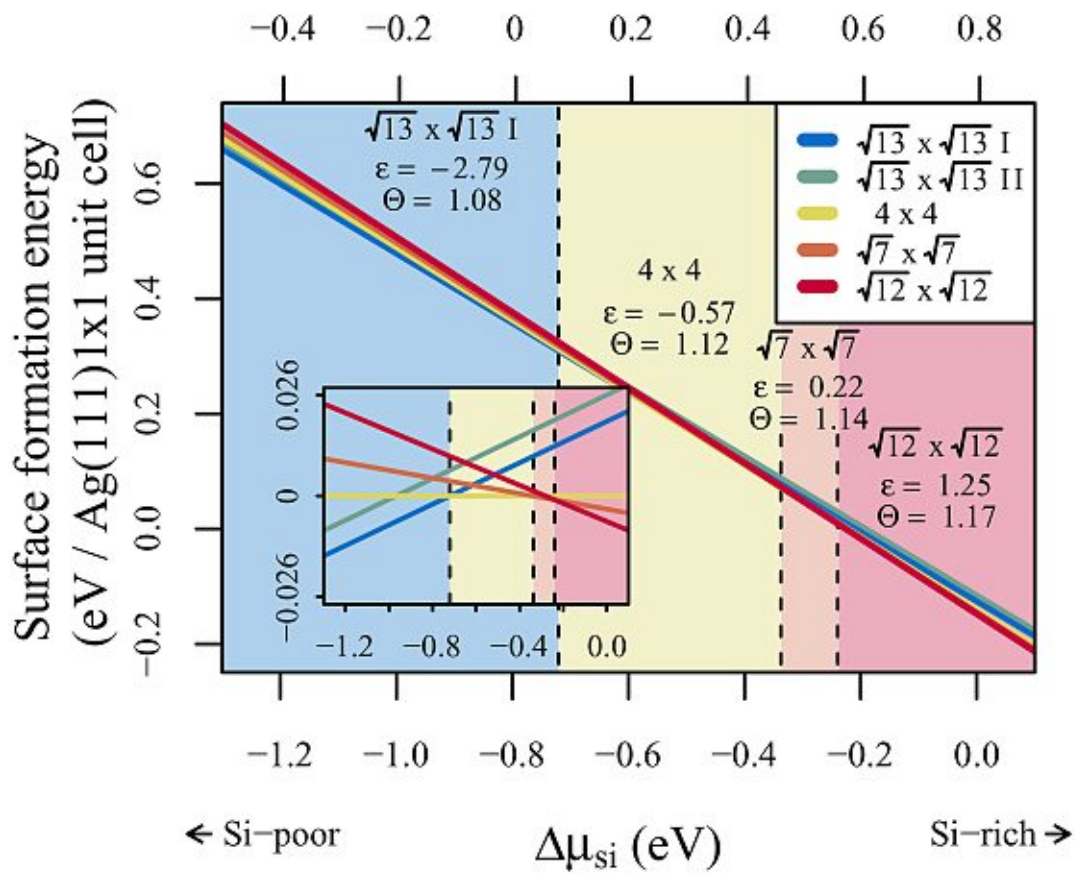


Figure 1.7: Image taken from Ref. [23]. The formation energy of silicene phases on Ag(111) plotted as a function of the Si chemical potential. The chemical potential difference (Δ) is calculated with respect to freestanding silicene (bottom axis) or to diamond sp^3 Si (top axis). Θ indicates the coverage, ϵ the strain.

Pflugradt et al. [23] calculated the formation energies of various phases of silicene observed on Ag(111), as reported in Fig. 1.7. All the phases are characterized by a similar formation energy, with a difference smaller than 0.01 eV per Ag(111) 1×1 unit cell. The calculation predicts that the 4×4 phase is the most stable for Si-rich preparation conditions, while the $2\sqrt{3} \times 2\sqrt{3}$ one becomes the most favourable only in extremely Si-rich conditions.

1.2 Raman Spectroscopy

Raman spectroscopy [32] is a technique that is based on inelastic scattering of monochromatic radiation and it is used to investigate the structural properties of molecules and materials. This process is extremely less probable than the one involving an elastic scattering - i.e. the Rayleigh scattering. In the inelastic scattering process, energy is exchanged between the incoming photon and the analysed target, inducing a change in the energy of the scattered photon. The energy variation is caused by the illuminated molecules changing to different vibrational and rotational states. The scattered light is analysed with a detector and the generated spectrum can give useful information on the structure of the examined material.

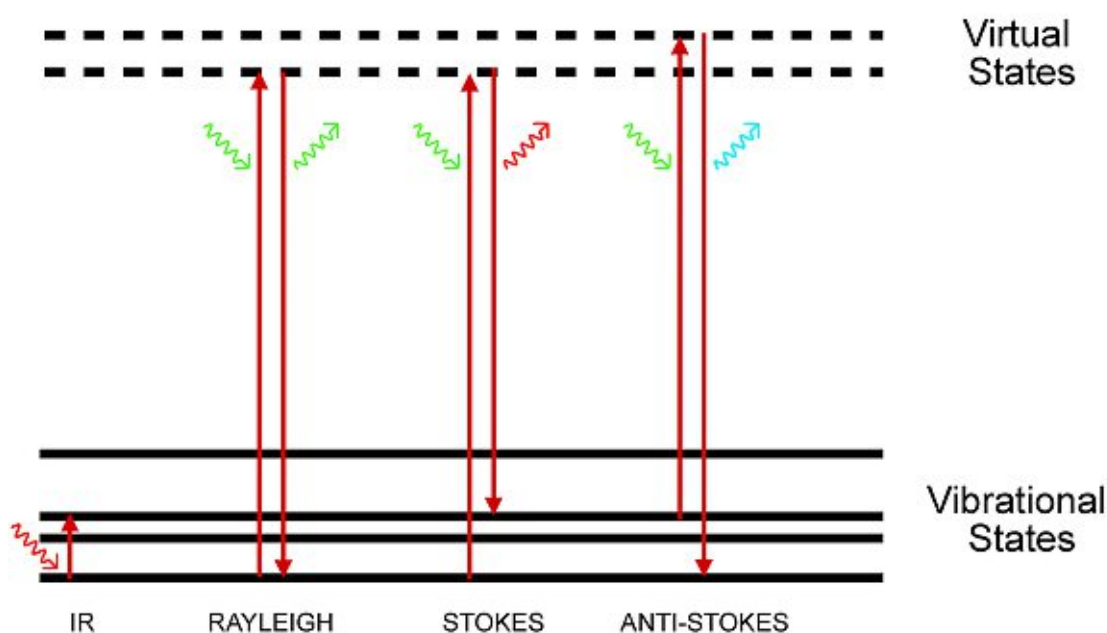


Figure 1.8: Schematic representation of IR, Rayleigh, Raman Stokes and Raman Anti-Stokes processes.

Some of the processes that can be observed when a photon is absorbed by a molecule or a crystal are schematically depicted in Fig. 1.8. In an infrared (IR) process, photons induce a change in the dipole moment. In this case, the molecule or crystal target is excited to a vibrational state with higher energy. In a Rayleigh process, instead, the target material is excited to a *virtual* state, where it stays only for a very short time, finally returning to the original vibrational state. A photon with the same energy of the exciting one is emitted during this process. In a Raman process, instead, the emitted photon has a different energy than the excitation one. Raman processes are related to a change in the polarisability of the target molecule or crystal.

Raman processes are divided in two different categories, called Anti-Stokes and Stokes. In both cases, the target molecule or crystal is excited by a photon to a *virtual* state, where it remains only for a short time. At the end of an Anti-Stokes process, the molecule or crystal finds itself in a vibrational state with a lower energy than the initial one, emitting

a photon with a higher energy than the excitation source. In the other case, the final state of the crystal or molecule has a higher energy than the initial one, while the photon has lost energy. Due to energetic reasons, Stokes processes are much more probable (and thus more intense) than Anti-Stokes ones and therefore are commonly the analysed ones [33]. In a crystal, the energy difference between the detected photons and the excitation source, usually expressed in cm^{-1} , is closely related to the phonon dispersion curves at the Γ point of the Brillouin zone. This connects the observed Raman peaks, or modes, with the structural properties of the analysed material. Generally, the position of the detected Raman peaks depends on the bond type and length. Shifts in the position of the peaks can indicate the presence of strain in a structure [34].

Polarisation dependent Raman spectroscopy

Raman spectroscopy can be extended by studying the polarisation properties of the emitted photon as a function of the polarisation state of the excitation source.

This can be understood by considering that the intensity of a Raman mode is proportional to:

$$I \propto |\langle P_i | \alpha | P_s \rangle|^2 \quad (1.8)$$

where α is the polarisability tensor and P_i and P_s are the incident and scattered light polarisation vectors.

In a Raman setup with a backscattering geometry - i.e. when the incident and scattered photons move both on the same line, perpendicular to the surface of the sample, but in opposite directions - the vectors for the direction of the incident and scattered light are given by $\pm \begin{pmatrix} 0 \\ 1 \end{pmatrix}$.

If the excitation and scattered photons are linearly polarised, it is possible to express the polarisation vector of the incident light as $P_i = \begin{pmatrix} \cos(\theta_i) \\ \sin(\theta_i) \\ 0 \end{pmatrix}$, and the one for scattered light as

$P_s = \begin{pmatrix} \cos(\theta_s) \\ \sin(\theta_s) \\ 0 \end{pmatrix}$, where the angles of polarisation θ_i and θ_s are defined in the sample plane.

Notably, the α tensor linked to a specific Raman mode possesses the same symmetry properties of the associated Raman tensor. For a given structure, all the possible Raman tensors are well predicted by group theory [24]. As an example, a highly symmetrical hexagonal structure, like the one of graphene, is described by point group D_{6h} . This is due to the fact that the structure possesses a 6-fold rotational axis, as well as six 2-fold rotational axis perpendicular to the first one and a mirror plane. According to group theory, the Raman modes visible in a back-scattering geometry are described by the following Raman tensors:

$$A_{1g} : \begin{pmatrix} a & 0 & 0 \\ 0 & a & 0 \\ 0 & 0 & b \end{pmatrix}, E_{2g} : \begin{pmatrix} d & 0 & 0 \\ 0 & -d & 0 \\ 0 & 0 & 0 \end{pmatrix}, E_{2g} : \begin{pmatrix} 0 & -d & 0 \\ -d & 0 & 0 \\ 0 & 0 & 0 \end{pmatrix}$$

Depending on the direction of the polarisation, the A_{1g} vibrational mode can be visible or completely suppressed, while the E_{2g} modes are always visible. This means that, by studying the Raman spectrum in parallel and cross polarisation configurations it is possible to get a precise picture of the symmetry properties of the analysed material. This, in addition to the information given by the position of the Raman peaks, can be used to build a detailed description of the structure of a crystal or molecule, making Raman spectroscopy one of the best methods for the analysis of 2D materials.

1.3 Photoemission Spectroscopy

Photoemission spectroscopy (PES) is one of the most important techniques for investigating the electronic properties of solids and surfaces [35]. This experimental method is based on the photoelectric effect, where characteristic electrons are extracted from a sample after the interaction with UV photons. [36, 37]. This generally happens when the energy of the photons exceeds the work function Φ_0 of the sample surface, therefore requiring light belonging, at least, to the UV range of the spectrum. The two quantities that are measured in a photoemission spectroscopy experiment are the kinetic energy of the extracted electrons and their k vector.

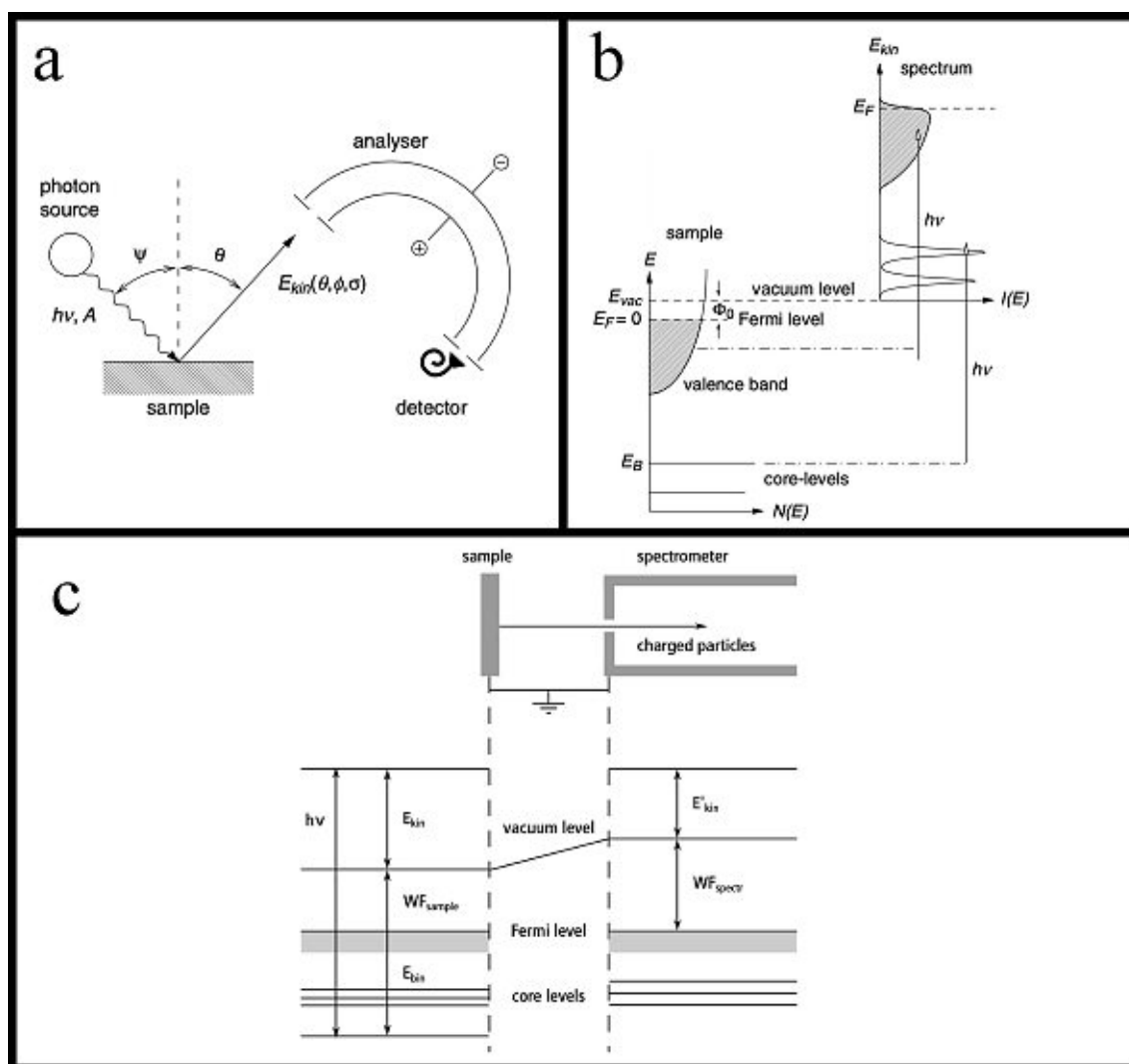


Figure 1.9: Images taken from [38]. a) Schematic representation of a PES; b) schematic representation of a simplified photoemission process; c) energy scheme in a photoelectron spectroscopy experiment.

In a typical PES experiment, shown schematically in Fig. 1.9, a beam of monochromatic photons is directed towards a surface. When the material is hit by the beam of photons, some of its electrons are excited and emitted in the surrounding space. Those emitted at a certain angle Θ are captured by a hemispherical analyser capable of measuring their

kinetic energy and, with the help of an electron detector, their number - i.e. the intensity. In common laboratory experiments, electrons can be extracted either from the valence band states, using UV photons, or from the more tightly bound core levels, using X-rays. Before exploring the different methods that can be used to produce the required photons and those used to analyse the emitted electrons, it is interesting to take a look into the basic theory that describes, in a simplified way, a photoemission event. Such a process is complicated by the fact that the analysed sample is, in reality, a many-body system and that many-body interactions play a role in determining the final state of the emitted electron. Nevertheless, a single-particle simplification is a valid approach for the interpretation of many photoemission experiments. The detected photocurrent J can be expressed as a function of the initial and final states of the emitted electrons:

$$J(k, \epsilon) \propto \sum_s |\langle N-1, s; k | H_{PE} | N, 0 \rangle|^2 \delta(E_{N,s} - E_{N,0} - h\omega) \quad (1.9)$$

where the final state is represented by a system of $N-1$ electrons, with s representing a set of quantum numbers for all possible excitations, and a single photoelectron with wavevector k and energy ϵ . It is important to note that, at this point, the final state represents a situation where the emitted photoelectron is still interacting with the $N-1$ electrons that are left in the solid.

The H_{PE} operator models the interaction of an electron with the electromagnetic field of the photons. Under a simplified picture, it can be expressed as:

$$H_{PE} = \frac{e}{m_e c} A \cdot p \quad (1.10)$$

where A is the vector potential operator associated to the electromagnetic field and p is the momentum operator.

Under the single-particle simplification, the extracted electron does not interact with the $N-1$ electrons that are left in the solid. The final state becomes:

$$|N-1, s; k\rangle \rightarrow c_k^\dagger |N-1, s\rangle \quad (1.11)$$

where c_k^\dagger is the creation operator for a photoelectron of wavevector k and energy ϵ . This allows to write the photocurrent as

$$\begin{aligned} J(k, \epsilon) &\propto \sum_s |\langle N-1, s | c_k^\dagger | N, 0 \rangle|^2 \delta(E_{N-1,s} + \epsilon - E_{N,0} - h\omega) \\ &\propto \mathbf{A}(k, \epsilon - \hbar\omega) \cdot f(\epsilon - \hbar\omega) \end{aligned} \quad (1.12)$$

where f is the Fermi distribution and $A(k, \epsilon - \hbar\omega)$ is the one-electron spectral function, which is a measurement of the probability of adding or removing an electron with wavevector k and energy $\hbar\omega$. This function accounts for the many-body interaction between the $N-1$ electrons that are remaining in the solid, after the emission of the photoelectron. Notably, the sum over k of the spectral function is equal to the single-particle density of states. PES is capable of measuring only the intensity of the photocurrent for a given energy will get information regarding the density of (occupied) states of the material. Instead, an experiment capable also of probing the wavevector of the emitted electrons

is able to measure the full spectral function, which includes information regarding the multi-body interactions.

In a typical photoemission experiment, the wavevector of the emitted electrons can be extrapolated from the measured emission angle. It must be noted that, however, only the component of the wavevector that is parallel to the surface of the sample can be directly obtained, as this is the only quantity that is conserved when the photoelectron transitions from the material into the vacuum. It is possible to connect the measured dispersion angle to the component of the wavevector parallel to the surface of the sample through a simple formula:

$$K_{//}^{solid} = K_{//}^{vacuum} = \sqrt{\frac{2m}{\hbar^2} E_{kin}} \sin\theta_{out} \quad (1.13)$$

where E_{kin} is the measured kinetic energy of the photoelectrons. It is possible to obtain the binding energy of the observed photoelectrons by noting that, in general

$$E_{kin} = h\nu - E_{bin} - WF_{sample} \quad (1.14)$$

where $h\nu$ is the energy of the excitation photons and WF is the working function of the sample. However, since the analyser and the sample are both grounded, their Fermi levels coincide, as shown in Fig. 1.9c. By following the energy scheme shown in the figure, it is possible to write that

$$E_{kin} + WF_{sample} = E_{kin}^* + WF_{spectrometer} \quad (1.15)$$

where E_{kin}^* is the kinetic energy of the electrons measured by the spectrometer and $WF_{spectrometer}$ is the work function of the spectrometer, which can easily be measured and calibrated. From this follows that

$$E_{bin} = h\nu - (E_{kin}^* + WF_{spectrometer}) \quad (1.16)$$

showing that the binding energy can be easily obtained.

1.4 Low Energy Electron Diffraction

Low energy electron diffraction is one of the first techniques that were developed for the study of surfaces [39]. This technique is based on the elastic scattering of a beam of electrons on the surface of a solid. The energy of these electrons is kept below 1000 eV and can be as low as a few electronvolts, resulting in an elastic mean free path smaller than 10 Å. This means that the signal generated by the elastically scattered electrons is strictly related only to the surface region of the analysed target.

The observed diffraction pattern can be explained, in first approximation, by assuming that the electrons are being scattered only once by a well ordered crystalline surface layer. The position of the observed diffraction peaks can be calculated using the Laue formula [40], which gives the condition for constructive interference between incident and scattered electrons.

$$K_f - K_i = G_{hkl} \quad (1.17)$$

where K_i is the wave vector of the incoming electrons, while K_f is the one of the scattered beam. G_{hkl} indicates a vector of the reciprocal lattice, where h,k,l are the Miller indices. In the approximation that the electrons are scattered only by the very first layer, no diffraction condition must be fulfilled in the direction perpendicular to the surface. From this follows that the Laue conditions becomes

$$K_f^{//} - K_i^{//} = G_{hk} = h \cdot a^* + k \cdot b^* \quad (1.18)$$

where a^* and b^* are the primitive translation vectors of the reciprocal 2D lattice of the analysed surface. Therefore, LEED patterns give a picture of the analysed surface in reciprocal space.

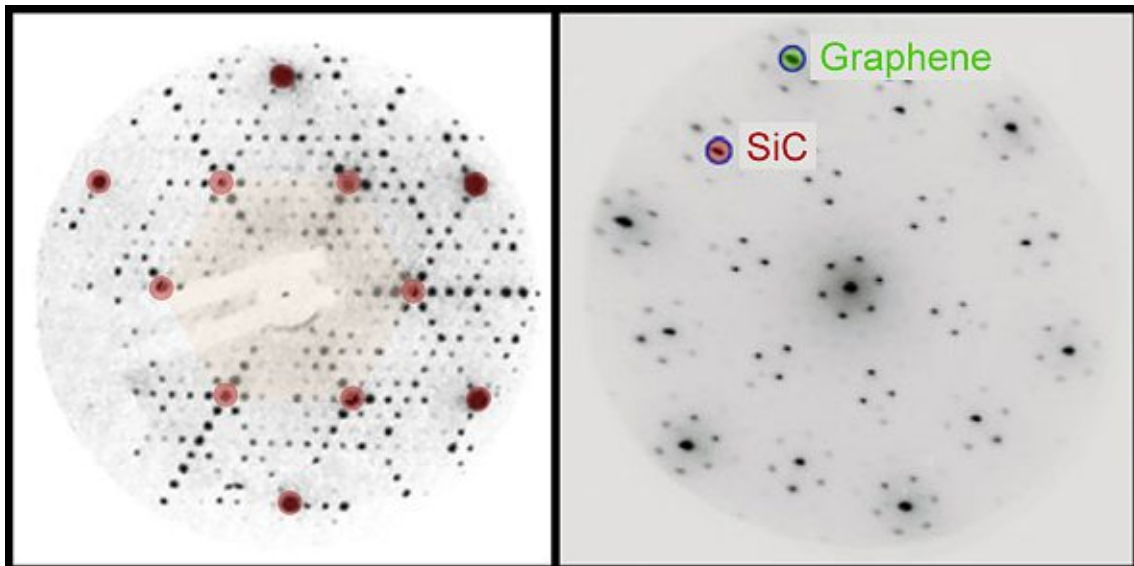


Figure 1.10: Left: image adapted from Ref. [41] showing the LEED signal of a Si(111) substrate. Right: image adapted from Ref. [42] showing the LEED signal of graphene on a SiC substrate.

The interpretation of a LEED pattern can be complicated by the presence of surface reconstructions, that are energetically favourable structural modifications of the surface layer leading to a different arrangement of the atoms compared to the bulk region, or by the presence of adsorbate layers, like in the case of 2D materials growing on a substrate. Examples of these two cases are shown in Fig. 1.10. On the left, a LEED pattern from a Si(111) surface is reported. The diffraction maxima related to an ideal 1×1 Si surface are highlighted in red, all the other dots are related to the presence of a 7×7 reconstruction on the surface. On the right, a LEED pattern of a graphene layer grown on SiC is reported. Both structures give rise to visible diffraction peaks.

Different notations have been proposed to better describe the structures that give rise to the additional diffraction maxima.

The simplest one is the Wood notation [43]. Assuming that the substrate lattice can be described by the unit base vectors a_1 and a_2 and that the overlayer structure is using, instead, vectors b_1 and b_2 , then it is possible to define the integers m , n such that

$$\frac{|b_1|}{|a_1|} = m; \quad \frac{|b_2|}{|a_2|} = n \quad (1.19)$$

Additionally, Θ is defined as the angle between a_1 and b_1 vector. The superstructure can then be described, using the Wood notation, as

$$m \times n R \Theta \quad (1.20)$$

Obviously, this notation is able to describe only superstructures that have the same symmetry as the substrate. A more general description can be constructed by using the Matrix notation [44]. The unit base vectors of the overlayer structure can be expressed as a function of the vectors of the substrate:

$$\begin{pmatrix} b_1 \\ b_2 \end{pmatrix} = \begin{pmatrix} m_{11} & m_{12} \\ m_{21} & m_{22} \end{pmatrix} \cdot \begin{pmatrix} a_1 \\ a_2 \end{pmatrix} = M \cdot \begin{pmatrix} a_1 \\ a_2 \end{pmatrix} \quad (1.21)$$

Notably, the determinant of the M matrix is a measure of the ratio between the unit cell area of the overlayer and of that of the substrate:

$$\det(M) = \frac{|b_1 \times b_2|}{|a_1 \times a_2|} \quad (1.22)$$

This number can be used to classify the type of superstructures. It is possible to identify three different cases:

1. $\det(M)$ is an integer and all m_{ij} are integers: the superstructure is simply related to the surface of the substrate, showing the same translational symmetry and the layers are commensurate. This includes all those overlayers that can be described by the Wood notation.
2. $\det(M)$ is a rational number (not an integer) *or* $\det(M)$ is an integer but some m_{ij} are rational numbers (not integers). In this case the two structures are rationally related, with the lattices coming into correspondence at regular intervals.
3. $\det(M)$ is an irrational number. This means that no common periodicity exists between the overlayer and the substrate. In this case the superstructure is defined as incoherent. The adsorbate layer is incommensurate with respect to the substrate.

Chapter 2

Experimental Methods

2.1 Molecular Beam Epitaxy

MBE is a technique that allows to grow epitaxially a film by a process involving the reaction of one or more thermal molecular beams with a crystalline surface under UHV conditions [45]. MBE has been introduced to deposit very thin films with a perfect control of their composition, thickness and of the surface morphology. Generally, it is possible to distinguish between two different cases:

- Solid source MBE: molecular beams are obtained by thermal evaporation of solid sources
- Gas source MBE: evaporation materials are introduced in gaseous form and decomposed

Independently from the type of source used, the key aspect that truly characterise and enables MBE growth is the base (or background) pressure. In case of solid sources, the base pressure is typically lower than 10^{-10} mbar. Such a low pressure allows to drastically increase the mean free path of a molecule - i.e. the average length that it can travel before scattering with another molecule. While at ambient pressure the mean free path is less than 100 nm [46], in UHV conditions it increases by 10^{13} times. This allows to avoid chemical interactions between the evaporated atoms or molecules and unwanted species. A low base pressure is not only required to have scattering-free molecular beams but it is also necessary for maintaining the surface of the substrate clean from impurities during growth.

The Hertz-Knudsen formula allows to calculate the flux of molecules impinging on a surface of 1 m^2 in 1 s:

$$F = \frac{p}{\sqrt{2\pi mkT}} \quad (2.1)$$

Where p is the partial pressure of the species of interest, m is the molecular mass, k the Boltzmann constant and T the temperature.

Knowing that 1 ML consists of approximately $10^{19} \frac{\text{atoms}}{\text{m}^2}$ and assuming a sticking coefficient of 1, the minimum time required for the formation of a layer of unwanted species with a partial pressure of $1 \cdot 10^{-10}$ mbar is thus approximately 3 hours. At a pressure of

10^{-6} mbar this time reduces drastically to only 1 s, obviously too short for completing any experiment.

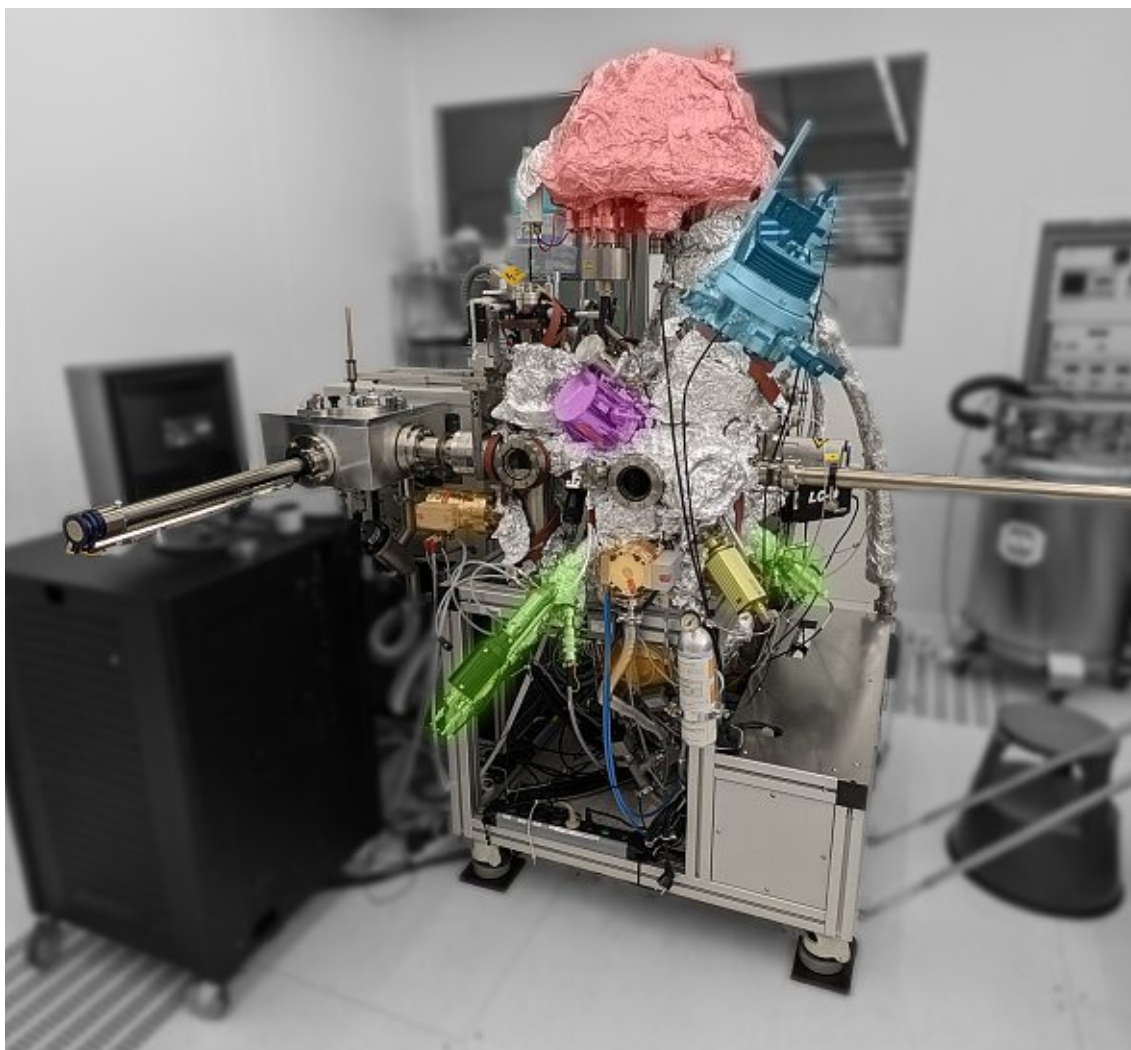


Figure 2.1: UHV system used for all the experiments described in this work. Orange areas are indicating the position of the pumps, green the evaporation sources, blue the low energy electron diffraction optics, red the hemispherical analyser, purple the large area sputterer, yellow the infrared pyrometer.

To fulfil these requirements, a system of pumps is used. Fig. 2.1 shows a photo of the actual MBE system used for the growth experiments and some of the analysis presented in this work. The system is equipped with a total of four turbomolecular pumps (TMPs), (highlighted in orange in the image, one is at the back).

In addition to mechanical pumps, the UHV system is also equipped with a titanium sublimation pump. This type of pump is particularly effective for pumping away some of the lightest gases, like H_2 , that are not particularly well expelled by turbo pumps.

Even by combining all these pumps, the pressure can be lowered down only to 10^{-7} mbar. At this level of vacuum, most of the molecules from the volume of the chamber are pumped away. However, many others, particularly H_2O , are adsorbed on the walls of the chamber and they randomly desorb, determining the final pressure to be too high. To solve this

problem, the walls of the UHV chamber must be kept at an increased temperature ($\sim 100^\circ\text{C}$) for several days during the so-called *Bake Out* process. By doing so, molecules desorb from the walls of the chamber and thus can be pumped away more quickly. Combining the effect of the pumps and of the *Bake Out* process, the system reaches a final base pressure of $\sim 3 \cdot 10^{-10}$ mbar.

Once the pressure is in the correct range, it is possible to start with the growth experiments. For this step, two aspects are important: the preparation of the substrate and the evaporation of the material.

For removing impurities and the oxide layer from the growth substrate, a penning ion sputter source (SPECS IQP 63) is used, indicated in Fig. 2.1 in purple. Ultra-pure argon is inserted through a leak valve in the ionisation chamber. Here, the gas atoms are ionised after interacting with a beam of electrons and are subsequently accelerated and focused on the surface of the substrate.

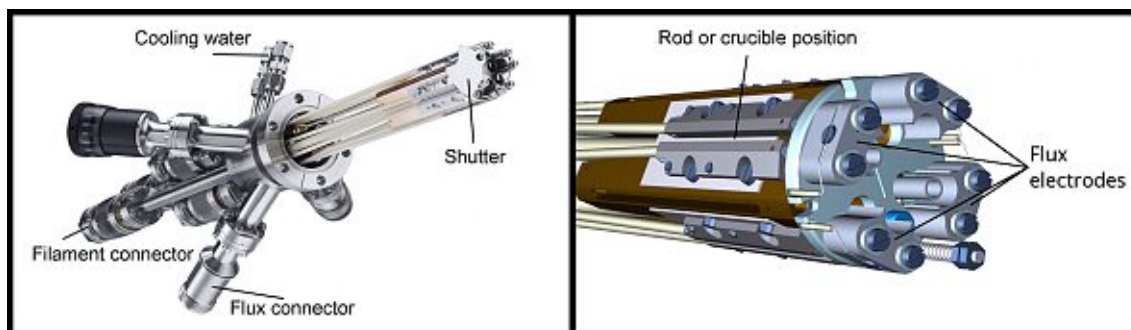


Figure 2.2: Images adapted from manual - SPECS [47]. Left: photo of EBE-4 evaporator; right: schematics of the vacuum side of the evaporator, with the sensor for flux measurement.

The evaporation of the materials is achieved using two different e-beam evaporators (shown in green in Fig. 2.1 and in detail in Fig. 2.2). The SPECS EBE-1 is equipped with a single rod of silicon, while the SPECS EBE-4 can be equipped with four crucibles (2 of tungsten (W), 2 of molybdenum (Mo)), for the evaporation of materials that melt before reaching a suitable vapour pressure. In both cases, an electron beam is directed against the target (rod or crucible), increasing its temperature. In order to control the rate of evaporation, the current of ionised atoms is measured by the application of a small bias at the vacuum side of the evaporator, as shown on the right of Fig. 2.2. This current (flux) is measured in units of nA and can be used as an indicator of a stable evaporation. It cannot be, however, used to compare the evaporation rates across different materials due to the different ionisation properties.

Materials available for evaporation are intrinsic silicon (Si), carbon (C), germanium (Ge) and calcium fluoride (CaF_2). Carbon has a very high melting point. For this reason it can be evaporated from a rod, but it requires high current and the obtainable fluxes are low. Germanium and CaF_2 , instead, melt before reaching a sufficiently high vapour pressure, thus these were inserted into a crucible for evaporation. Ge is evaporated from a Mo crucible, while CaF_2 is evaporated from a tungsten one. Silicon, instead, is in an intermediate range. It can be evaporated from a rod, however for obtaining higher fluxes it is necessary to partially melt the silicon rod, forming a molten drop at the tip, from where

Si atoms are evaporated. However, if the evaporation flux is increased significantly, the molten drop can fall from the rod, shortcircuiting the electrical connection in the evaporator. For this reason, the flux for Si is maintained constantly at low levels for all the experiments in this thesis.

2.2 Raman Spectroscopy

In this work, Raman measurements are performed using a Witec 300 confocal setup, always in a backscattering geometry. This equipment allows to perform spatially resolved measurements with sub- μm resolution by focusing the incident light (a 532 nm Nd:YAG laser) through objective lenses with a magnification up to 100x, and by collecting the scattered light through the same lenses. By using an achromatic Nikon EPI EPlan 100 \times objective (NA = 0.9, WD = 0.23 mm) it is possible to focus the laser down to a diffraction-limited spot size of ~ 720 nm. The incident light is linearly polarised and the polarisation angle, defined with respect to a common line in the sample plane, can be set between -90° and $+90^\circ$. The sample to be analysed is placed on a movable stage that allows to precisely control the position of the sample with respect to the incident light.

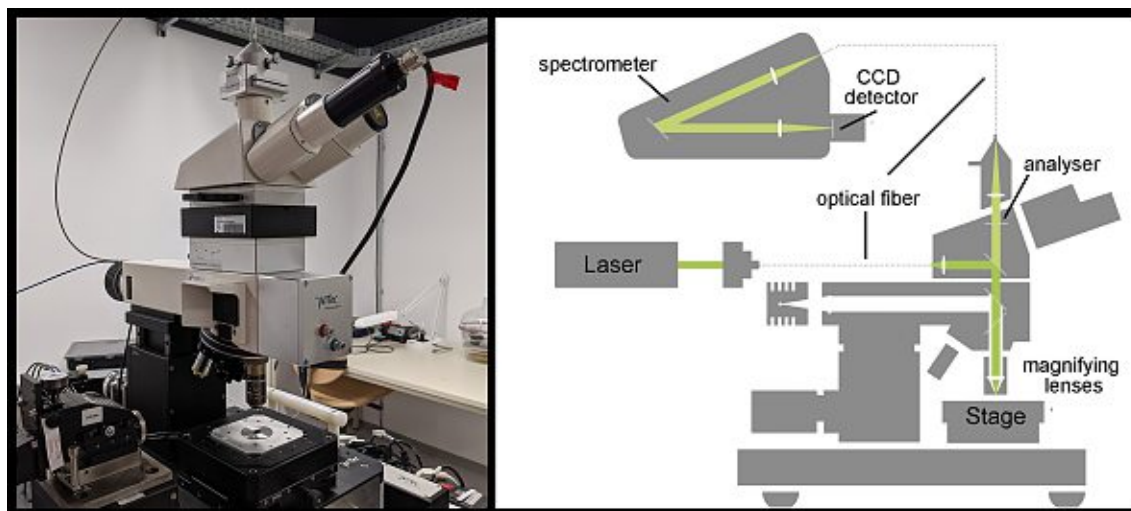


Figure 2.3: Left: photo of the confocal Witec 300 setup; right: schematics of the optical path - adapted from WITEC documentation [48]

In the right panel of Fig. 2.3 a schematic representation of the Witec setup is depicted. The optical path of the laser can be observed. The laser beam, guided by a single-mode fibre, passes a beam splitter with an integrated polariser and is focused onto the sample plane by optical lenses. The scattered light goes through the same lenses and then passes first through an analyser, which is used to select the analysed polarisation direction of the scattered light and then through a notch filter, that reduces the intensity of the Rayleigh-scattered light. Successfully, the beam enters the spectrometer, where it is divided in all its spectral components by a grating and finally is detected by a CCD detector. For detecting Raman modes with a small shift from the Rayleigh peak ($< 200 \text{ cm}^{-1}$), a Witec 500 setup is, instead, used. Thanks to an improved notch filter, it is possible to acquire Raman shift as small as 75 cm^{-1} . The working principle and the internal components are, however,

similar to what has been described for the Witec 300 setup. For all the measurements, the laser power has been kept at 1 mW. This choice allowed to acquire spectra with a satisfactory signal to noise ratio using relatively short integration times. This allowed to reduce the unwanted and potentially harmful heating of the analysed layers.

All the acquired Raman spectra are analysed using OriginLab. Generally, the data processing always follows these steps: firstly, a Savitzky–Golay filter is applied, to smooth out the raw spectra. Subsequently, a background removal is performed. Background data are either directly measured from a bare substrate or are generated through polynomial interpolation. The resulting spectrum can be fitted using Voigt functions, to better identify the position of the detected peaks.

2.3 Photoemission Spectroscopy

In this thesis three different types of photoemission experiments are performed. Two of them only collect the intensity of the electrons emitted at a certain kinetic energy, without acquiring data regarding their wavevector. Based on the type of used photon source, it is possible to distinguish between X-ray photoemission spectroscopy (XPS) and UV photoemission spectroscopy (UPS). The third method, called angle resolved UV photoemission spectroscopy, is capable of collecting also information regarding the wavevector of the emitted photoelectrons, allowing for a full mapping of the spectral function.

Within this work, photons are generated using two different sources.

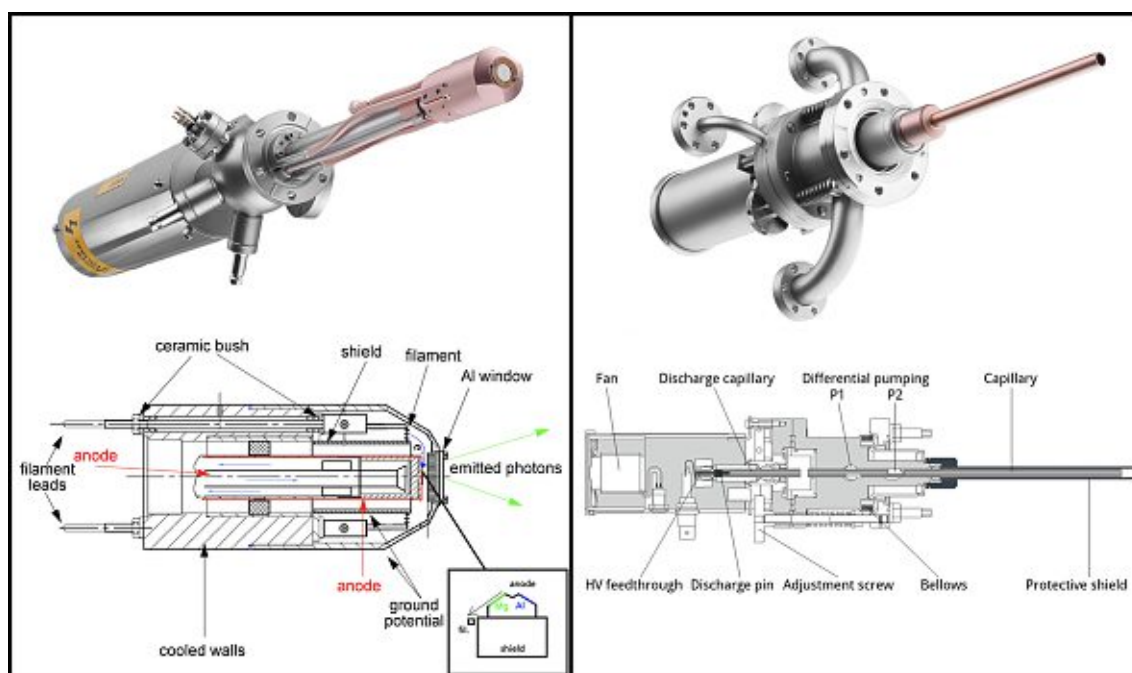


Figure 2.4: Images taken from SPECS manual [47]. Left: photo of a XR50 X-ray source, with schematic representation of the head components. Right: photo of a UVS 10/35 UV source, with schematic representation of its components.

X-ray photons are generated with a SPECS XR50 source, shown on the left of Fig. 2.4, which is directly mounted on the UHV system. The functioning principle is straight-

forward: a current is applied to a filament that emits electrons. These electrons are accelerated towards the anode due to a high voltage difference (0-15 kV). Within this source, two anodes are available. One is made of aluminium (Al), the other is a magnesium (Mg) anode. The electrons from the filaments generate K_{α} radiation lines at energies of 1486.6 eV (for Al) and 1253.6 eV (for Mg). The photon beam is then emitted out from the source and hits the sample. A small Al window is placed between the anode and the UHV chamber, with the goal of absorbing the stray electrons emitted from the filaments that are not directed to the anode.

UV photons, instead, are generated using a SPECS UVS 10/35 source, visible on the right of Fig. 2.4. A high purity noble gas is introduced in the source head, where its pressure is controlled via a leak valve. When the pressure of the gas is high enough, a discharge is started from a point anode, biased at high voltage. The discharge is led through a capillary by a differential pumping system, resulting into the emission of UV photons directly into the UHV chamber. For this thesis a high purity He gas is used, which produces photons at an energy of 21.2 eV (He I) and 40.82 eV (He II).

The photoelectrons excited using UV or XPS photons are collected by an analyser placed above the sample plane. The analyser used in this work is a Phoibos 150 high resolution spectrometer from SPECS.

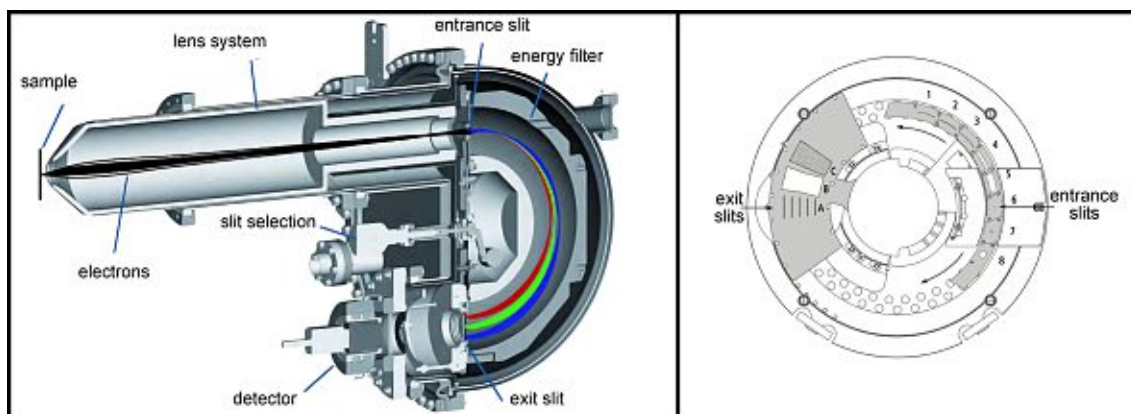


Figure 2.5: Left: cutaway drawing of a Phoibos 150 spectrometer. The path followed by the photoelectrons is highlighted. Right: schematic representation of the rings for the selection of the entrance and exit slits. Images taken from SPECS manuals [47].

A cutaway drawing of the analyser is shown in Fig. 2.5. The photoelectrons enter the analyser from the cylindrical column, which is set to the same reference potential as the sample (usually grounded). In the column, a series of lenses allow to guide and focus the photoelectrons on the plane of an entrance slit. The slit shape can be selected by rotating a large ring within the hemispherical analyser. All the available slits are shown in the right panel of Fig. 2.5. For the experiments of this thesis slit 5 is used for all the XPS experiments, while slit 2 is used for UPS and ARUPS experiments. Slit 5 has a rectangular shape with dimensions of $7 \times 20 \text{ mm}^2$, while slit 2 is also rectangular but with sizes $0.2 \times 20 \text{ mm}^2$. A larger slit allows to compensate for the lower intensity of the XPS source, compared to the UPS one, at the sacrifice of having slightly less spatial and spectral resolution. Besides being focused on the entrance slit, the photoelectrons are also

slowed down to a chosen energy value, defined *passing energy*. Once the electrons pass through the entrance slit, they enter the hemispherical part of the analyser. Here, thanks to a voltage difference between the inner and outer hemispherical caps, it is possible to select only those electrons that possess a certain kinetic energy. The selected electrons are allowed to pass through the exit slit which can be selected moving a circular ring as well. However, for all the experiments in this thesis, a slit of the type B (open) is chosen. Finally, the electrons hit the detector, where their intensity is measured. The detector is a 2D CCD detector from SPECS. This detector is composed by a surface of micro-channel plates (MCPs), which are capable of multiplying the incoming electrons. The multiplied electrons hit a phosphor screen, generating a light signal that is ultimately detected by a CCD camera.

Different modes can be selected through the choice of the lens mode. For XPS and UPS experiments, where the direction of the photoelectrons is not determined, it is possible to use the *Magnification Mode*. With this choice it is possible to perform spatially resolved studies of a sample. The analysed area depends on the choice of the lens mode and on the size of the entrance slit and can be calculated as $\frac{A_{slit}}{M}$, where A_{slit} is the area of the chosen slit and M is the magnification factor related to the chosen lens mode, which can vary between 2 and 10.

For ARUPS experiments, where it is necessary to determine the angular dispersion of the emitted electrons, an *Angular Dispersion Mode* is used, where the emission angle distribution is imaged. The lateral resolution is lost but the emission angle information is easily obtainable. The maximum acceptance angle can be increased from 3° up to 13° . In this way the wavevector of the emitted electrons can be directly measured by knowing its dispersion angle, as shown earlier.

Finally it must be noted that, in the used experimental setup, the rotation direction is perpendicular to the slit direction, as shown in Fig. 2.6. Since the maximum dispersion angle that can be measured directly is 13° , it follows that, for photoelectrons excited by He I photons, the maximum measurable value of $k_{//}$ in the direction of the slit is slightly smaller than 0.5 \AA^{-1} . By rotating the sample around the rotation axis shown in Fig. 2.6, it is possible to reach higher values of $k_{//}$. Unfortunately, since the slit is oriented in the opposite way, it is not possible to acquire the signal in one step. To solve this issue, one can acquire the signal at several rotation steps and then stitch all the data together. By keeping the rotation step as small as possible (1°), it is possible to minimise the loss of data between each step.

A MATLAB algorithm (reported in the Appendix) has been implemented in order to seamlessly stitch all the images together, as well as converting the angular data to $k_{//}$ (\AA^{-1}).

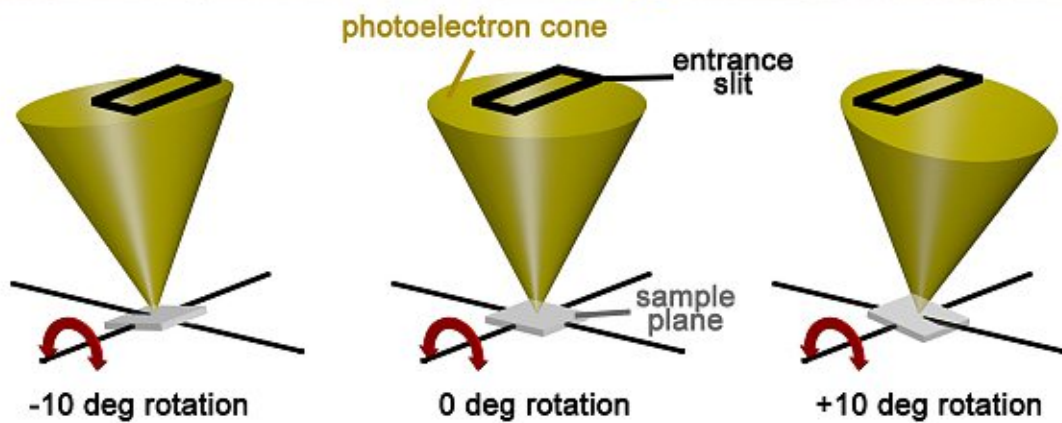
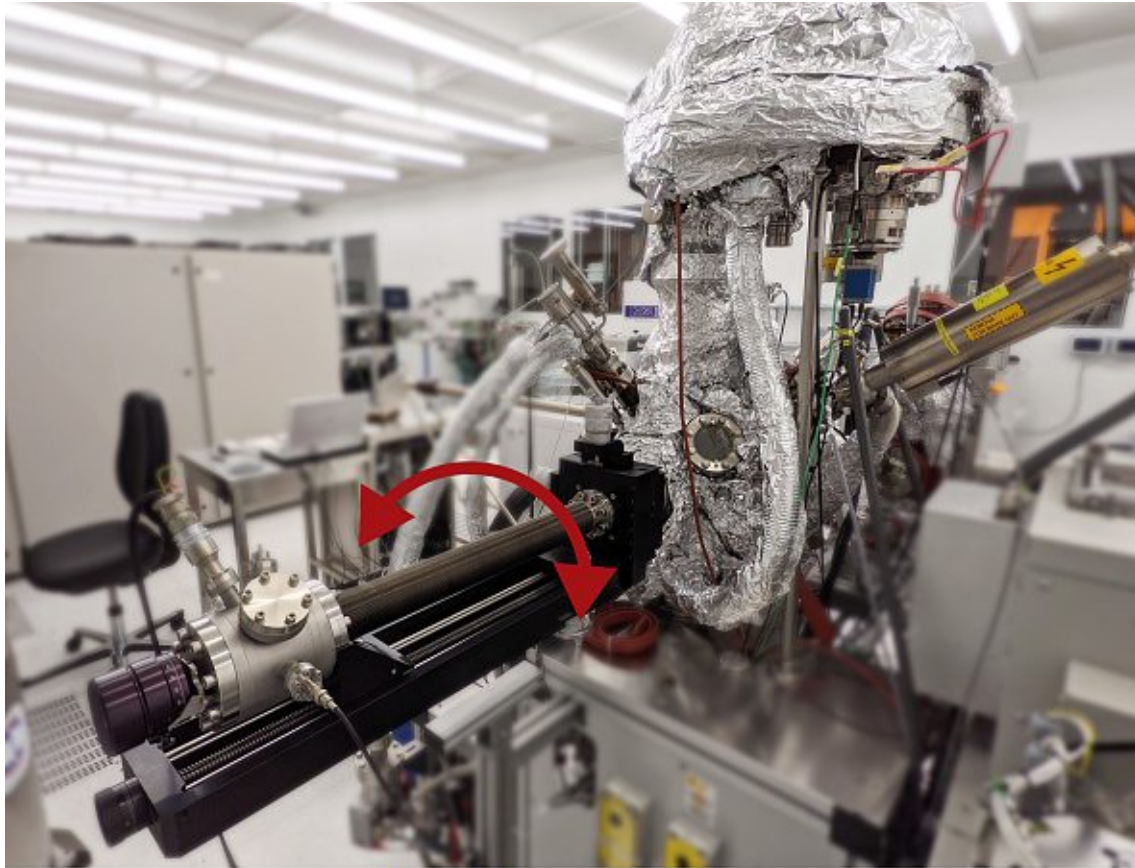


Figure 2.6: ARUPS measurements setup. Upper panel: photo of the sample manipulator. The red arrow shows the direction of the sample rotation. Lower panel: schematic representation of the orientation of the emitted electrons when the sample is rotated.

2.4 Low Energy Electron Diffraction

For performing Low Energy Electron Diffraction experiments an ErLEED 1000A (SPECS GmbH) apparatus is used, with direct access to the growth chamber.

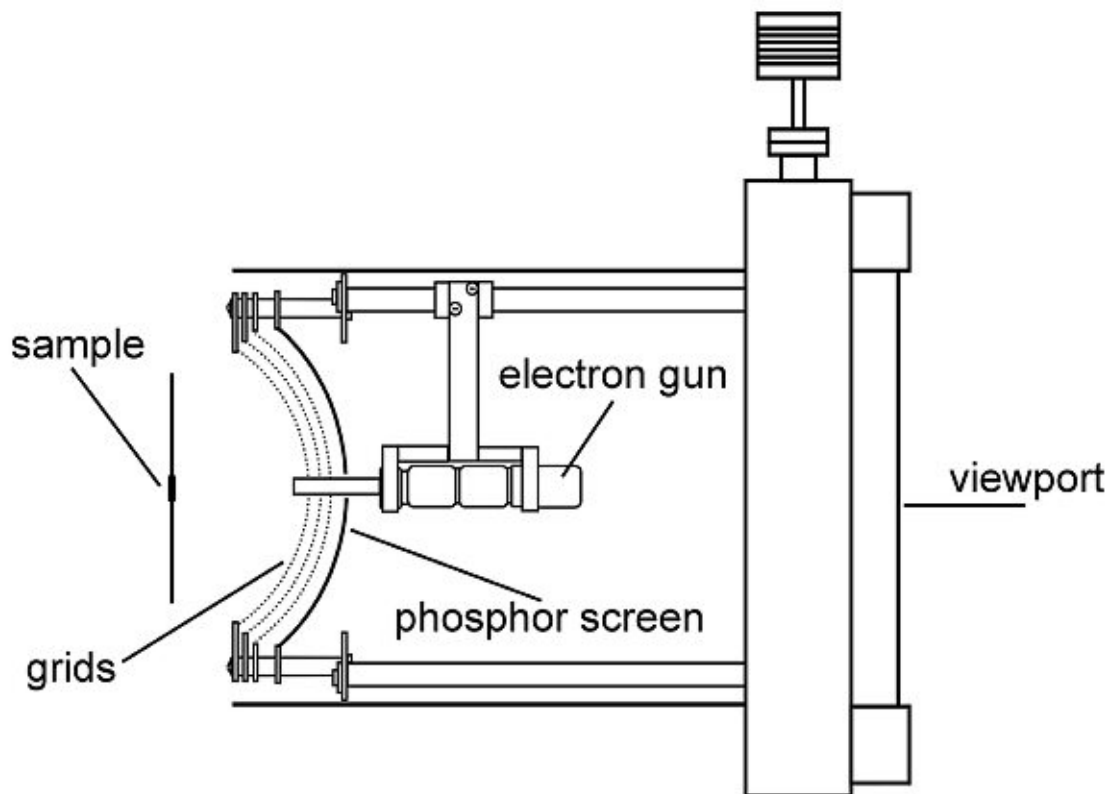


Figure 2.7: Schematic representation of the ErLEED 1000A apparatus used in this thesis. Image adapted from SPECS manual [47].

Figure 2.8 shows a schematic representation of the instrument. An electron gun is placed at the core of the unit. When a current (up to ~ 2.3 A) is applied to the LaB₆ coated filament, a beam of electrons is generated. The beam is focused by an electrostatic lens onto the sample's surface. Once the electrons are scattered back from the surface, they interfere with each other, forming a diffraction pattern. The scattered electrons pass through grids that eliminate the inelastically scattered ones (suppression grids) and accelerate the remaining electrons towards a phosphor-coated screen. The areas of the screen that are hit by electrons becomes luminescent, generating a signal that is captured by a CCD camera. The signal is acquired by a computer, directly connected to the camera. 200 raw images are acquired and averaged to increase the signal-to-noise ratio. Acquired patterns are analysed using LEEDLab software, which allows to simulate the diffraction patterns of superstructure grown on a crystalline substrate [49].

2.5 Low Energy Electron Microscopy

Low energy electron microscopy (LEEM) is a powerful technique that exploits a beam of low energy electrons to image surfaces with high spatial and temporal resolution [50]. In this thesis, LEEM images are acquired using a SPECS P90 microscope, located at the Central European Institute of Technology (CEITEC) in Brno, Czech Republic.

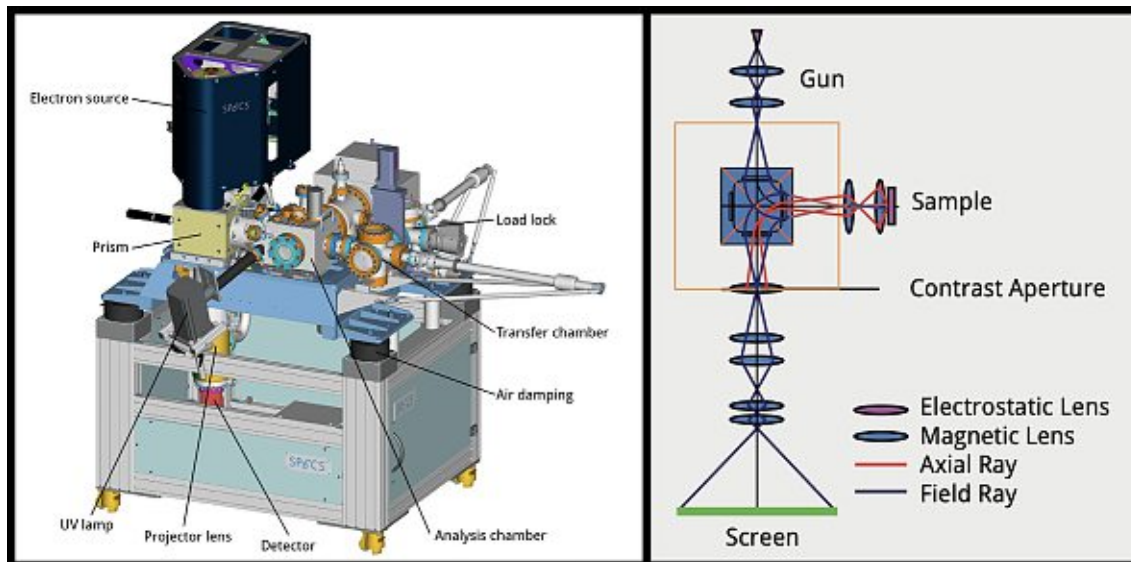


Figure 2.8: Left: representation of the LEEM microscope used in this thesis (SPECS P90). Right: schematic representation of the optical path of the electrons used for imaging the sample. Image adapted from SPECS manual [47].

The P90 microscope uses a cold field emitter to generate electrons, which are extracted to form a 15 keV electron beam. The electron beam is focused into the prism, a 90° magnetic deflector that serves as a beam splitter and imaging energy filter, by a set of magnetic lenses. At this point, a parallel beam of electrons is directed onto the surface of the sample. The sample is kept at a high negative potential of -15 kV, inducing a strong reduction of the electron energy down to few eV. After interacting with the surface, the electrons are accelerated back to 15 keV, entering the prism once again. Finally the electrons are focused onto a 2D detector, generating an image that can be acquired by a computer. The magnetic prism has the primary scope of separating the incident and reflected electron beam. At the same time, however, it corrects imaging errors, such as astigmatism, and serves as an imaging energy filter, effectively selecting the scattered electrons upon their kinetic energy.

LEEM is very versatile, allowing for different imaging methods: firstly, thanks to the complex projector lens system that focuses the electrons into the prism, the instrument is capable of imaging the sample both in real space and in k -space. Additionally, by slightly varying the sample potential, it is possible to change the type of interaction between the incident electrons and the sample, resulting in a different imaging method. Lastly, a series of apertures can reduce significantly the electron beam size, allowing for a detailed study of small regions of the sample.

The LEEM images shown in this thesis are acquired using both the real and k-space imaging configurations. In real space, the images are acquired using the *Reflectivity Contrast* method. This configuration exploits the fact that different areas on the surface show a different in electron reflectivity, resulting in a clear contrast difference. The energy of the interacting electrons is varied between 0 to 40 eV. In k-space, LEEM was used to acquire high quality LEED diffraction patterns, as well as microdiffraction patterns, obtained by restricting the electron beam size down to 185 nm.

2.6 Growth Parameters

For obtaining a successful epitaxial growth of silicene via MBE, a precise control of three main parameters must be obtained:

- Substrate Temperature
- Evaporation Rate
- Base Pressure and Substrate Preparation

2.6.1 Temperature Control

It is well reported that the temperature window for a successful growth of silicene on Ag(111) is quite narrow, with a target temperature that can be chosen between 200 °C and 300 °C. Within this range, different crystalline phases can be obtained based on the precise choice of temperature. Temperature has also been suggested as a key parameter for the successful realisation of multilayer silicene, which imposes even a more restrictive choice. For these reasons, temperature must be precisely and quickly measured through the whole growth process. In UHV systems, temperature can be reliably measured either using thermocouples, or via optical methods, using infrared pyrometry. High precision infrared pyrometry offers some advantages over thermocouples, with a much faster response and the capability of measuring a precise spot directly on the substrate surface or just aside of it, without requiring direct contact. In this work, the temperature of the sample is controlled via a high precision infrared pyrometer (DIAS DGE-10N), directly interfaced to the temperature controller (Eurotherm 100). For a precise temperature measurement, it is important to match the emissivity parameter of the pyrometer to the one of the examined surfaces. Polished metals (Ag and Au), however, are characterised by an extremely low emissivity (0.02-0.03), which is well below the instrument lower limit.

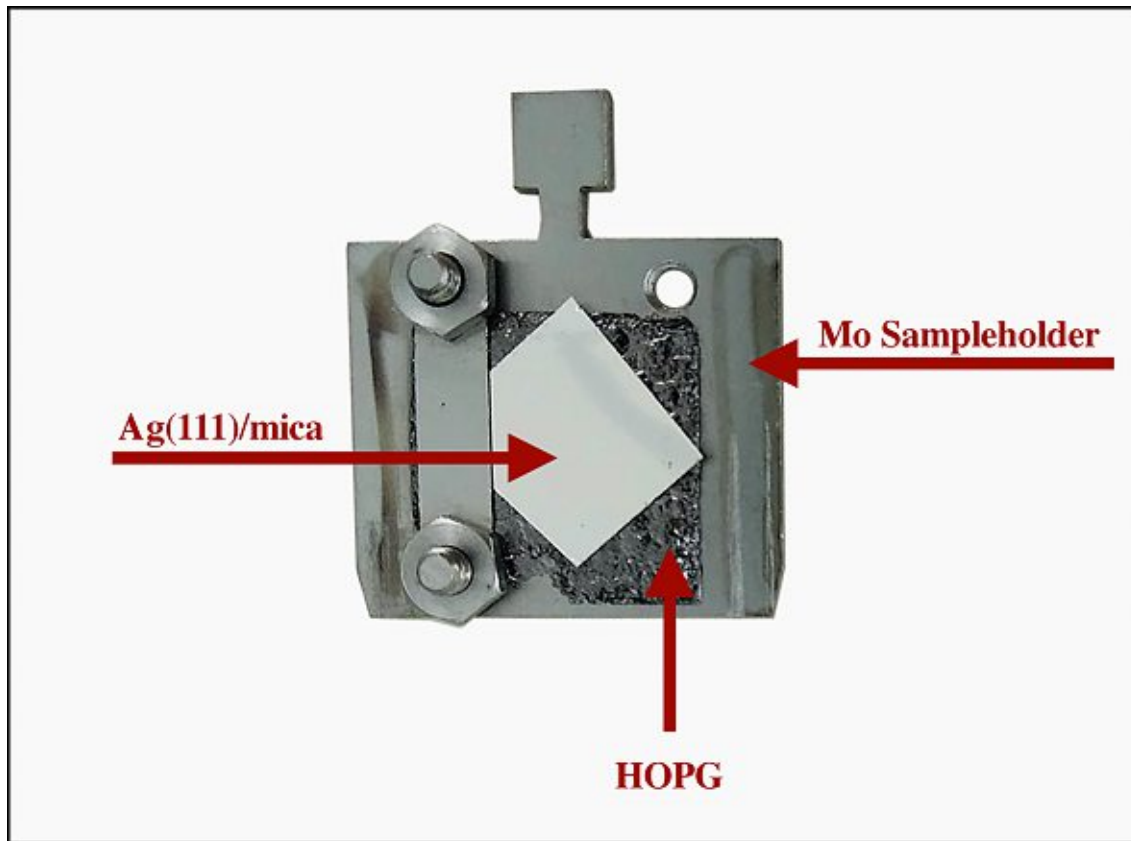


Figure 2.9: Ag(111)/mica substrate mounted on a Mo sample holder. An HOPG layer is placed between the substrate and the sample holder to act as a target for the pyrometer temperature reading.

To overcome this problem, the sample is always mounted on top of a Highly Oriented Pyrolytic Graphite (HOPG) layer, as shown in Fig. 2.9.

HOPG was chosen for two reasons: its in-plane thermal conductivity is extremely high and its emissivity is rather constant over a large range of temperatures [51, 52]. These two characteristics allow to quickly reach a uniform temperature all over the sample surface and to perform precise measurements under different conditions. In order to calibrate the pyrometer, the HOPG layer is heated at a well-known temperature on a hot plate and the emissivity parameter of the pyrometer is varied until the read value matches the reference. Following this procedure, the emissivity was set to 0.55, in close agreement with the expected value. Periodically, this calibration procedure is repeated to compensate for changes into the HOPG layer that could affect its emissivity. For the optimal temperature measurement, one has also to compensate for the absorption of the infrared spectrum caused by the viewport placed between the sample and the pyrometer. Common materials for UHV viewports, such as fused silica or borosilicate glass, are highly absorbing within the spectral range of the pyrometer (2 - 2.6 μm). For this reason, a sapphire (Al_2O_3) viewport is used, which benefits by a high transmissivity in the infrared region (90%). The pyrometer software allows to compensate for the low 10% absorption caused by the sapphire viewport, improving the measurement precision.

2.6.2 Evaporation Rate

The evaporation rate is obviously of extreme importance for the epitaxial growth of 2D materials. As explained earlier, this parameter not only determines the time needed for the formation of 1 ML but it is also a key factor for reaching suitable growth conditions. Flux and temperature must be coordinated carefully to promote a layer-by-layer growth, keeping in mind that different combinations can induce the formation of different metastable phases. Since the equipment lacks a suitable tool for the real-time monitoring of the evaporation rate (RHEED, Quartz Microbalance), a calibration is performed through *ex situ* measurements. Ellipsometry is a suitable tool for the determination of the thickness of evaporated films, even in the single-digit nanometer range.

In order to precisely measure the evaporation rate of the e-beam evaporator at a given flux, a thin film of silicon is deposited onto a piece of a polished Si wafer. This substrate is used for calibration purposes as it is exceptionally well modelled in ellipsometric analysis. The native oxide layer of the Si wafer piece is initially measured by using an ALPHA-SE spectroscopic ellipsometer (J.A. Woollam, spectral range: 380 nm - 900 nm), giving a value of 1.74 ± 0.01 nm. A thin layer of Si is then deposited on this substrate by evaporating at a fixed flux of 1 nA (see Methods) for 1.5 hours, with the substrate kept at a room temperature. After removal from the UHV chamber, the thin film is immediately analysed and the thickness of the silicon oxide is measured to be 2.86 ± 0.01 nm.

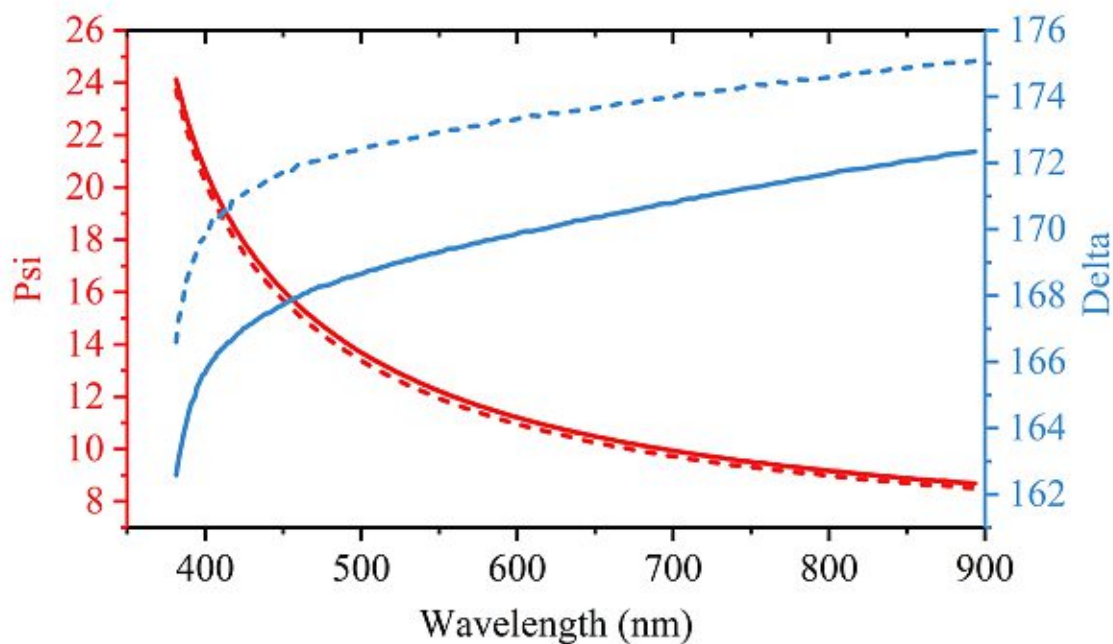


Figure 2.10: Ellipsometer data acquired before (dashed lines) and after (solid lines) evaporation of Si for 90 min.

The ellipsometric data (Psi and Delta) are reported in Fig. 2.10, with dashed lines showing the analysis performed before the Si deposition. Since the phase information (Delta) is very sensitive to films down to sub-monolayer thickness, it shows a large variation upon deposition of the Si film [53].

The deposited film is measured to be 1.12 ± 0.015 nm thick. This is, however, the thickness

of the oxide. The thickness of the deposited silicon can be estimated using a simple formula

$$h_{Si} = \frac{m_{Si}}{d_{Si}} \frac{h_{SiO_2} \cdot d_{SiO_2}}{m_{SiO_2}} \quad (2.2)$$

where m is the molar mass, d is the density and h the thickness. A final result of $\sim 0.59 \pm 0.01$ nm is obtained. Assuming a thickness of ~ 0.5 nm for 1 ML of amorphous silicon, it is possible to extrapolate a deposition rate of 0.013 ML/min for a flux of 1 nA. A finer tuning is achieved by comparing the obtained LEED image and Raman spectrum of silicene with literature data allowed to tune the evaporation rate at a more precise value of 0.022 ML/min for a flux of 1.3 nA.

2.6.3 Base Pressure and Substrate Preparation

Base pressure and substrate cleanliness are two strictly correlated concepts. The base pressure of the chamber must be carefully controlled for a successful growth of a silicene layer. As explicated earlier, in an MBE process the base pressure must be kept low to ensure a true molecular regime. Moreover, a bad base pressure will result in many impurities that will be incorporated into the grown material. For the growth of silicene this problem is even greater, as the reactivity of the layer is extremely high and the required evaporation rate is very low, resulting in long evaporation times. This means that the level of impurities must be kept at the lowest possible level, with a particular attention towards reactive species such as O_2 and H_2O molecules. As described in more detail in the previous section, the UHV system is equipped with 3 turbomolecular pumps and a Ti sublimation pump, which ensure that the vacuum levels can be kept as low as possible through the whole growth process. The base pressure, after a successful bakeout of the chamber, is as low as $3.5 \cdot 10^{-10}$ mbar. According to mass spectrometer measurements, the partial pressure of H_2O and O_2 species are, respectively, $3 \cdot 10^{-10}$ mbar and $1 \cdot 10^{-10}$ mbar. The minimum time for the substrate surface to get covered by an unwanted water layer can be estimated via the Hertz-Knudsen formula, as explained in Section 2.1. With the detected pressure levels, the minimum time - when the sticking coefficient is 1 - required for the formation of a layer of water in the UHV chamber is *circa* 7 hours. This ensures a sufficient time for a successful growth and characterisation of silicene.

The as-inserted substrate must be prepared to initially reach a suitable level of cleanliness, by removing adsorbed species and its native oxide layer. Additionally, the preparation process is also aimed at increasing the size of the surface terraces. Immediately after insertion into UHV, the substrate is gently heated to 200 °C for 15 minutes, to let all the adsorbate species detach. After this preparatory step, the substrate is exposed to repeated cycles of Ar^+ sputtering and annealing. The sputtering is achieved using the ion sputtering source IQP 10/63, which allows to accelerate a beam of Ar ions towards the sample. The beam profile can be controlled by varying the discharge bias (i.e. the ion energy) and is chosen to be large enough (5 mm radius) to avoid inhomogeneities on the sample. The sputter rate for Ag can be estimated with the formula

$$\frac{z}{t} = \frac{M}{\rho N_A e} S J_P \quad (2.3)$$

Where M is the molar weight of the substrate, ρ is its density, N_A is the Avogadro

number, e the electron charge, S a sputtering yield depending on the target material and J_P is the primary ion current density. The sputtering yield for Ag, at the chosen ion energy of 1 keV, is $S=5$. The beam radius at this energy, according to the datasheet, is 8 mm. Since the current is $3 \mu\text{A}$, the current density can be calculated as $150 \frac{\text{A}}{\text{cm}^2}$. This gives a sputtering rate of approximately $0.5 \frac{\text{nm}}{\text{min}}$. The substrate is sputtered for 5 minutes, effectively removing 2.5 nm from the substrate. This ensures that only the topmost surface is removed, keeping the substrate uniform. The sputtered substrate is subsequently annealed at a temperature of $520 \text{ }^\circ\text{C}$ for 15 minutes. At this temperature, the substrate atoms are able to diffuse along the surface, promoting the formation of wide terraces, ideal for the growth of silicene. The substrate surface after sputtering and after annealing has been imaged using LEEM.

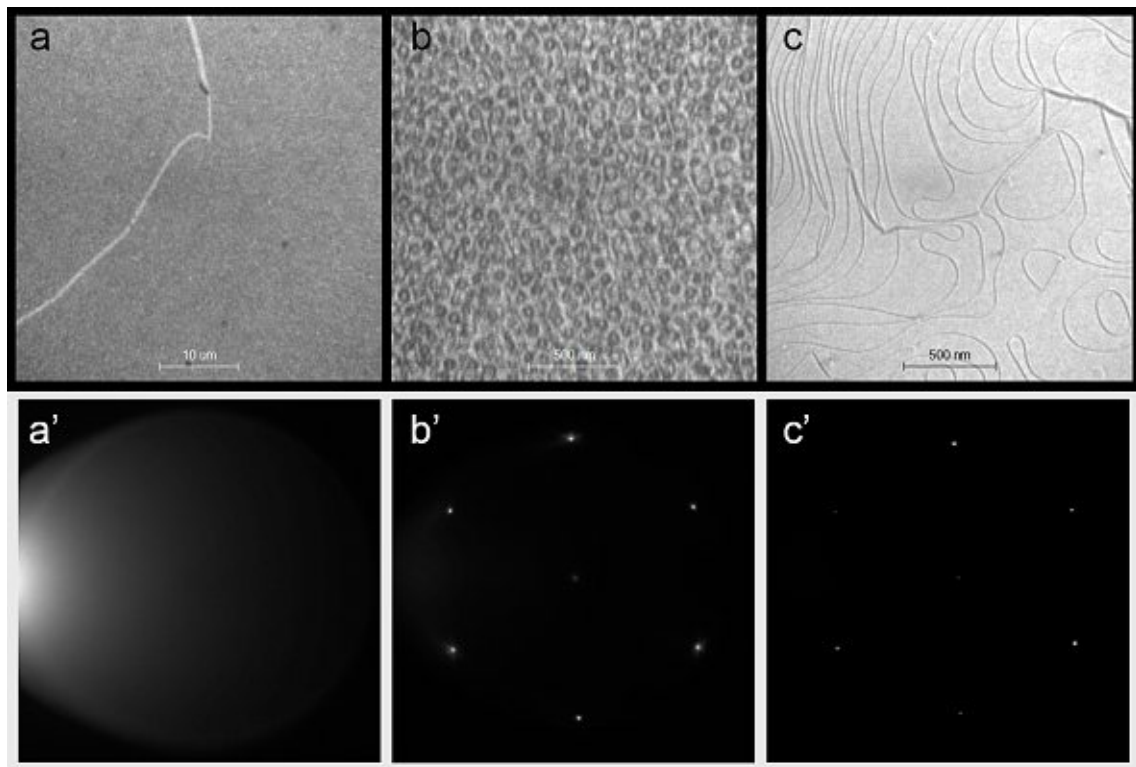


Figure 2.11: Bright field LEEM images and diffraction patterns of the Ag(111)/mica substrate a,a') as inserted into the UHV chamber, b,b') after 5 min of Ar^+ sputtering, c,c') after annealing at $520 \text{ }^\circ\text{C}$.

Fig. 2.11 shows the bright field images collected at an electron energy of 17 eV and the respective diffraction patterns, collected at an electron energy of 35 eV.

Clearly the substrate surface improves dramatically with just one cycle of Ar^+ sputtering and annealing. The substrate is initially characterised by having a grainy appearance, due to the presence on the surface of the native oxide layer (Fig. 2.11 a). The large scale is chosen to show the uniformity of the surface layer, which can be removed via sputtering. At this point no diffraction signal can be detected (Fig. 2.11 a'). After sputtering, the sample surface is heavily perturbed, as shown in Fig. 2.11 b by interaction with the Ar ions. Nevertheless, an already clear diffraction pattern can be detected, related to the intact crystal layers below the surface (Fig. 2.11 b'). After annealing (Fig. 2.11 c), large

terraces are formed, with some reaching a lateral size of almost $0.5 \mu\text{m}$. The diffraction pattern (Fig. 2.11 c') is clearly sharper, owing to the highly ordered surface. This procedure is then repeated twice, to get the best growth conditions. The surface condition is checked before any growth by LEED. A good surface will be characterised by clearly visible and focused diffraction spots, as shown in Fig. 2.11 c'.

2.7 *In Situ* encapsulation

Some of the results that will be discussed later will require to be able to analyse the silicene layer under ambient conditions. Contrary to graphene, this material is highly reactive and degrades extremely quickly. The time needed for the oxidation of 1 mm^2 of silicene has been estimated to be just $\sim 40 \text{ ns}$ [54]. An ideal passivation layer should possess the following properties:

- a superb impermeability towards oxidative species
- do not cause an alteration of the capped layer
- do not interfere with the methods used to analyse the capped layer

Ideal materials that fulfil all these requirements are inert 2D materials such as graphene and hBN. It has been demonstrated that these two materials are extremely impermeable [55, 56, 57]. At the same time it is well known that these materials are inert, with no dangling bonds at the surface. This is very important for the realisation of an interface that is not likely to degrade or change the structure of the encapsulated 2D layer. Encapsulation is required to analyse the silicene layers with Raman spectroscopy, in order to study their structural properties. Both graphene and hBN are compatible with this intent, as they both does not have any active modes in the expected region of interest for silicene. Due to the high reactivity of silicene, the encapsulation process must be performed immediately after the growth, without breaking the vacuum. In order to achieve this, one starts with hBN and graphite crystals. As a first step, these materials are exfoliated using the well-known adhesive tape method [58] on a Kapton (polyimide) tape with a silicone adhesive layer. Both the tape and the adhesive are compatible with UHV conditions since these materials show a very low outgassing even at extremely low pressures [59].

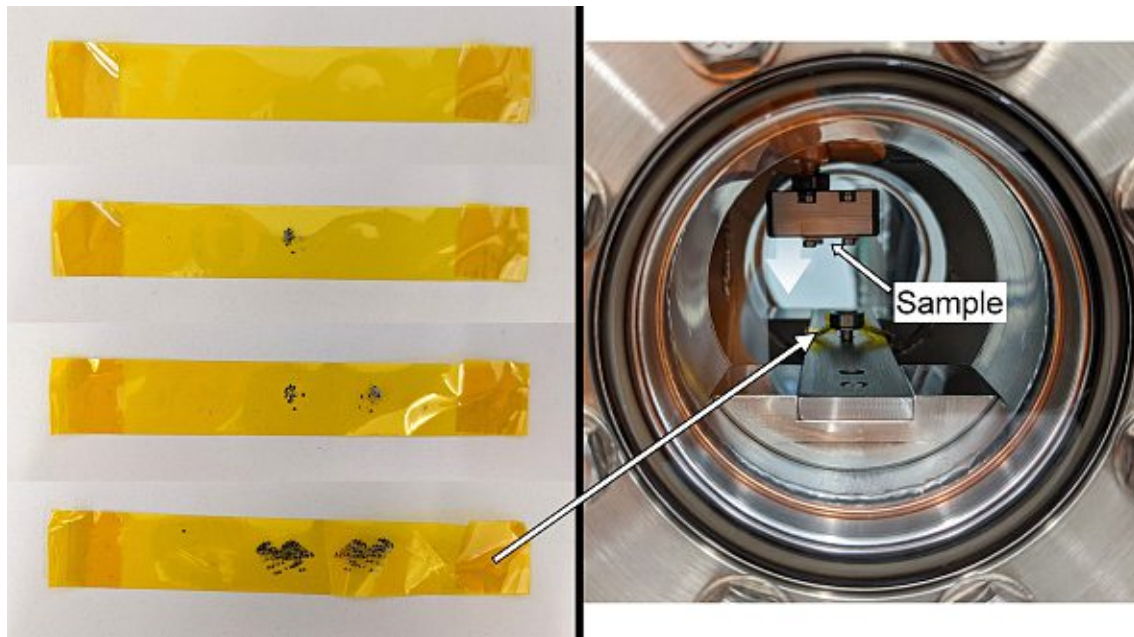


Figure 2.12: Left: graphite is exfoliated using a Kapton adhesive tape. Right: self built stamping apparatus; The tape, with exfoliated graphite is loaded on the spring-loaded holder in the centre. The sample is inserted, facing downwards, on the sample holder.

To perform the exfoliation, a small quantity of graphite or hBN crystals are dispersed on the adhesive side of the Kapton tape, as shown in Fig. 2.12. The crystals are then exfoliated by folding the tape and opening it again. This process is repeated 3-4 times, to get a large number of flakes on the adhesive tape. Once this is completed, the tape is loaded onto a self-built, UHV-compatible holder. The Kapton tape is fixed on top of a spring-loaded cylinder, with its adhesive side - and the exfoliated flakes - facing upwards. The chamber containing the tape is then evacuated using a small TMP. To remove the water layer adsorbed on the walls of the chamber and on the surface of the exfoliated flakes a bake out is performed.

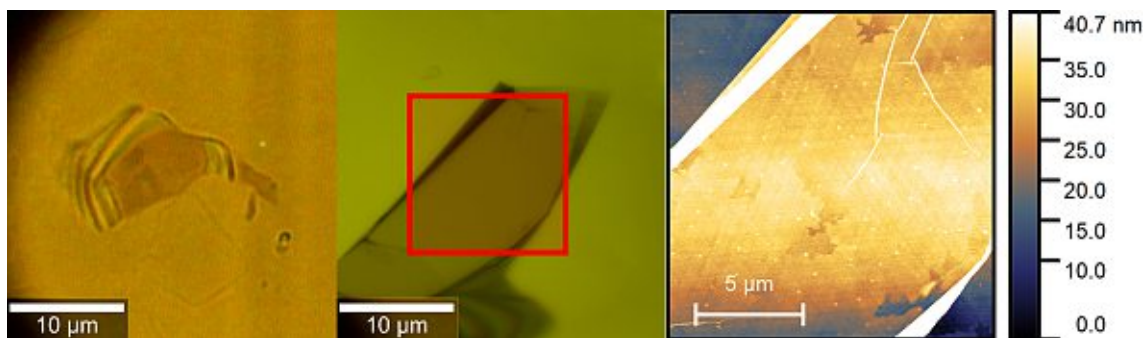


Figure 2.13: From left to right: optical image of few-layers hBN flake covering silicene on Au(111); adapted optical image of few-layers graphene flake covering silicene on Ag(111) - red square indicates region where flake was analysed by AFM; AFM scan of the few-layers graphene flake covering silicene on Ag(111) shown in the previous image.

As soon as the silicene growth is completed and the temperature of the sample is reduced below 150°C, the sample is moved into the encapsulation dedicated chamber and loaded into the sample holder facing downwards, towards the exfoliated flakes. The sample holder is attached to a XYZ-manipulator that guarantees its full movement. The sample is then pressed onto the tape and, subsequently, slowly separated. This causes some few-layers graphene or hBN flakes to exfoliate and remain attached on to the sample, covering the silicene layer and protecting it from oxidation. The flake adapts precisely to the layer below, as shown by the AFM scan in Fig. 2.13, where the imperfections of the Ag(111) substrate are visible through the capping flake. The encapsulation process allows to protect the silicene layer for up to about 72 h. During this time, some oxidative species are able to diffuse through cracks and wrinkles of the capping layer. Some of these imperfections are clearly visible also in the AFM scan of Fig. 2.13. Nevertheless, this result represents a huge improvement from the uncapped situation. This allows to perform *ex situ* experiments that would be otherwise impossible or that would require expensive and specific UHV-compatible equipment.

Chapter 3

Results and Discussion

In this chapter the obtained results, subdivided in three sections, are presented and discussed.

In the first section, the growth of silicene on Ag(111), at different substrate temperatures, is investigated. A large number of experimental techniques are combined to get a precise description of the grown layer, with a special focus on the investigation of its two-dimensional structure. The results are compared with literature data, to validate the growth technique.

In the second section, the analysis of silicene grown on Au(111) is presented. Once again, the 2D layer is investigated by combining different experimental techniques. The structure of the grown material is determined by confronting the results of the experiments with first-principle calculations.

The final section reports the results obtained regarding the epitaxial growth of crystalline CaF_2 on silicene, with the goal of exploring a viable process for the realisation of a dielectric layer directly interfaced on silicene. The interface is examined using the same combination of experimental techniques that was employed in the first two sections, exploring both the properties of the buried silicene layer and of the fluorite film.

3.1 Silicene on Ag(111)

3.1.1 Epitaxial Growth

Single-Layer Silicene

An Ag(111)/mica substrate with an area of $5 \times 5 \text{ mm}^2$ is mounted onto the sample holder and inserted into the UHV chamber. The surface is prepared, following the procedure outlined in section 2.6. Si evaporation is started by slowly increasing the filament current of the EBE-1 evaporator up to 5.3 A. As soon as the flux reaches the target value of 1.3 nA, the control on the filament current is switched to the internal automatic feedback loop. The evaporation is initially conducted, for several minutes, with the shutter closed, in order to protect the substrate from contamination from impurities desorbed initially from the Si rod. Meanwhile, the substrate temperature is increased to the chosen value. The shutter is then opened for 45 minutes, to let 1 ML of Si to deposit on the substrate. As mentioned earlier, temperature is a critical parameter for a successful growth of silicene

on Ag(111): the temperature window for the formation of silicene on Ag(111) is reported to be quite large, spanning from 150 °C to 300 °C [60]. Depending on the chosen temperature, different silicene phases are obtained. As described in section 1.4, the single layer phases can be described using the Wood notation or the Matrix notation. In literature, the different silicene/Ag(111) reconstructions are described using the Wood notation, either with reference to the substrate structure, or to an hypothetical freestanding silicene layer. In this work the different phases will always be described, when possible, by using the Wood notation with reference to the used substrate. Additionally, the Matrix notation of each phase, with respect to a virtual freestanding silicene layer, will also be introduced. This more general description allows to directly compare silicene phases grown on different substrates.

As soon as the growth is finished, the sample is cooled down to room temperature and the grown layer is analysed by LEED. Figure 3.1a and b show the diffraction patterns that are obtained for growths at a substrate temperature of 260 °C and 300 °C, respectively. Evidently, different reconstructions are obtained. In Panel a of Fig. 3.1, it is possible to observe the obtained diffraction pattern for the silicene grown at a substrate temperature of 260 °C. In panel a', the data are compared with a model generated using the software LEEDLab [49].

The model is composed by two phases: in green the 4×4 phase - matrix notation: $M_1 : \begin{pmatrix} 3 & 0 \\ 0 & 3 \end{pmatrix}$, while in blue the $\sqrt{13} \times \sqrt{13}$ R13.9° one, with

$$\text{matrix notation: } M_2 : \begin{pmatrix} 2.977 & 0.744 \\ -0.744 & 2.232 \end{pmatrix}.$$

The two phases are frequently observed together, as their formation energies are similar [60, 23]. The clear sharpness of the observed diffraction pattern is an indication of the high quality of the grown layer. It is well known that defects and crystallographic imperfection result in a broadening and weakening of the observed dots [61]. Panel b, instead, shows the reconstruction that is obtained for a growth temperature of 300 °C. Phase 4x4 can be detected also in this case, as indicated by the green dots in panel b'. At increased temperature, however, the $\sqrt{13} \times \sqrt{13}$ phase cannot be observed anymore. A new phase is formed, showing a $2\sqrt{3} \times 2\sqrt{3}$ R30° reconstruction - Matrix Notation: $M_3 : \begin{pmatrix} 3.0078 & 1.5039 \\ -1.5039 & 1.5039 \end{pmatrix}$.

This high temperature phase is represented by yellow dots in panel b'. In this case the diffraction pattern appears broader and weaker, denoting possibly higher amounts of defects and imperfections compared to the result obtained at a lower growth temperature, as confirmed by STM images [62].

As reported earlier, the $2\sqrt{3} \times 2\sqrt{3}$ phase become the most favourable only in extremely Si-rich conditions. A high temperature substrate can promote the surface mobility of Si atoms, leading to the formation of areas where the Si concentration is high, possibly explaining why this phase is observed at higher temperature growths.

Similarly to temperature, flux is expected to have an influence in the outcome of the growth process. These two parameters play an important role in determining the balance between the rate at which Si atoms impinge onto the Ag substrate and the speed of diffusion of the evaporated atoms onto the substrate surface. However, due to the technical limitations

of our configuration illustrated in Section 2.1, the flux cannot be easily varied, making temperature the only reliable parameter to tune the kinetics of the process.

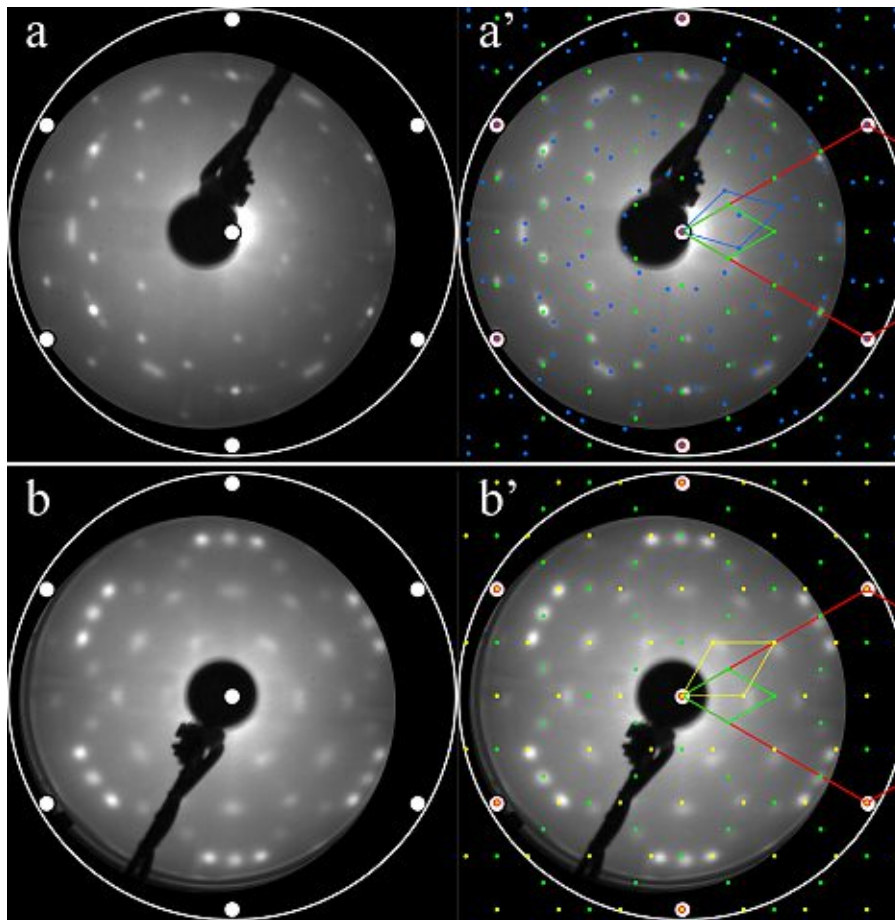


Figure 3.1: Diffraction patterns, collected with an electron energy of 35 eV, obtained after growing 1 ML of silicene on Ag(111) at different substrate temperatures. Panel (a) shows the result obtained by growing at a substrate temperature of 260 °C. This leads to the formation of two different phases. Panel (a') reports the simulation of the two phases in comparison with the obtained data. The green dots correspond to the 4×4 phase, while the blue dots are belonging to the $\sqrt{13} \times \sqrt{13}$ R13.9° one. The solid lines show the Brillouin zones of each phase, with the red one representing Ag(111). Panel (b) shows the result obtained at a higher growth temperature of 300 °C. The simulation in panel (b') shows the presence of 2 phases, with the green dots representing again the 4×4 reconstruction and the yellow dots indicating the $2\sqrt{3} \times 2\sqrt{3}$ R30°.

LEEM investigation of silicene growth

The epitaxial growth of silicene on Ag(111) was then investigated using LEEM.

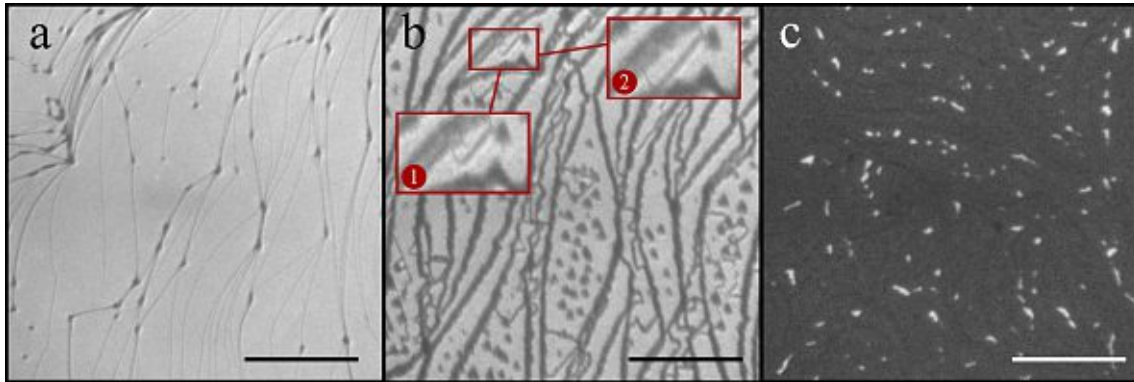


Figure 3.2: LEEM micrograph acquired during the growth of 1 ML silicene on Ag(111) at 260 °C. For all the images, the scale bar represents 1 μm . a) Ag substrate shortly after the beginning of Si evaporation, with distinct Ag step edges. b) Ag(111) surface with a Si coverage of approximately 0.2 ML. c) Ag(111) when Si reaches ~ 0.9 ML coverage.

LEEM micrographs for a growth at 260 °C are shown in Figure 3.2. In the first panel from the left, an almost clean Ag surface can be seen, with clear step edges. The silicene growth is clearly starting from these step edges, as indicated by the formation of small dark patches. As the evaporation progresses, the Si coverage increases to 0.2 ML, as shown in panel b. Silicene expands from the step edges, towards the inner parts of the Ag terraces. Additionally, the growth of small triangular islands within the terraces of the Ag substrate can be observed. Triangularly shaped islands are also reported regarding the growth of other 2D materials, such as hBN [63] and WS₂ [64]. In this case, the alignment of the triangles evidences a preferential orientation with respect to the substrate, in accordance with the diffraction patterns shown earlier. The insets in panel b evidence how step edges are moving during the evaporation of Si, possibly as an effect of the temperature or due to chemical interaction with the evaporated Si. As the evaporation is prolonged, almost full coverage is obtained, as evidenced by the micrograph of panel c (0.9 ML coverage). From the LEEM image it is not possible to determine whether a second layer has already started to form or not, due to a lack of contrast difference between the different Si layers. This possibility will be discussed later on.

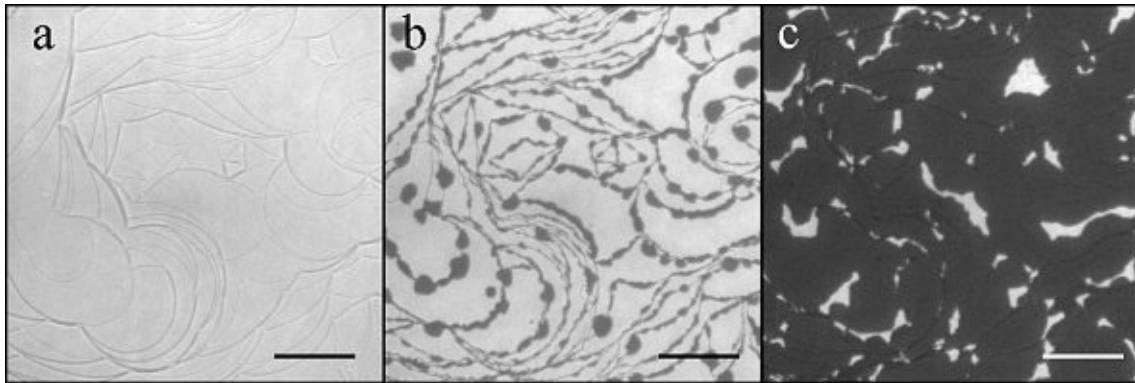


Figure 3.3: LEEM micrograph acquired during the growth of 1 ML silicene on Ag(111) at 300 °C. For all the images, the bar represents 1 μm . a) Bare Ag substrate before Si evaporation. Silicene grows from the step edges, with some darker areas appearing in b); c) Surface of the sample when Si coverage reaches 0.9 ML.

Interestingly, clear differences in the growth can be evidenced when the substrate temperature is raised up to 300 °C. As shown in Figure 3.3, silicene growth at this temperature still starts from the Ag step edges. However, within the Ag terraces, no sign of triangular shaped islands can be seen. At higher temperature Si diffuses faster on top of the Ag(111) surface, resulting in a growth that proceeds only from the seeds generated at the step edges. This clearly indicates the fragility of the balance between temperature, which governs the surface diffusivity of Si atoms on top of Ag(111), and flux. It is evident that, at higher temperature, silicene grows without following preferential directions, as evidenced by the formation of dark circular shapes, as opposed to the triangular geometries observed during the growth at 260 °C.

Growth of multilayer silicene

By proceeding with the Si evaporation, it is possible to exceed the 1 ML coverage. As explained in Sec. 1.1.1, silicene is predicted to be capable of forming a stable multilayer structure [65]. Experimental observations have reported the formation of a new, additional crystalline phase that can be observed for coverages exceeding 1 ML [66].

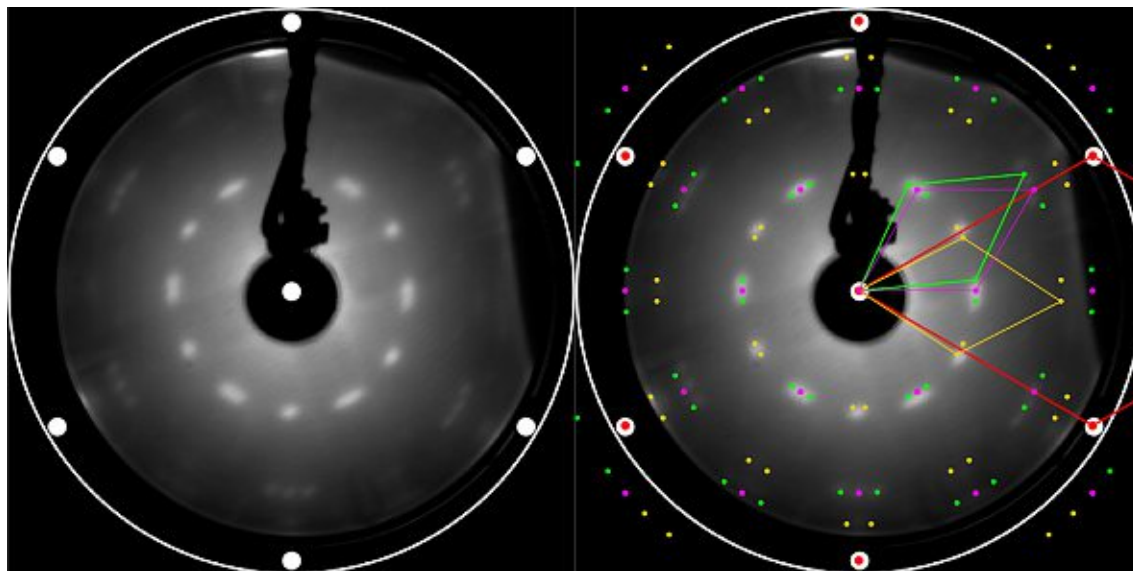


Figure 3.4: Left: diffraction pattern collected with an electron energy of 35 eV of a sample characterized by a Si coverage of nominally 3 ML, deposited on Ag(111) kept at a temperature of 260 °C. Right: diffraction model comprising three different phases is confronted with raw data.

The diffraction pattern obtained after growing nominally 3 ML silicene at a temperature of 260 °C is shown in Fig. 3.4. Clearly, the obtained pattern is different from the ones observed for a single-layer coverage. The diffraction spots can be perfectly modelled by considering the presence of a new $\sqrt{3} \times \sqrt{3} R30^\circ$ phase, indicated by the purple dots. Additionally, the same phase is also detected with different rotations, with respect to the Ag(111) substrate, as indicated by green (Rotation: 35.2°) and yellow (Rotation: 3°) dots. This result has been discussed in Ref. [67] as a consequence of the characteristics of the first silicene layer: as explained earlier, at this growth temperature, the first layer is composed by several different phases. In particular, it was demonstrated that the $\sqrt{13} \times \sqrt{13} R13.9^\circ$ phase grows on the Ag(111) surface with four different, but equivalent, rotational domains ($\pm 33^\circ$ and $\pm 5.2^\circ$) [68]. This indicates that the orientation of the initial layer greatly influences the arrangement of the final multilayer film. The nature of the $\sqrt{3} \times \sqrt{3}$ reconstruction of multilayer silicene has, however, sparked some debate around the interpretation of the experimental results. Simulations have predicted that, when additional Si is added to a freestanding silicene layer, it bonds at 1.38 Å above the top site of silicene, pushing the lower Si atoms downwards by the same amount. This new structure has been nicknamed *Dumbbell Structure*, and it is energetically favourable with respect to freestanding silicene. Moreover, the most stable arrangement of several of these Dumbbell units is expected to be forming the observed $\sqrt{3} \times \sqrt{3} R30^\circ$ reconstruction [69, 70, 71].

However, the same reconstruction has also been explained by assuming a different scenario: the additional silicon triggers the formation of diamond-like, sp^3 Si(111). Additionally, some of the Ag atoms from the substrate diffuse above these *bulk-like* Si clusters, forming the well-known $\sqrt{3} \times \sqrt{3}R30^\circ$ reconstruction of Ag on Si(111) [72, 73]. Interestingly, a difference can be detected in the lattice parameter of the structures grown by depositing several monolayers of Si on Ag(111) at two different temperatures (200 °C and 300 °C). The authors have interpreted those data as a sign that multilayer silicene is a metastable phase that can be grown only at low temperatures, otherwise forming Ag-terminated Si(111) [74]. LEEM analysis cannot resolve the conflict between *multilayer silicene* or *Ag-terminated Si(111)*, however the collected micrographs show a clear difference in the growth behaviour for the two different temperature regimes.

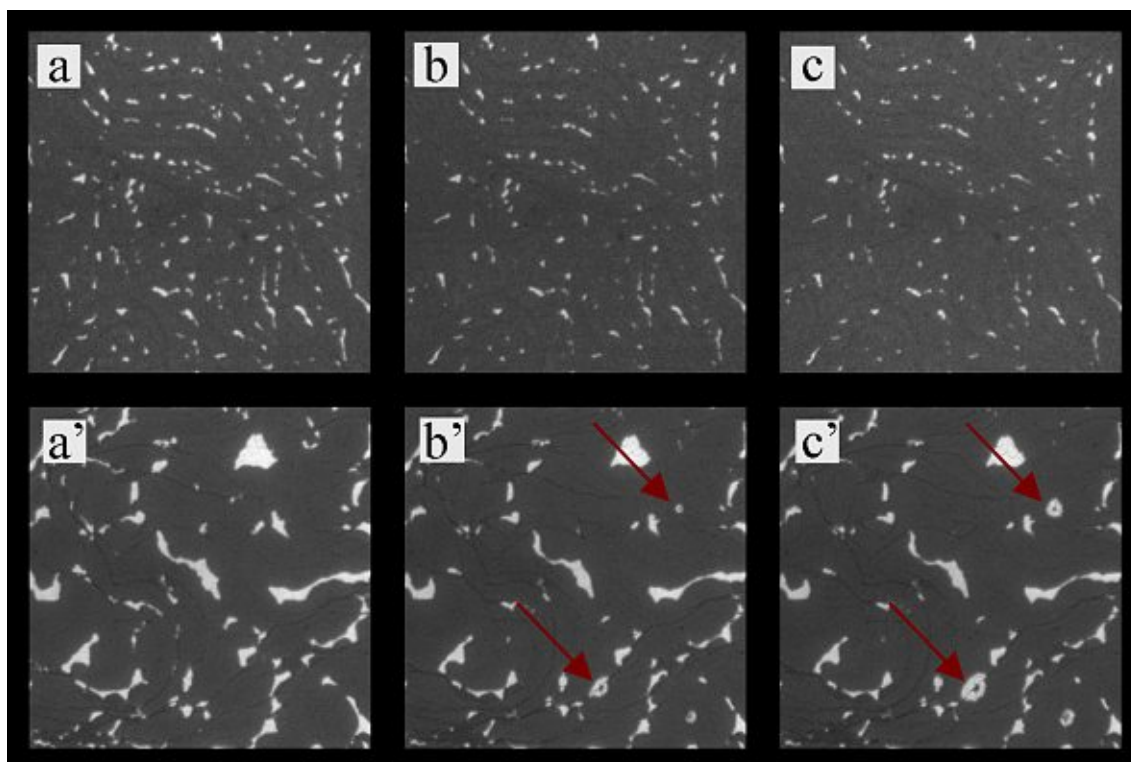


Figure 3.5: LEEM micrograph of the Si deposition prolonged above 1 ML coverage at 220 °C (a-c) and at 300 °C (a'-c'). Red arrows indicate, in the high temperature process, areas where the planar silicene structure seemingly *collapses* into a small cluster.

Fig. 3.5 shows LEEM micrographs taken during the deposition of Si on Ag(111) at a substrate temperature of 220 °C (top row) and of 300 °C (bottom row) and at a Si coverage close to 1 ML. The coverage of Si is increasing from left to right, with the same growth length between pairs of images (a-a', b-b', c-c'). The exposed Ag areas are clearly shrinking as the deposition is prolonged. Surprisingly, at the higher growth temperature, it is possible to observe, at certain positions, (indicated by red arrows) a clear collapse of the silicene structure. Circular areas of exposed Ag become larger as the Si deposition continues. The expansion of these circles is faster than the shrinking rate of the clean Ag areas due to the arrival of new Si atoms. Interestingly, at the center of these circular areas, it is possible to observe the formation of a dark, dot-like, features. Researchers at

the University of Twente had observed the same mechanism, for a substrate temperature of 270 °C and revealed that the dot features are bulk-like sp^3 silicon [75]. This intrinsic instability of silicene, that prevents the formation of a complete layer on Ag(111), is an indication of the unlikeliness of obtaining a multilayer silicene structure when growing at a substrate temperature of 300 °C. Interestingly, at lower temperatures, no such structural change can be observed, for a similar quantity of deposited silicon (see upper row of Fig. 3.5), marking a striking difference between what can be observed for a higher substrate temperature growth. To clarify, this observation is not supporting or refuting the existence of a multilayer silicene structure. It wants, however, to focus the attention on the striking different growth process that can be observed due to a variation in substrate temperature during an extended growth.

3.1.2 Photoemission Spectroscopy Measurements

X-ray Photoemission Spectroscopy

XPS measurements were performed using a non-monochromatic X-ray source ($\text{Al K}\alpha$), which emits photons with an energy of $E_\gamma = 1486.6$ eV and a line width of $\Delta = 0.85$ eV. The analysis has been focused on studying the Si2p peak, the most indicative for obtaining information regarding the chemical state of this material. For intrinsic, sp^3 Si, this peak is normally centred at a binding energy value of $E_{\text{Si}2p} = 99.4$ eV [76].

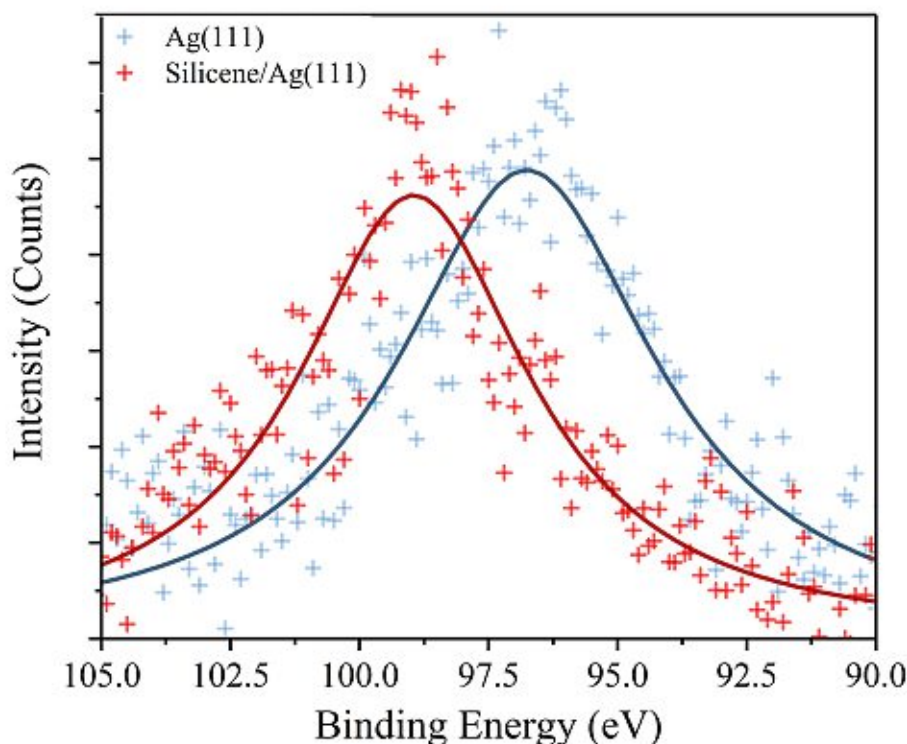


Figure 3.6: XPS analysis of: the clean Ag(111) substrate (blue); 1 ML silicene, grown on Ag(111) at a temperature of 260 °C (red) with a takeoff angle of 60°.

The result is shown in Fig. 3.6. The substrate was initially analysed before growing the silicene layer, as shown in blue. The detected peak is related to the 4s orbital of the Ag substrate. The fitting procedure consists in a first background removal step, accomplished by using a Tougaard model [77]. Subsequently, the peak is fitted using a Voigt profile, which is a function composed by a product of Gaussian and Lorentzian peaks. The result are reported in the Table 3.1.

Unfortunately the Ag4s peak is located in the vicinity of the expected Si2p peak. In order to correctly analyse the Si2p peak of silicene it is important to reduce the intensity of the Ag4s peak, thus reducing the overlapping. To accomplish this, the data are collected with a take-off angle of 60° - i.e. collecting the photoelectrons emitted at that angle - a configuration that maximises the intensity of the surface layer. The photoelectrons related

Ag4s Peak	Values (eV)
Center	96.76 ± 0.03
FWHM	6.08 ± 0.08

Table 3.1: Ag4s peak position and FWHM for Ag(111).

to the bulk have to travel a longer path within the material, due to the emission geometry and are more likely to be suppressed. The collected data are fitted again with a Voigt function, after the usual background correction. The fitting results for the Si2p peak are reported in Table 3.2.

Si2p Peak	Values (eV)
Center	98.95 ± 0.04
FWHM	5.4 ± 0.1

Table 3.2: Si2p peak position and FWHM for 1 ML silicene on Ag(111).

Interestingly, the position of the observed silicene Si2p peak is shifted by almost 0.5 eV to lower binding energies, if compared with the result commonly observed for intrinsic bulk silicon (99.4 eV [76]). This is in agreement with a previous report that detected the Si2p peak of silicene at 98.8 eV [78]. A similar shift can be also detected for carbon: the sp^2 hybridized carbon peak is centred at 284.3 eV, while the sp^3 one is located at 285.2 eV [79].

Angle Resolved UV Photoemission Spectroscopy

ARUPS measurements are carried out to analyse the electronic properties of the grown layer. Freestanding silicene is predicted to show a Dirac cone at the K and K' points of the Brillouin zone.

Based on this prediction, the most interesting direction to explore within the Brillouin zone is certainly the $\Gamma \rightarrow K$ one.

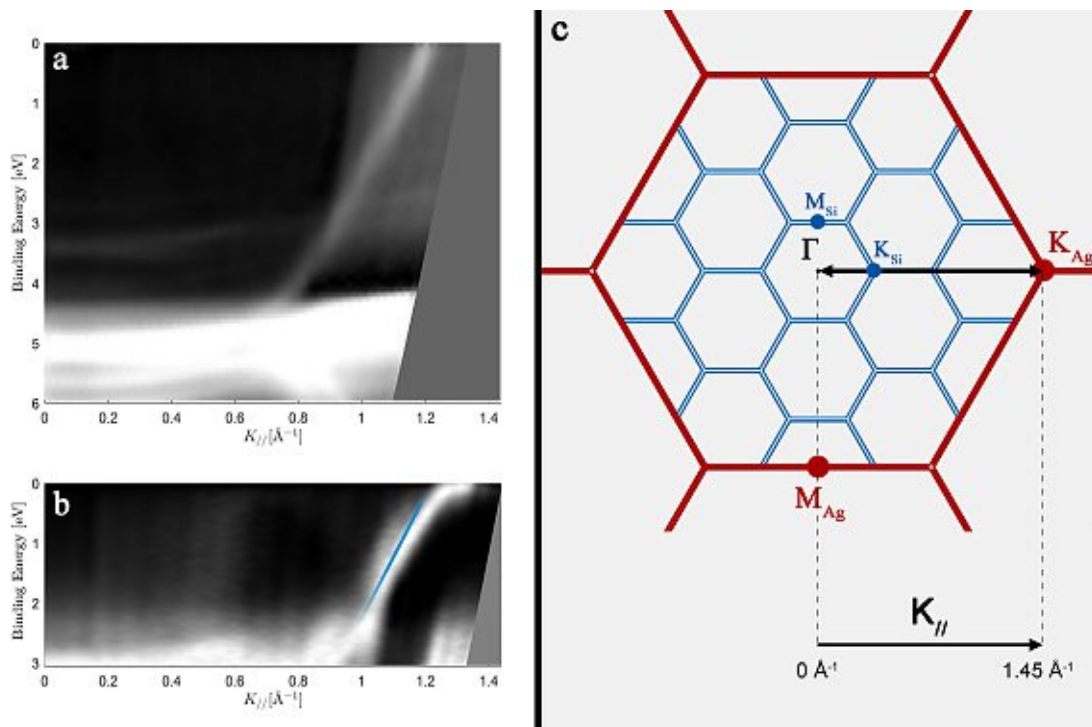


Figure 3.7: a) ARUPS analysis of the bare Ag(111) substrate. The scan direction is parallel to the $\Gamma \rightarrow K$ line. The position of the K_{Ag} point is $k_{\parallel} = 1.45 \text{ \AA}^{-1}$. b) ARUPS analysis of 1 ML silicene on Ag(111). The scan direction is the same as in a). The blue line indicates the position of the Ag-sp valence band. c) in blue, Brillouin zones of 4×4 phase of silicene; in red the 2D projection of the Brillouin zone of Ag(111) on the (110) plane. The black arrow indicates the direction of the scan.

Assuming the 4×4 phase of silicene on Ag(111) to be the most prevalent one, the Brillouin zone is expected to look like the sketch in Fig. 3.7 c. Obviously, as the unit cell of this silicene phase is, in real space, 4 times bigger than the one of Ag(111), the related Brillouin zone will be 4 times smaller, as shown in blue. The black arrow indicates the scan direction.

Initially, the analysis is performed on the clean Ag(111) substrate. Due to the current limitations of the experimental system, the data are composed by a collection of several spectra, one for each rotation angle, stitched together using the MATLAB script shown in the Section 4. For this analysis, He I photons are used, with an energy of 21.2 eV. The spectrum is collected using a rectangular slit with dimensions $1 \times 20 \text{ mm}^2$, an energy

resolution of 20 meV, a passing energy of 2 eV and a exposure of 0.1 s for each energy step. The results are shown in Fig. 3.7 a. The typical Ag-related bands are brightly appearing in the binding energy region that spans from 6 to 4 eV. The parabolic Ag-sp valence band is clearly recognisable, crossing the Fermi level at around $k_{//} = 1.2 \text{ \AA}^{-1}$. The position of the K_{Ag} point, relative to the 2D projection of the Ag Brillouin zone on the (111) plane, is, instead, at $k_{//} = 1.45 \text{ \AA}^{-1}$. After the deposition of a silicene layer, the ARUPS measurement is repeated, using the same parameter. The result is displayed in Fig. 3.7b. The lower binding energy region is still dominated by the filled Ag bands and thus here omitted. The collected spectrum does not show a dramatic change: a seemingly linear band, slightly shifted with respect to the position of the Ag-sp valence band (indicated by the blue line), reaches the Fermi level at $k_{//} = 1.3 \text{ \AA}^{-1}$, here flattening. This result is very different from the expected spectrum of freestanding silicene, showing a loss of the Dirac signature. The band detected after the deposition of 1 ML of silicon is very close to the sp band of Ag(111) and can be related to hybridisation of Si with Ag orbitals, as proposed by Tsoutsou et al. [80], which observed a similar behaviour. Indeed, hybridisation between Si and Ag is to be expected, as suggested by calculations of the band structure of silicene on Ag(111) [81]. The appearance of similar bands can be also confirmed along the other K and K' points of the Brillouin zone. It was possible to demonstrate that the band appearing upon deposition of 1 ML silicene does not shift when changing the energy of the excitation photons, while the Ag-sp band does [80]. This striking difference is relative to the 2D nature of the additional bands: surface states do not disperse with k_{\perp} , which depends on the photon energy. On the other side, the Ag-sp band depends upon the perpendicular component of the k vector, thus being sensitive to a change in the photon energy.

These results clearly indicate that Ag(111) has a strong, unwanted influence on the electronic structure of silicene. Unfortunately, this heavy interaction between Si and Ag atoms leads to the destruction of the Dirac signature predicted for freestanding silicene.

3.1.3 Vibrational Properties

The structural properties of silicene on Ag(111), from 1 to 2 ML coverage, are investigated in detail by confocal polarized μ -Raman spectroscopy. For ex situ measurements, silicene must be effectively protected from rapid oxidation. This is achieved by in situ encapsulation by few layer graphene flakes described in section 2.7.

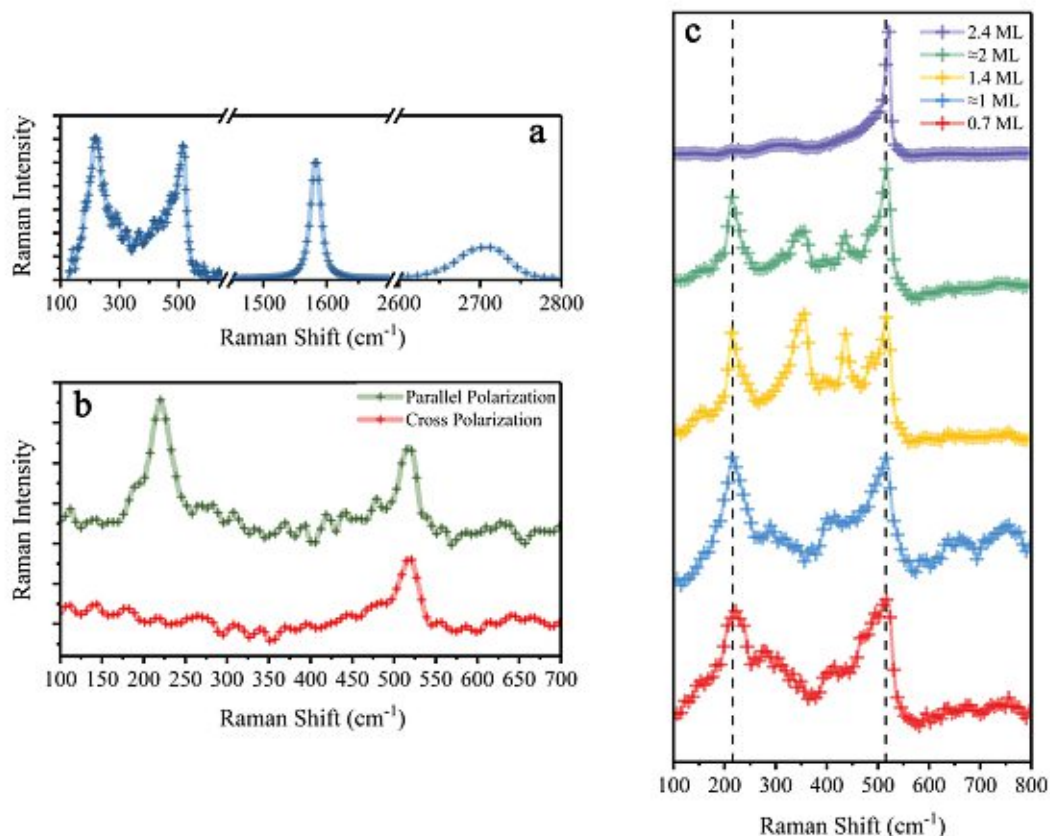


Figure 3.8: a) Raman spectrum of 1 ML of silicene on Ag(111) encapsulated under a few-layer graphene flake. b) Polarised Raman spectrum, collected in parallel polarisation configuration (green) and in cross polarisation configuration (red). c) Raman spectra of samples with an increasing silicon coverage, from ~ 0.7 ML up to ~ 2.4 ML. The intensity of the ~ 2.4 ML coverage spectrum is reduced in the plot by a factor of 1000.

The Raman spectrum of 1 ML silicene on Ag(111), encapsulated under a few-layer graphene flake and analysed 30 minutes after removal from the UHV system, is shown in Fig. 3.8 a. Alongside the well-known G (~ 1580 cm^{-1}) and 2D (~ 2700 cm^{-1}) peaks associated to the capping graphene flake, two additional peaks characteristic for silicene are detected, centred at 216 cm^{-1} and 515 cm^{-1} . It must be noted that the detected modes are much different from the predicted ones for freestanding silicene, which are expected at 175 cm^{-1} and 566 cm^{-1} [82, 83], however they are in good agreement with previous in-UHV Raman measurements and with the results of first principle calculations [84]. This is a clear indication that silicene grown on Ag(111) is structurally different from the freestanding layer, due to the interaction with the substrate. The calculations results allow to propose an identification for the 216 cm^{-1} peak, relating it to the out-of-plane vibrational mode of

this structure, while assigning the 515 cm^{-1} to the doubly degenerate in-plane vibrations. Additional structural information can be obtained by performing a polarised Raman analysis.

As explained earlier, the 4×4 silicene is a high symmetry phase, belonging to the C_{6v} point group. This group possesses three possible phonon symmetries, $A(z)$, E_1 and E_2 , which are described by the following Raman tensors:

$$A(z) : \begin{pmatrix} a & 0 & 0 \\ 0 & a & 0 \\ 0 & 0 & b \end{pmatrix}, E_1 : \begin{pmatrix} 0 & 0 & c \\ 0 & 0 & c \\ c & c & 0 \end{pmatrix}, E_2 : \begin{pmatrix} d & -d & 0 \\ -d & -d & 0 \\ 0 & 0 & 0 \end{pmatrix}$$

This means that, depending on the direction of the polarisation, the $A(z)$ vibrational mode can be visible or completely suppressed.

In a parallel polarisation configuration $\theta_i = \theta_s$, while in cross polarisation configuration $\theta_i = \theta_s + \frac{\pi}{2}$. From this follows that:

$$I_{A_{//}} \propto |\langle P_i | A(z) | P_s \rangle|^2 = \left| \left\langle \begin{pmatrix} \cos(\theta_i) \\ \sin(\theta_i) \\ 0 \end{pmatrix} \middle| A(z) \middle| \begin{pmatrix} \cos(\theta_i) \\ \sin(\theta_i) \\ 0 \end{pmatrix} \right\rangle \right|^2 = |a \cdot \cos^2(\theta_i) + a \cdot \sin^2(\theta_i)|^2 = a^2$$

$$I_{A_{\perp}} \propto |\langle P_i | A(z) | P_s \rangle|^2 = \left| \left\langle \begin{pmatrix} \cos(\theta_i) \\ \sin(\theta_i) \\ 0 \end{pmatrix} \middle| A(z) \middle| \begin{pmatrix} \cos(\theta_i + \frac{\pi}{2}) \\ \sin(\theta_i + \frac{\pi}{2}) \\ 0 \end{pmatrix} \right\rangle \right|^2 = |a \cdot \sin(\theta_i) \cdot \cos(\theta_i) - a \cdot \sin(\theta_i) \cdot \cos(\theta_i)|^2 = 0$$

The sample with a coverage of 1 ML silicene has been investigated in parallel and cross polarisation configuration. As shown in Fig. 3.8 b, the two characteristic silicene modes are both visible in the parallel configuration (green spectrum). However, when the analyser is rotated by 90° , the mode located at 216 cm^{-1} is completely suppressed (red spectrum). This clearly indicates that the out-of-plane vibrational mode can be assigned to phonon symmetry $A(z)$, while the 566 cm^{-1} peak belongs to the E_2 phonon symmetry. No peaks with an E_1 phonon symmetry can be detected as they are always invisible in a backscattering geometry [85]. It must be noted that the observation of a Raman mode with an "A symmetry" is of great importance as it confirms that the observed spectrum is related to a high-symmetry silicene phase. Since this kind of phonon mode is related to an out-of-plane vibration, it cannot be observed in bulk silicon structures but only in a 2D layer where the translational symmetry along the z-axis is broken. For this reason, the observation of such a vibrational mode is a solid proof of the two-dimensionality of the analysed layer.

Interestingly, different Raman signatures are observed when the silicon coverage is varied, as shown in Fig. 3.8 c. When the coverage is increased, two additional sharp peaks appear in the spectrum, at $\sim 350 \text{ cm}^{-1}$ and $\sim 450 \text{ cm}^{-1}$. Interestingly, the intensity of the additional peaks lowers for a higher silicon coverage. This might indicate that these additional Raman peaks are related to edge-activated modes of a second layer growing on top: as the coverage is increased, larger portions of the sample are covered by a second layer and the edges are scarcer. Nevertheless, it cannot be excluded that these additional modes are the signature of a drastically modified structure caused by the presence of

additional Si atoms, as proposed by Cahangirov et al. [69] or of an ordered layer of Ag atoms that have diffused on top of silicene [86]. Finally, when the coverage exceeds 2 ML, a Raman spectrum similar to the one of bulk silicon is detected, characterised by a pronounced peak centred at 520 cm^{-1} . Interestingly, the intensity of the signal is ~ 1000 times higher than what observed for lower coverages: this dramatic change is an indication of a phase transition towards a sp^3 -hybridised bulk-like structure, matching what was observed in LEEM micrographs (Fig. 3.5).

3.2 Silicene on Au(111)

As evidenced by the data presented in the previous section, Ag(111) is a substrate that offers an ideal platform for the investigation of many properties of silicene, thanks to the almost perfect epitaxial matching conditions and to the relative small number of different phases that can be obtained. However, the strong hybridisation between Si atoms and Ag orbitals leads to a complete loss of the Dirac nature of the electrical properties of the 2D layer. Recently, several reports hinted at the possibility of obtaining a silicene phase on Au(111) [87, 88]. Additionally, ARUPS measurements evidenced the possibility of having an intact Dirac cone in the electronic structure of the grown layer [88]. However, no clear information is given on the structural properties of the obtained structure, with contrasting models across different papers. For these reasons a full characterisation of the grown structure obtained by combining diffraction and Raman analysis would be of great importance.

3.2.1 Epitaxial Growth

Similarly to the case of silicene on Ag(111), the substrate is constituted by a thin Au(111) film (300 nm), grown on mica (MaTeK GmbH). The preparation of the substrate is achieved by following the same procedure used for Ag(111), as outlined in section 2.6. Once the surface of the sample is cleaned, its quality is checked by LEED analysis.

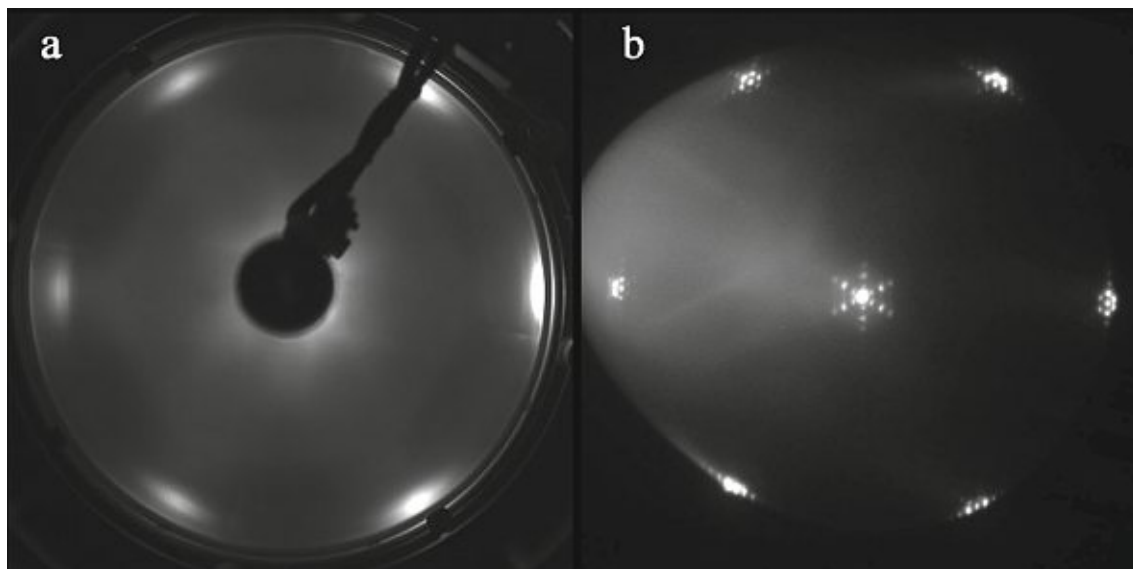


Figure 3.9: a) Diffraction pattern obtained with the LEED apparatus from a $\approx 1\text{ mm}^2$ area of the cleaned substrate. b) μ -diffraction pattern obtained with LEEM.

The obtained LEED pattern, shown in Fig. 3.9 a, is characterised by rather large diffraction spots. This is principally caused by two factors: the existence of several domains on the surface that do not share precisely the same orientation, giving rise to slightly rotated diffraction peaks and the peculiar reconstruction of clean Au(111), known as *herringbone reconstruction*, where 23 Au surface atoms fit into 22 lattice sites by a compression of the top layer along the close-packed $[110]$ direction, giving rise to a $22 \times \sqrt{3}$ reconstruction that cannot be resolved well with the large area LEED equipment. Differently, when a μ -diffraction pattern of the same sample is acquired using LEEM, sharp peaks appear and the surface reconstruction is well recognisable, as shown in Fig. 3.9b. This confirms the good quality of the substrate while, however, evidencing the need of performing diffraction analysis on a small area to be able to get meaningful results.

The growth of silicene on Au(111) follows exactly the same procedure as for Ag(111): after the cleaning of the substrate, 1 ML of silicon is evaporated onto the Au(111) surface, kept at a temperature of 260 °C.

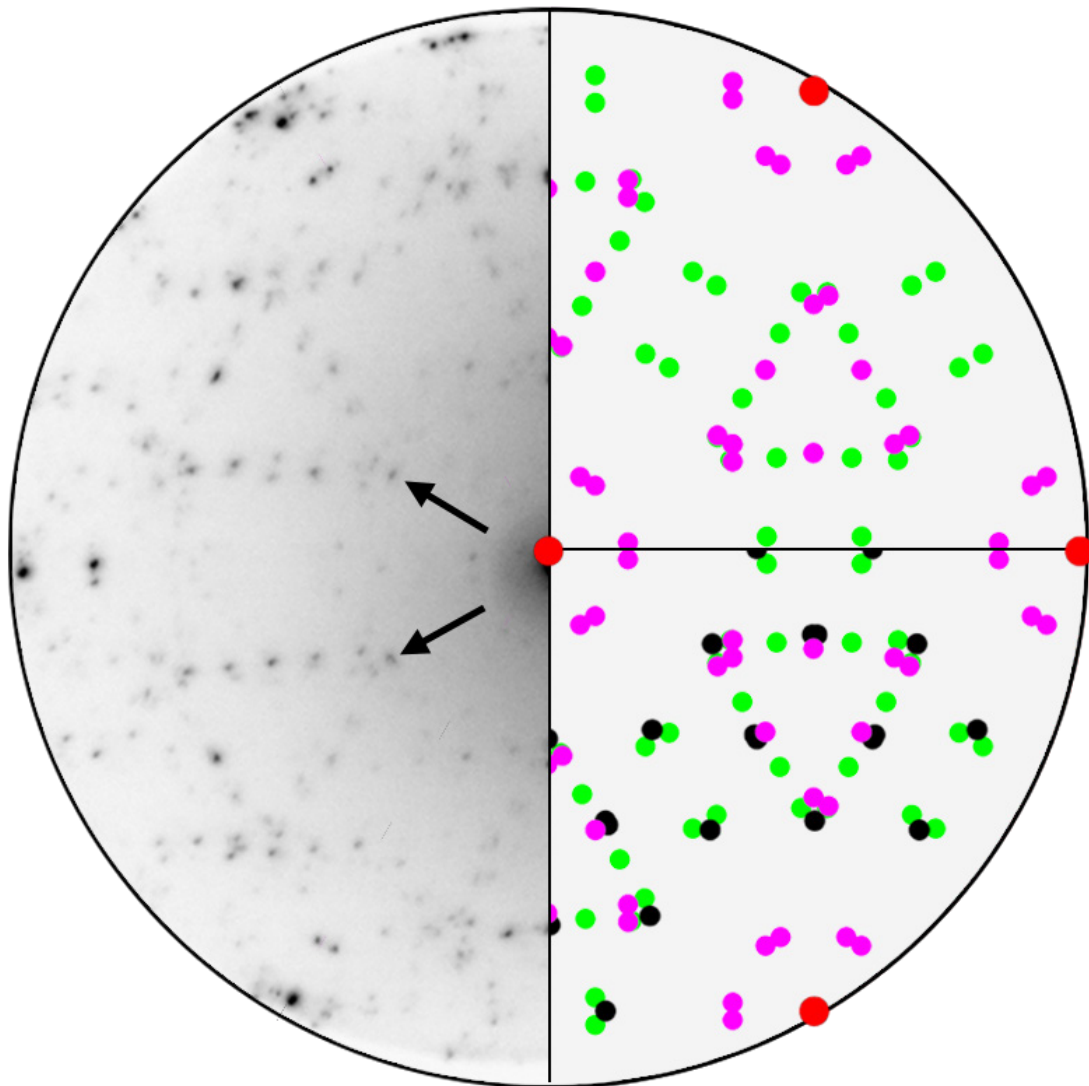


Figure 3.10: μ -diffraction pattern acquired using LEEM. Left half: μ -diffraction pattern, obtained for an electron energy of 50 eV, of 1 ML of silicon deposited on Au(111) kept at 260 °C; upper-right quarter: diffraction model which includes the **b** (green) and **c** (purple) silicide phases shown in Fig. 3.11. The arrows indicate high intensity diffraction spots unexplained by this model; lower-right quarter: the diffraction model of the upper-right quarter is extended including a silicene-derived phase, rotated by 30° with respect to Au(111).

Soon after the end of the evaporation, the sample is analysed with LEEM. The acquired μ -diffraction pattern, obtained for an electron energy of 50 eV, is shown in the left half of Fig. 3.10. The diffraction signal is clearly very complex and it is complicated to explain it in a single or double-phase scenario.

It is well known that surface gold-silicides can form under UHV conditions, complicating the observable diffraction pattern.

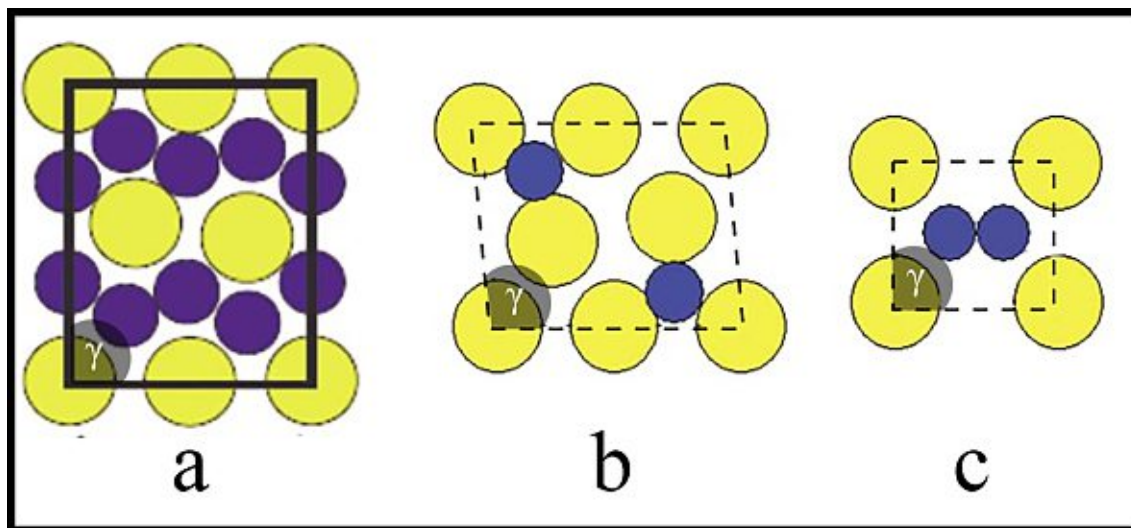


Figure 3.11: Taken from Ref. [89]. Silicides unit cells: a) Au_4Si_8 , $a=7.386 \text{ \AA}$, $b=9.386 \text{ \AA}$, $\gamma=90^\circ$; b) Au_4Si_2 , $a=5.41 \text{ \AA}$, $b=4.25 \text{ \AA}$, $\gamma=95.5^\circ$; c) AuSi_2 , $a=3.66 \text{ \AA}$, $b=2.94 \text{ \AA}$, $\gamma=91.1^\circ$.

Three different surface gold-silicides have been recognised and their unit cells have been recently precisely analysed by grazing-incidence X-ray diffraction [89, 90]. These structures were identified by studying the properties of the eutectic liquid $\text{Au}_{82}\text{Si}_{18}$, when heated above the eutectic point. The reconstructed unit cells, with their dimensions, are shown in Fig. 3.11. Only the first of the three phases is characterised by an orthorhombic unit cell, while the others having a lower symmetry, with a γ angle $\neq 90^\circ$.

The observed diffraction signal of Fig.3.10 is compared with diffraction models obtained by using the software LeedLAB [49] which assume the presence of the silicides described in Fig. 3.11. In the upper-right quarter of 3.10, the signal is compared with a diffraction model composed by the AuSi_2 silicide phase (purple), with a rotation of 30° with respect to the Au(111) substrate and the Au_4Si_2 silicide phase (green), with a rotation of 22° with respect to the Au(111). The model also includes multiple-scattering events with the substrate. Evidently, good agreement can be obtained.

In this comparison, the third silicide phase, Au_4Si_8 , was not included as its diffraction pattern is clearly not observed here. All the phases are observed down to the smallest analysable area with LEEM of 185 nm, suggesting that the different phases are growing forming extremely small domains and with no preferential location.

This comparison proves that the substrate is partially covered by Au-silicide surface phases. This is somewhat surprising as the eutectic point is never surpassed during the experiments here reported, with the growth temperature being more than $100 \text{ }^\circ\text{C}$ lower.

Nevertheless, silicide phases are appearing, as clearly proven by the LEED patterns, probably due to the special conditions of the experiment described here where a very low Si flux is directed towards a perfectly clean Au(111) surface.

At the same time, however, it is clear that some bright diffraction spots are left unexplained, as indicated by the arrows in Fig. 3.10, suggesting the presence of an additional phase. The 12×12 silicene reconstruction, proposed in Ref.[88], does not fit the observed diffraction pattern. Recently, the existence of a hexagonal Si phase with an increased lattice parameter of $\approx 4.1 \text{ \AA}$ has been observed forming on Au(111) [87] under similar growth conditions. Such a strained condition is surprising but a good lattice matching condition can be observed between this strained silicene phase and Au(111), if the 2D layer is rotated by 30° with respect to the substrate. This suggests that, on the surface of Au(111), a silicene phase could be induced to assume a strained configuration for energy optimisation reasons. Moreover, simulations have predicted that silicene is stable up to a huge biaxial tensile strain of 17 % [91].

In the lower-right panel of Fig. 3.10, a strained silicene phase is added (black dots), fitting well the unexplained diffraction peaks. The structure of this layer, however, could not be determined only from the diffraction images, as the observed signal is complicated by the presence of different phases and by the presence of diffraction spots related to multiple scattering processes. These diffraction data were integrated with additional experimental information, in order to propose a valid structure. The ideal tool for the determination of the structural properties of a 2D material is certainly given by polarised Raman spectroscopy, as evidenced in the previous chapter.

3.2.2 Vibrational Properties

As evidenced previously, polarised Raman spectroscopy is able to provide a precise picture of the symmetry properties of the analysed structure. This, in combination with the diffraction data presented in the previous section, will result in a powerful set of data for the determination of the structure of the analysed material. Most importantly, Raman signal coming from a silicene phase will not be hindered by the presence of silicides, differently from what happens for diffraction measurements. This can be expected for the following reasons: firstly, bulk gold silicide has been reported to be Raman inactive [92]. Additionally, surface gold silicides, which could possess Raman active modes due to a modified structure compared to the bulk, are expected to behave differently compared to a silicene phase. These surface silicide phases are described by unit cells with a very low symmetry, as shown in Fig. 3.11. Even by assuming that all of their atoms lay in the same plane (zero buckling scenario), the highest symmetry achievable by these structures is described by point group C_2 . The Raman tensors of this group are:

$$A(z) : \begin{pmatrix} a & d & 0 \\ d & b & 0 \\ 0 & 0 & c \end{pmatrix}, B(x, y) : \begin{pmatrix} 0 & 0 & e \\ 0 & 0 & f \\ e & f & 0 \end{pmatrix}$$

This means that these phases cannot show fully polarised Raman modes, differently from what happens for higher symmetry phases, as observed previously for silicene on Ag(111) [85]. For these reasons, polarised measurements will be crucial for a correct interpretation of the Raman spectrum. Once again, in order to perform *ex situ* μ -Raman measurements, the Si monolayer must be protected from oxidation. To do so, the same encapsulation process used for silicene on Ag(111) is employed here. In this case, however, few-layers hBN are used as encapsulation material, as its transparency allows to acquire Raman spectra with a higher signal to noise ratio. The spectrum of silicene on Au(111) encapsulated under few-layers hBN flakes is shown in Fig. 3.12 a. Alongside the well-known E_{2g} mode of multilayer hBN, centred at $\approx 1360 \text{ cm}^{-1}$, other three peaks can be observed, located at 83 cm^{-1} , 100 cm^{-1} and 435 cm^{-1} .

Notably, no 520 cm^{-1} peak can be detected, indicating the absence of crystalline, sp^3 hybridised silicon on the surface. As mentioned before, the analysis of the polarisation dependency of the detected peaks is important for a correct interpretation of the results. The spectrum acquired in parallel polarisation, indicated by the red solid curve in panels b and c, shows again the peaks centred at 83 cm^{-1} , 100 cm^{-1} and 435 cm^{-1} .

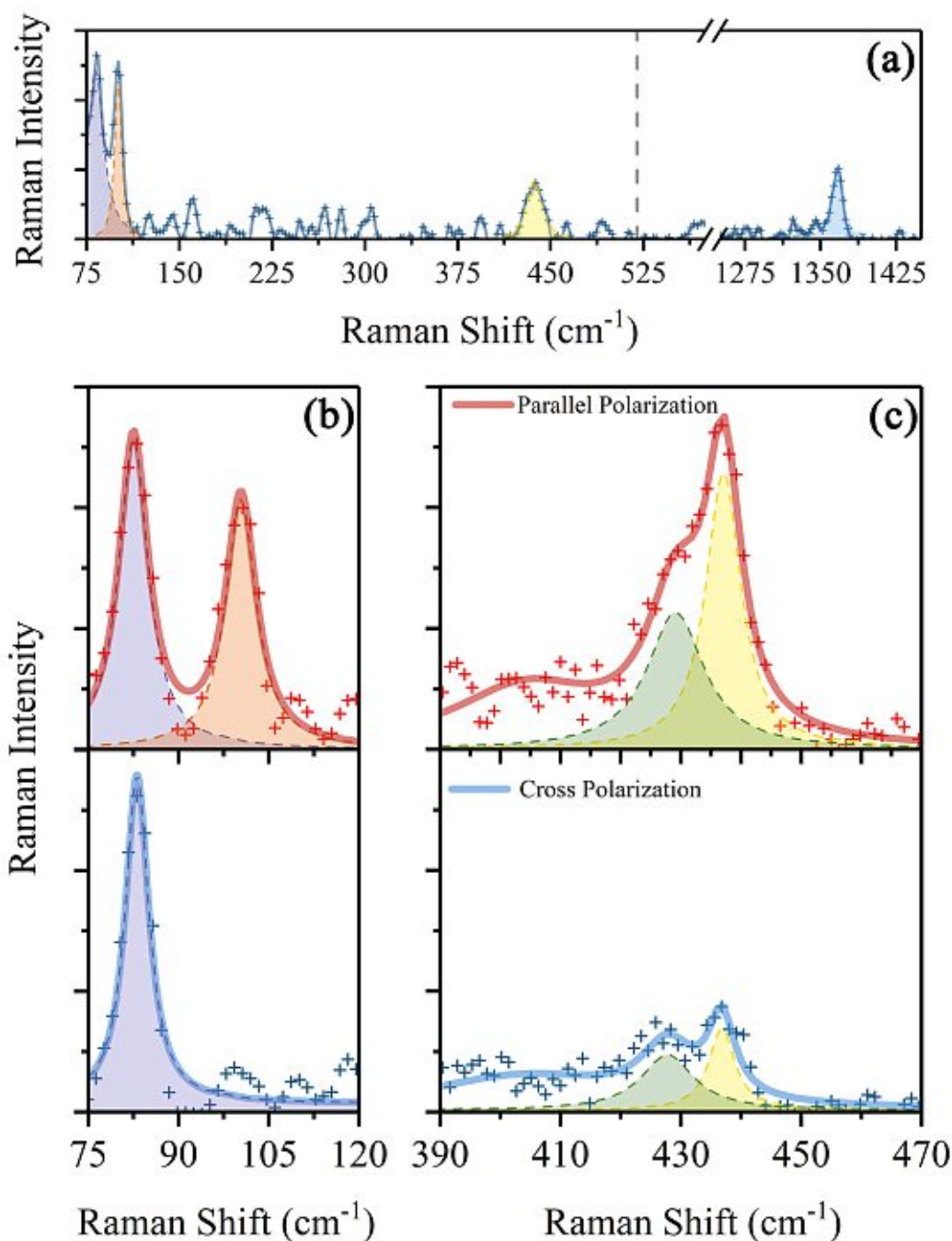


Figure 3.12: a) Unpolarised Raman spectrum of 1 ML silicene on Au(111). The dashed line indicates the position of the Raman mode of sp^3 hybridised Si (520 cm^{-1}). b), c) Polarised Raman spectra, acquired in backscattering geometry, in parallel (top, red line) and cross polarisation (bottom, blue line) configurations. Low frequency modes can be fitted by a single Lorentz function (purple and orange dashed lines), while the high frequency peak is fitted with a combination of two Lorentz functions (green and yellow dashed lines). The two panels (b,c) are separated because the spectra are acquired with different spectrometers.

Interestingly, in cross polarisation configuration (blue solid lines), the 100.4 cm^{-1} peak is completely suppressed and the 429 and 437.0 cm^{-1} ones have a strongly reduced intensity. Clearly, the 100.4 cm^{-1} peak cannot be related to the silicide phases, as no fully polarised mode is expected for those structures.

This evidence clearly indicates that an additional phase, with a higher symmetry than the silicide phases, must have grown onto the Au(111) surface.

While the low frequency peaks can be fitted well with a single Lorentzian functions (purple and orange dashed lines), the higher frequency peak is obviously composed by two different modes and can be fitted by a combination of two Lorentzian functions (green and yellow dashed lines). The fitting results are reported in Table 3.3.

Peak Centre (cm^{-1})	Peak FWHM (cm^{-1})
82.8 ± 0.2	5.0 ± 0.5
100.4 ± 0.2	6.5 ± 0.5
429 ± 2	11 ± 4
437.0 ± 0.5	7 ± 2

Table 3.3: Position and FWHM of Raman peaks observed for 1 ML silicene on Au(111).

The observed Raman modes are strongly redshifted if compared to the ones calculated for freestanding silicene, where the out-of-plane vibrational mode is expected at $\sim 175 \text{ cm}^{-1}$ and the in-plane vibrational modes (doubly degenerate) are located at $\sim 566 \text{ cm}^{-1}$ [22]. The peaks are also redshifted if compared to the one observed for silicene on Ag(111) which, as described before, are located at 216 cm^{-1} for the out-of-plane vibrational mode and at 515 cm^{-1} for the in-plane vibrational modes. A softening (or redshifting) of a Raman mode can be generally related to an elongation of the bond length [93]. This is in good agreement with the hypothesis that, on Au(111), a strained silicene phase can favour lattice matching, thus lowering the formation energy. To understand if the observed Raman signature can truly be assigned to a strained silicene phase, it is compared with the results of first-principles calculations. Density-functional calculations are performed with the ABINIT code [94] to compute the phonon modes at the Γ point and the corresponding Raman susceptibility tensors [95, 96]. The calculations are performed using norm-conserving pseudopotentials, a plane-wave cutoff of 48 Ha, the local density approximation for the exchange-correlation energy, and a 22×22 k-point grid to sample the Brillouin zone. At first, a free-standing layer of silicene is simulated, obtaining, as expected, a lattice parameter of 3.810 \AA , a buckling of 0.425 \AA and Γ -point phonons of 175 cm^{-1} and 566 cm^{-1} . Next, the atomic positions are optimised, constraining the lattice parameter of silicene to the value of 4.1 \AA , corresponding to a biaxial tensile strain of 7.6%, in accordance with the previous report [87] and with the lattice matching condition in case of a 30° rotation with respect to the substrate. In this highly strained condition, the buckling is reduced to 0.237 \AA .

The computed Raman spectra for a 7.6% biaxially strained silicene phase, in both the parallel and crossed polarisation geometry, are shown in Fig. 3.13 a,b as dashed black lines. The simulated structure that gives rise to these spectra is shown in Fig. 3.13 c and is described by considering a rhomboidal unit cell with an edge length of 4.1 \AA

and $\gamma = 60^\circ$. The calculated Raman spectrum is characterised by two peaks: the one related to out-of-plane vibrations is located at 98.6 cm^{-1} and is totally suppressed in cross polarisation configuration; the two modes (degenerate) related to the in-plane vibrations are both located at 447.3 cm^{-1} and show no polarisation dependency.

The position of the simulated peaks is very similar to the experimental observations, suggesting a close match between the structures. The intensity of the simulated low-frequency peak is, however, $\approx 3000\times$ lower than what can be experimentally observed. A possible explanation for this difference could be related to the presence of the substrate, not accounted for in the theoretical calculations. Au(111)/mica is a SERS active substrate [97] and it is well-known that the amplification factors are extremely high and can noticeably vary for different vibrational modes [98]. Such an amplification is expected to be particularly effective for an out-of-plane vibration, which could couple well with the metallic substrate. The peak at 82.8 cm^{-1} is clearly not showing up in the computed spectra and could be related to defects- or edge-activated Raman modes, that are not taken into account within the simulation. Additionally, in the experimental spectrum, the in-plane vibrational modes are clearly splitted and their polarisation dependency is different from the calculation results. The loss of degeneracy of the in-plane vibrational modes is reminiscent of what can be observed for graphene when uniaxial strain is applied [99].

For this reason, simulations have been repeated by considering a slightly deformed hexagonal structure resulting from the application of a small uniaxial strain (1%) along the zig-zag direction. The obtained Raman spectrum is shown in Fig. 3.13 as solid coloured lines. Notably, as a consequence of the additional uniaxial deformation, the out-of-plane vibrational mode gets a small blueshift, moving up to 102.9 cm^{-1} . At the same time the in-plane vibrational modes get redshifted and split up in two distinct peaks, as the degeneracy is lifted, at 433.9 cm^{-1} and 439.5 cm^{-1} . Additionally, the polarisation dependency is completely changed, with the in-plane modes getting now only partially suppressed. Overall, these new results are much closer to the experimental results, making it possible to reliably assign the observed Raman spectrum to a highly strained silicene phase. The deformed hexagonal lattice can be described by considering a rectangular unit cell with dimensions of $4.141 \times 7.1 \text{ \AA}^2$, as shown in Fig. 3.13 d. The diffraction pattern generated by this structure, assuming a rotation of 30° with respect to the Au(111), is shown in the lower-right quarter of Fig. 3.10 by the black dots and agrees well with the intense spots that were left unexplained by the silicides-only model.

Overall, the observed data point to the presence of a highly biaxially strained silicene phase, with a slight deformation along the zig-zag direction. This asymmetry does not come as a surprise, as the surface layer of Au(111) is compressed along the $\langle 110 \rangle$ direction, where 23 atoms on the surface are fitted in the same space occupied by 22 atoms in the bulk. The peculiar surface reconstruction of Au(111) [100] thus could be the reason for the uniaxial deformation of the silicene phase.

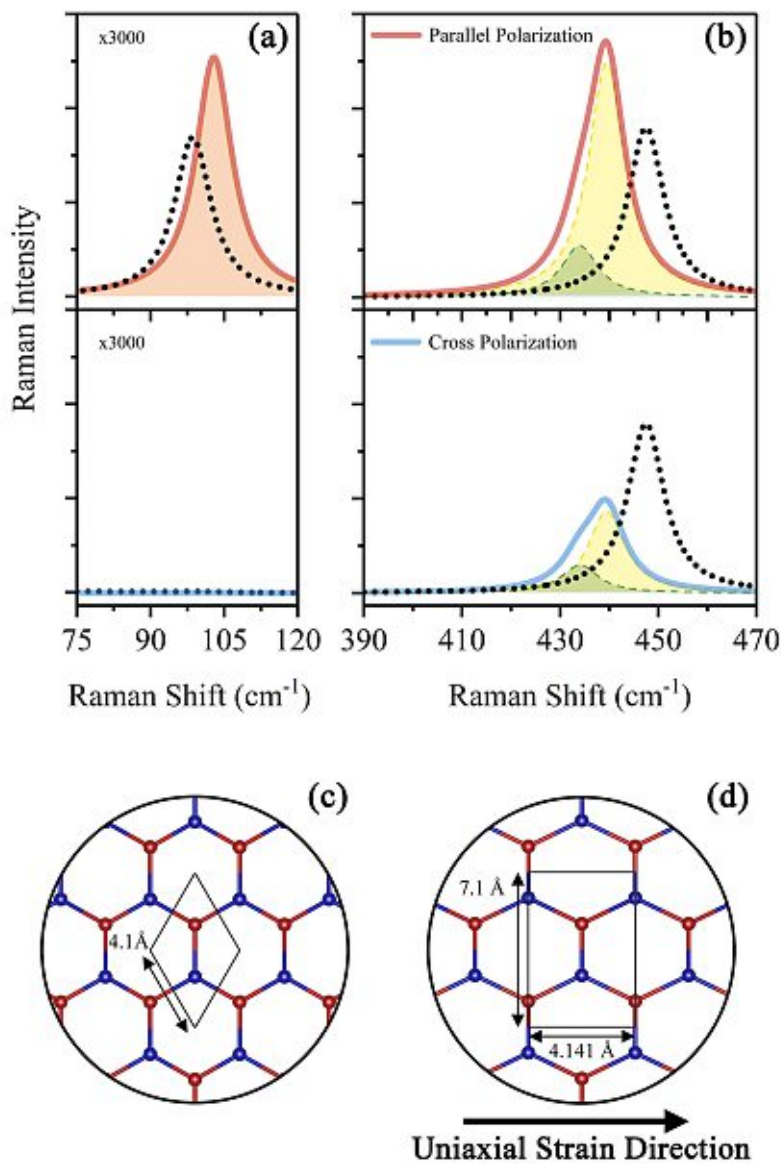


Figure 3.13: a-b) Simulated Raman spectra in parallel and cross polarisation configurations for 7.6% biaxially strained silicene with lattice constant of 4.1 Å (dotted black lines) and for the same phase with an additional uniaxial 1% deformation along the zig-zag direction (red and blue solid lines). The intensity of the low-frequency peak is enhanced by $\approx 3000\times$. c-d) Representation of the simulated silicene structures. The unit cells are indicated with a solid black line. For clarity reasons, the image in (d) describes a larger additional strain (20%), while the unit cell sizes are related to the 1% strain configuration.

3.2.3 Photoemission Spectroscopy Measurements

X-ray Photoemission Spectroscopy

To complete the characterisation of silicene on Au(111) photoemission spectroscopy measurements are performed. XPS was used to probe the Si2p orbital. Differently from Ag(111), where the signal from the Ag4s orbital was interfering, in this case only the signal of silicon is detected in the selected energy region.

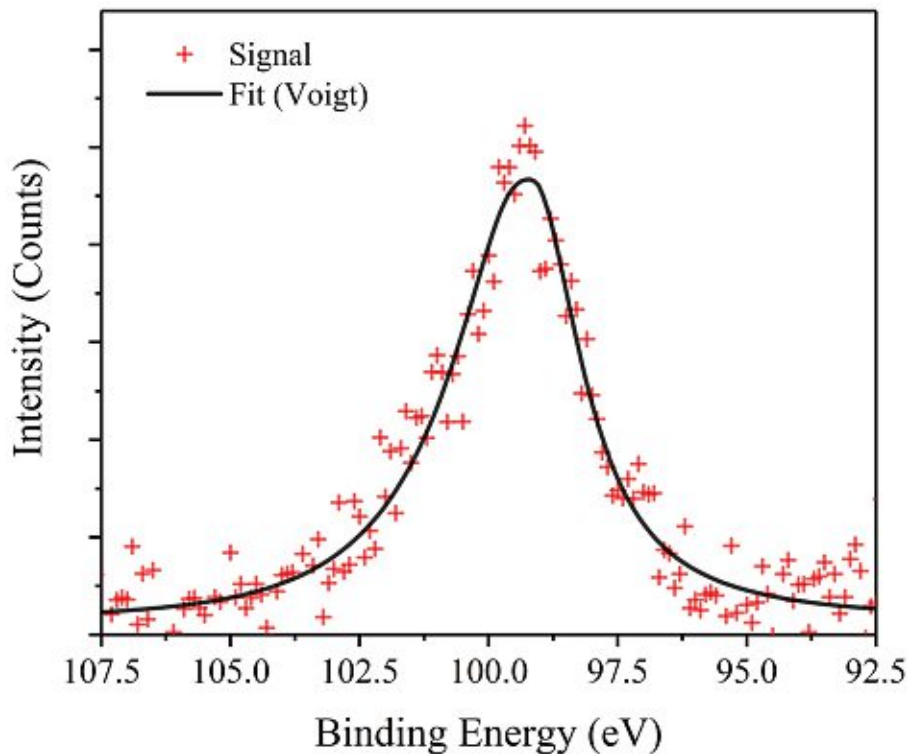


Figure 3.14: XPS signal probing the Si2p peak for 1 ML silicene on Au(111). The signal is acquired with a takeoff angle of 60° . The peak is fitted with an asymmetric Voigt profile.

The plot in Fig. 3.14, shows the presence of a well-defined peak with a longer tail on the left. For this reason the peak is better fitted with an asymmetric Voigt function, after performing a Tougaard background removal step [77]. The results of the fitting are reported in Table 3.4.

Si2p Peak	Values (eV)
Center	99.15 ± 0.05
FWHM	2.4 ± 0.2

Table 3.4: Position and FWHM of the Si2p peak for 1 ML silicene on Au(111).

Once again, the observed peak is slightly shifted to lower binding energies, if compared to the position of the Si2p peak in intrinsic bulk silicon (99.4 eV [76]). However, the shift

is less pronounced than in the case of silicene/Ag(111), probably due to the presence of surface silicides, which lead to a surface only partially covered by sp^2 hybridised silicon. The slightly asymmetric shape, with a longer tail towards higher binding energies, could be related to the sp^2 hybridised state of the silicon atoms. A similar behaviour has been observed also for the C1s peak of HOPG, and has been related to the high asymmetry of the peak related to sp^2 hybridised carbon [101]. In the case of silicene/Ag(111), a full understanding of the peak shape was hindered by the overlapping Ag4s signal.

Angle Resolved UV Photoemission Spectroscopy

ARUPS scans are performed along the $\Gamma \rightarrow K$ and $\Gamma \rightarrow M$ directions of the 2D Au Brillouin zone - *i.e.* the projection of the 3D Au Brillouin zone onto the (111) plane. Once again, the analyses are performed by collecting several images for each rotation step (representing a movement in the k-space) and by stitching them together using the algorithm presented in the Appendix A. Each image is collected using a rectangular slit ($0.2 \times 20 \text{ mm}^2$), an energy resolution of 20 meV, a passing energy of 2 to 10 eV and an exposure of 0.1 s for each energy step. The photoelectrons are excited using He I photons, with an energy of 21.2 eV. The ARUPS spectra for a clean Au(111) substrate and for 1 ML silicene on Au(111) are shown in Fig. 3.15. The upper panels report the signal acquired by scanning along the $\Gamma \rightarrow M$ direction of the Au(111) Brillouin zone. In the first panel, signal from the clean Au(111) substrate is reported. The parabolic sp band is clearly recognisable, crossing the Fermi level at $k_{\parallel} \approx 1 \text{ \AA}^{-1}$. After the deposition of 1 ML of silicon, the scan is repeated and the results are shown in panel b. The Au sp band is still recognisable, but fainter. At the same time, a new band appear at k values higher than 1 \AA^{-1} . Due to the low intensity of the band, a higher passing energy scan is performed, as shown in panel c. The band is seemingly plateauing at $k_{\parallel} \approx 1.25 \text{ \AA}^{-1}$ and at a binding energy level of $E_B \approx 0.5 \text{ eV}$. No clear signal is detected for higher values of k, possibly due to a photoemission interference effect, already observed for graphene, that makes only one branch visible [102]. The signal obtained for a scan along the $\Gamma \rightarrow K$ direction is shown in the lower panels. Once again, the first panel is showing the signal taken from the clean Au(111) substrate, with the sp band still clearly visible. After the deposition of the Si monolayer (panel b'), a new band becomes visible, similarly to what has been observed in panel b. The image of panel b' is composed of two different scans, with the upper part of the image being acquired with a higher passing energy (5 eV) to compensate for the low intensity. Differently from the situation described in the upper panels, the additional band does not seem to reach a plateau. Its intensity becomes fainter as the band approaches the Fermi level.

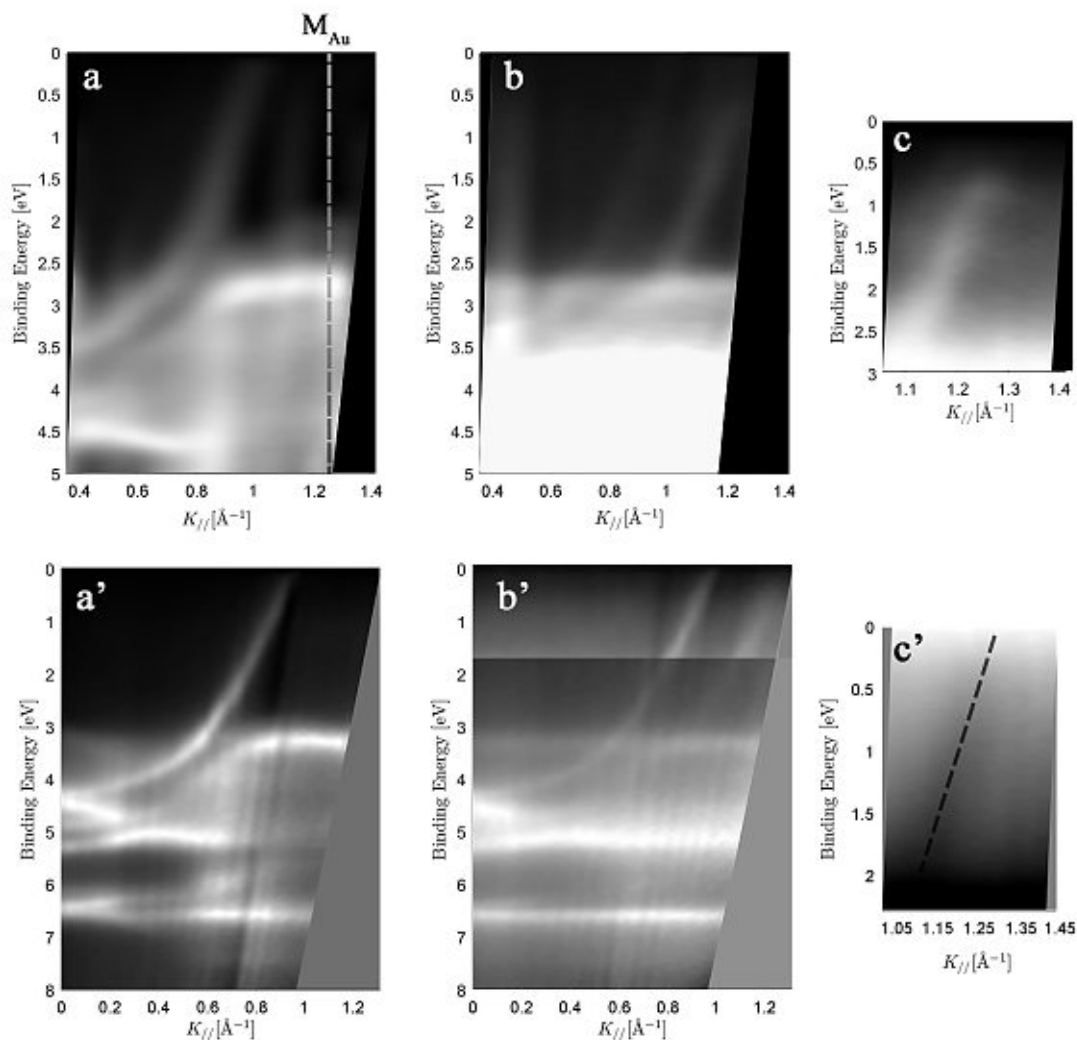


Figure 3.15: a-c) ARUPS signal acquired scanning along the $\Gamma \rightarrow M$ direction of the Au(111) Brillouin zone: a) Signal obtained from the clean Au(111) substrate; b) Signal obtained after deposition of 1 ML Si; c) High passing energy scan (10 eV) of a selected energy region of b); a'-c') ARUPS signal acquired scanning along the $\Gamma \rightarrow K$ direction of the Au(111) Brillouin zone: a') Signal obtained from the clean Au(111) substrate; b') Signal obtained after deposition of 1 ML Si; The upper part of the image has been scanned with a higher passing energy (5 eV) c') High passing energy scan (10 eV) of a selected energy region of b). The dashed line indicates the apparent position of the linear band. The image colours are inverted to enhance the contrast.

A high passing energy scan, shown in panel c', reveals a faint band rising linearly towards the Fermi level. The image is shown in reversed colours to enhance the contrast, as the band is extremely faint. By following the band direction (dashed line), the Fermi level is crossed at $k_{//} \approx 1.3 \text{ \AA}^{-1}$. By measuring the slope of the linear band it is possible to extrapolate the Fermi velocity, as the linear dispersion can be described by

$$E = \hbar V_F k \quad (3.1)$$

The measured Fermi velocity is $V_F = 1.58 \pm 0.01 \cdot 10^6 \text{ m/s}$, a value close to the one measured for graphene [102].

The results shown in Fig. 3.15 are seemingly in contrast with what has been observed in Ref.[88], where the plateauing band is observed along the $\Gamma \rightarrow \text{K}$ direction (and not the $\Gamma \rightarrow \text{M}$ one) and where it is interpreted as a gapped Dirac cone.

The obtained results are strikingly similar to what has been observed for silicene/Ag(111) [80]. In this work, a linear band has been observed for a scan along the $\Gamma \rightarrow \text{K}$ direction, while a plateauing band (and then descending) can be observed in the $\Gamma \rightarrow \text{M}$ direction. Both bands have been recognised as being surface states. The plateau in the M direction has been identified as a saddle point in the band structure. In general, the bands have been interpreted as the result of a hybridisation between the silicon atoms and the silver atoms, resulting in a degradation of the electronic properties of silicene.

An alternative explanation, however, can be proposed in this case. By looking at the terminated Au(111) surface covered by a biaxially strained silicene phase (rotated by 30° with respect to the substrate), as shown in Fig. 3.16, it is possible to recognise a periodic structure given by the matching condition between Si and Au atoms, that shows the same orientation as the Au(111) unit cell. This periodical structure, indicated by the black hexagon, has a lattice parameter $\mathbf{a} = 5 \cdot a_{Au}$. This larger structure could arise on the Au(111) surface due to a more complex arrangement of the Si atoms, with some of them assuming different buckling levels for energy minimisation reasons, similarly to what happens for silicene on Ag(111). The expected position of the M and K point for such a structure would be, respectively, $k_K \approx 0.29 \text{ \AA}^{-1}$ and $k_M \approx 0.25 \text{ \AA}^{-1}$. The plateau observed along the $\Gamma \rightarrow \text{M}$ is positioned at $k_{//} = 5 \cdot k_M \approx 1.25 \text{ \AA}^{-1}$, supporting the existence of a structure with a periodicity of 5. The observed plateau could thus be interpreted as the one expected for a freestanding silicene layer at the M point, as shown in Fig. 1.5. Following this model, the Fermi crossing point along the $\Gamma \rightarrow \text{K}$ direction should be related to the larger periodical structure. However, the position of the observed crossing point is too small to match a $5 \times$ periodicity, as $5 \cdot k_K \approx 1.45 \text{ \AA}^{-1}$, while the band was observed crossing the Fermi level at $k_{//} \approx 1.3 \text{ \AA}^{-1}$. Nevertheless, a strained silicene structure is expected to show a slightly different band structure [91]. In particular, the Dirac cone's tip is expected to shift above the Fermi level, causing the valence band to cross the Fermi level at a smaller $k_{//}$, as observed experimentally. Further experiments in the future are required to clarify the electronic properties of this structure, keeping in mind that the biaxially strained silicene scenario offers some intriguing similarities with what has been observed here experimentally. In particular, it is expected that biaxially strained silicene will give rise to p-doped Dirac states, due to the Dirac cone's vertices moving above the Fermi level [91].

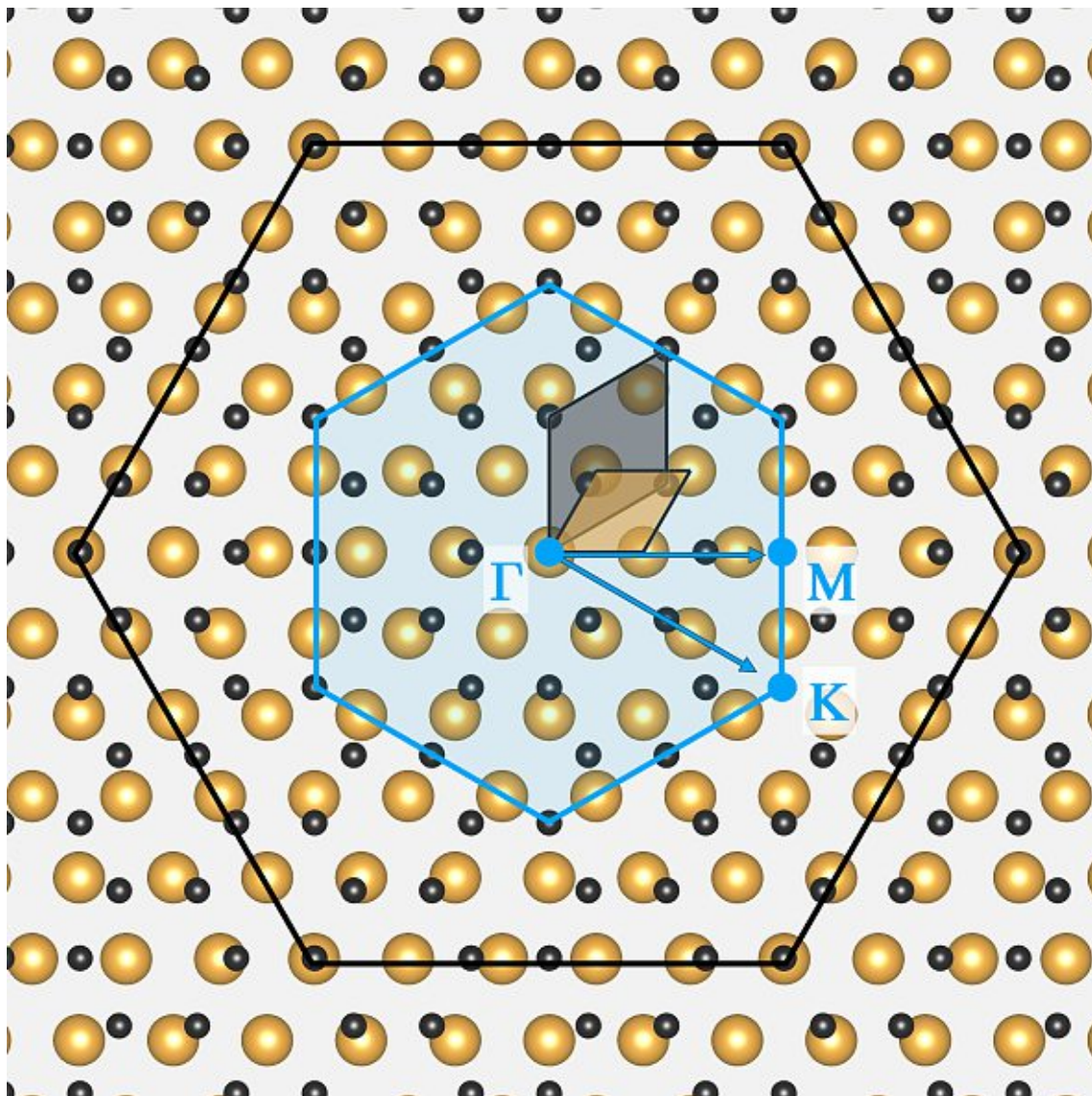


Figure 3.16: An ideally terminated Au(111) surface, covered by a biaxially strained silicene phase (with no uniaxial deformation), rotated by 30° with respect to the substrate. The rhomboidal unit cell of silicene is shown in black, the one of Au(111) in gold. The black hexagon indicates a possible periodical structure, with the same orientation as Au(111). The blue hexagon indicates the orientation of its Brillouin zone.

3.3 Integration of Silicene and Calcium Fluoride

The extreme reactivity of silicene is certainly one of the biggest challenges that need to be overcome to successfully integrate this 2D material in electronic devices. The last chapter of this thesis is focused on the exploration of a suitable material for the realisation of a gate dielectric layer that can be interfaced directly with silicene, without degrading its properties.

Crystalline calcium fluoride (CaF_2) is a formidable insulator, even for extremely thin layers (~ 2 nm), with a wide band gap of 12.1 eV and a high dielectric constant ($\epsilon = 8.43$) [103]. CaF_2 crystallises in the so-called *fluorite structure*, where the Ca ions occupy the regular sites of a face-centered cubic (FCC) structure and the F ions occupy the tetrahedral interstitial sites.

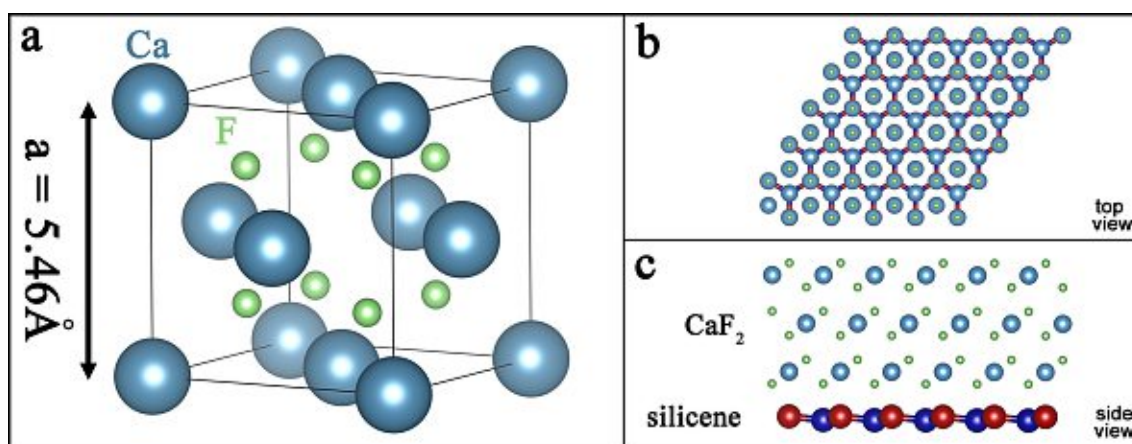


Figure 3.17: a) Schematic representation of CaF_2 crystallising in the fluorite structure. Ca ions (blue) occupy the regular sites of a face centred cubic (FCC) cell, while F ions (green) occupy the tetrahedral interstitial sites. b,c) Side and top views of a possible stacking between 1 ML silicene and CaF_2 , highlighting the perfect lattice matching.

Notably, the lattice parameter of CaF_2 ($a = 5.46 \text{ \AA}$) is very close to the one of Si ($a = 5.43 \text{ \AA}$). For this reason, this material can be epitaxially grown, with high quality, on a silicon (111) substrate [104, 105]. From this naturally follows that the lattice parameter of the (111)-terminated CaF_2 lattice is very close to the one of freestanding silicene (3.87 \AA), as shown in Fig. 3.17. Additionally, the $\text{CaF}_2(111)$ surface is inert and free from dangling bonds, as it is terminated by fluorine atoms [106]. This characteristic is especially important when interfacing 2D materials because, in order to preserve the electronic properties of such a thin layer, no chemical bonding must take place. Recently, ultra thin CaF_2 layers have been successfully used to realise MoS_2 -based field-effect transistors [107], showing their compatibility with 2D materials.

All these characteristics make CaF_2 a promising candidate for the realisation of a high quality silicene-dielectric interface by molecular beam epitaxy, allowing to preserve the properties of the 2D silicon layer.

3.3.1 Epitaxial Growth

Silicene grown on Ag(111) is chosen as a platform to investigate the interface with CaF₂, as its structure is fully characterised, allowing one to precisely understand the impact induced by the coupled CaF₂ layer. As a starting point, 1 ML of silicene is grown on Ag(111) at 260 °C, following the procedure outlined in Sec.3.1.

CaF₂ evaporation is obtained by thermal evaporation of small (2-5 mm) calcium fluoride crystals (Merck). The crystals are loaded into the tungsten crucible of a SPECS EBE-4 e-beam evaporator. In this configuration, an electron beam is directed against the crucible, heating it up but never hitting directly the target material. For this reason, the process can be considered as a pure thermal evaporation. CaF₂ has been reported to grown on Si(111) at very different temperatures, ranging from 200 °C to 800 °C [104]. Some of these temperatures are well beyond the limit of stability for silicene on Ag(111). Notably, by keeping the Si(111) substrate temperature at 250 °C it was possible to grow ultra-thin CaF₂ layers (with a thickness of just 4-5 ML) with a leakage current that was sensibly reduced if compared to the one measured for layers grown at higher temperatures [108]. Such moderate growth temperatures, therefore, allow to synthesise dielectric films with superior properties, while ensuring a good compatibility with the silicene layer grown on Ag(111). The evaporation rate has been calibrated by evaporating CaF₂ for several hours on a reference silicon sample at a fixed flux of 10 nA (emission current = 0.42 mA, filament current = 3.3 A, voltage = 1.7 kV) and, subsequently, measuring the thickness of the evaporated layer using a spectroscopic ellipsometer. By using these evaporation parameters it was possible to reach an evaporation rate of $\sim 1.2 \frac{nm}{h}$ or, equivalently, $\sim 2 \frac{ML}{h}$. To ensure that no impurities are formed at the interface, the time between the end of silicene growth and the beginning of the CaF₂ evaporation is kept as short as possible. While increasing the temperature on the CaF₂ crucible, the silicene sample is stored in a separated chamber of the UHV system, to protect it from the contamination with degassing species that may have accumulated into the CaF₂ crucible between experiments. The growth is performed by first heating the silicene/Ag(111) sample up to the required temperature of 250 °C and then by opening the shutter of the CaF₂ evaporation pocket, once that the growing temperature has been maintained at the target level for at least 15 minutes.

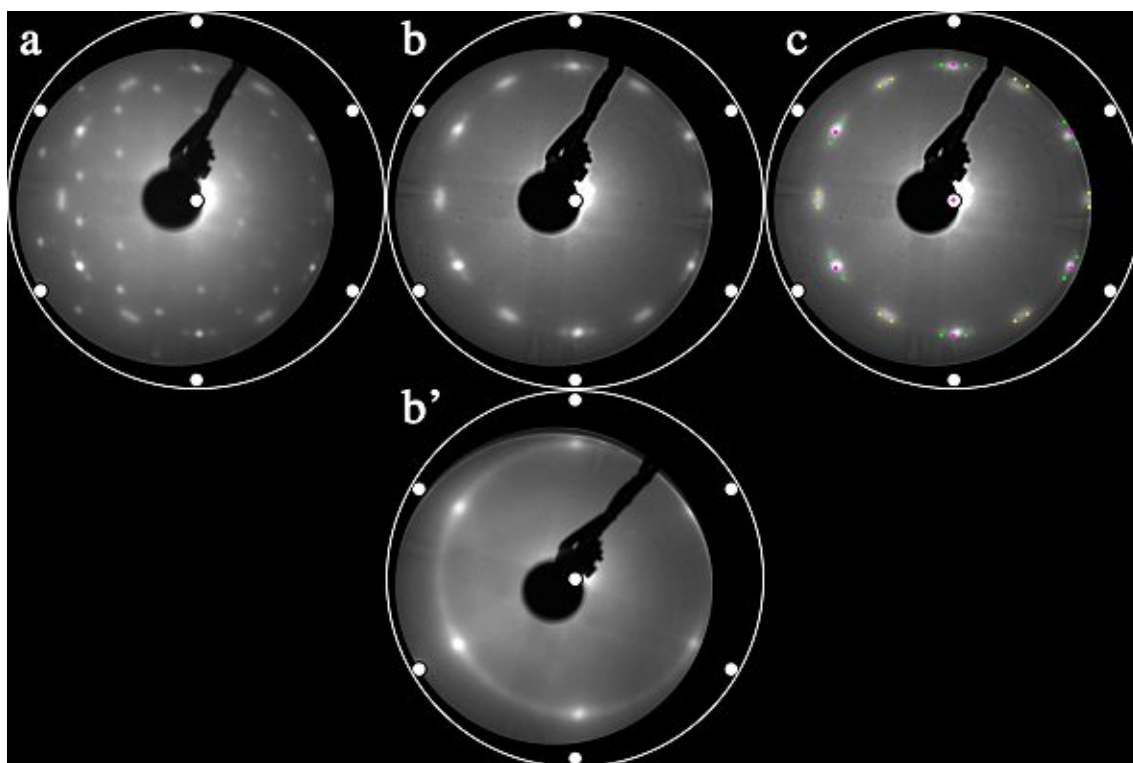


Figure 3.18: LEED diffraction patterns acquired at an electron energy of 35 eV for: a) 1 ML silicene on Ag(111) grown at 260 °C; b) ~ 5 ML CaF_2 grown on top of silicene at 250 °C; b') ~ 5 ML CaF_2 grown directly on Ag(111) at 250 °C; c) Diffraction model obtained for CaF_2 domains with different rotations superimposed to the signal shown in b); For all the images, the 6 Ag(111) primary diffraction spots are aligned under the white disks.

Fig. 3.18 shows the diffraction patterns obtained with LEED at an electron energy of 35 eV. Panel a shows the typical diffraction pattern obtained for 1 ML silicene grown on Ag(111) at 260 °C, already shown in Section 3.1. After growing ~ 5 ML CaF_2 on top of silicene, the diffraction pattern drastically changes, as shown in panel b. 12 peaks can be observed, 6 of them in correspondence with the position of Ag(111) diffraction peaks (indicated by white disks), 6 with a rotation of 30° . The distance of the obtained spots from the centre is compatible with a lattice constant of 5.46 \AA , as expected for CaF_2 (accounting for the (111) orientation). A great difference in the diffraction pattern can be observed when growing 5 ML CaF_2 directly on Ag(111), without having the single layer silicene below, as shown in panel b'. In this case, it is possible to observe a clear diffraction ring, with pronounced peaks appearing along the main directions of Ag(111). The radius of the ring is also compatible with the lattice constant of CaF_2 . Clearly, without silicene on Ag(111), no epitaxial growth can be started, resulting in a layer constituted partially by randomly oriented domains and partially by domains oriented along the main directions of Ag(111). This result is to be expected as no lattice matching condition exists between CaF_2 and Ag. At the same time, it clearly shows that the silicene monolayer is able to direct the growth of the CaF_2 . This result could be promoted by a non-negligible interaction between the two materials, contrasting the idea of weak interactions due to the absence of dangling bonds in the CaF_2 layer. However, as the lattice mismatch is almost

zero, a good epitaxial growth can be expected also in the case of only weak Van der Waals interactions [109]. The diffraction pattern obtained by growing CaF_2 on silicene can be well modelled by assuming to have domains with 5 different orientations, with rotations of 0° , $\pm 33^\circ$ and $\pm 5.2^\circ$ with respect to the $\text{Ag}(111)$ layer. Interestingly, this is precisely the same configuration observed for a second layer of silicene, as shown in Section 3.1. This surprising result could be a consequence of the similar dimensions of the Si and CaF_2 lattices. Thus, additional layers of either Si or CaF_2 grow following the same orientations likely for energy minimisation reasons.

This is a further strong indication that the material grows with a precise epitaxial relation to the silicene layer, as the growth takes place both on the 4×4 phase, as well as on the $\sqrt{13} \times \sqrt{13} R13.9^\circ$ one. The LEED images presented in Fig. 3.18 are clearly indicating that CaF_2 grows well on silicene, covering completely the layer. However, it is difficult to understand if the silicon atoms are still in a sp^2 -hybridised configuration and if the structure of the silicene layer is left unchanged, due to the low intensity of the silicene diffraction signal and to the overlapping between silicene and CaF_2 related diffraction spots. For a better understanding of the bonding state of the silicon atoms and of the structure of the buried silicene layer a combination of XPS and Raman measurements is used.

3.3.2 Photoemission Spectroscopy Measurements

X-Ray photoemission spectroscopy is employed to analyse the silicene layer before and after the deposition of CaF_2 . For these experiments, a thinner layer of only 2 ML CaF_2 is grown on top of silicene, in order to be able to better detect the Si related signal.

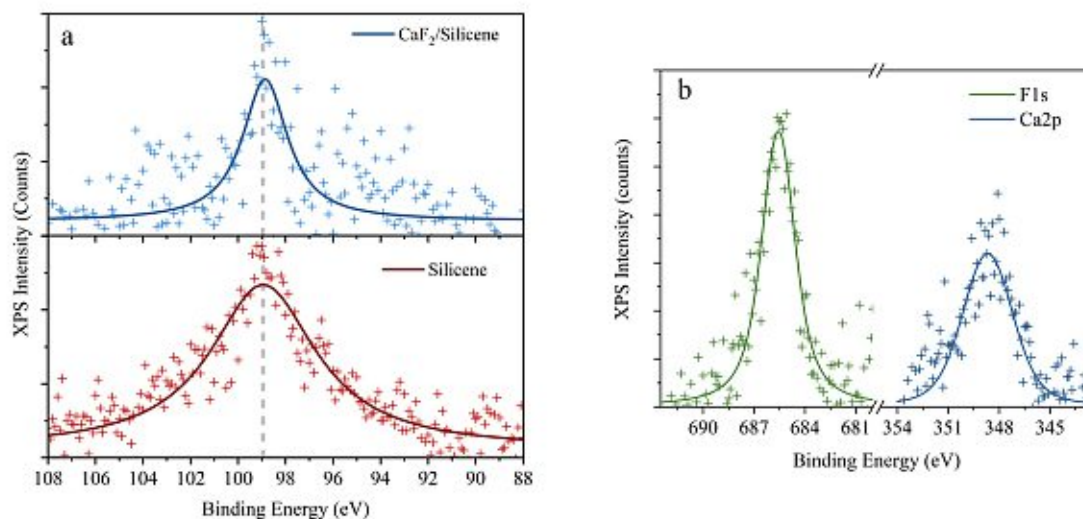


Figure 3.19: a) XPS signal for the Si2p peak acquired before (red) and after (blue) the growth of 2 ML CaF_2 on silicene. The dashed line indicates the position of the Si2p peak for silicene (98.95 eV). b) XPS signal for the F1s (green) and Ca2p (blue) peaks obtained after the deposition of 2 ML CaF_2 on silicene.

The XPS spectra shown in Fig. 3.19 a are acquired with a takeoff angle of 60° , in order to minimise the signal from the Ag substrate, which could interfere into the determination of the exact position of the Si2p peak.

The observed peaks are fitted, once again, using a Tougaard background model and a Voigt profile. The fitting results are reported in Table 3.5.

Si2p Peak	Peak Position (eV)	FWHM (eV)
Silicene	98.95 ± 0.05	5.4 ± 0.2
CaF ₂ /Silicene	98.86 ± 0.04	2.3 ± 0.1

Table 3.5: Position and FWHM of the Si2p peak for 1 ML silicene on Ag(111) and 2 ML CaF₂/1 ML silicene on Ag(111).

Upon deposition of 2 ML of CaF₂, the position of the Si2p peak is slightly shifted by ~ 0.09 eV. Such a small shift is not compatible with the formation of either Ca-Si or F-Si bonds: the former are expected to shift the Si2p peak by 0.4 eV to lower binding energies, while the latter are expected to shift the peak by 0.8 eV to higher binding energies. Both Ca-Si and F-Si related peaks have been observed when growing CaF₂ on Si(111) at a temperature of 750°C [110], alongside the unchanged Si2p peak coming from the unreacted bulk substrate. If such bonds would form in the present case, the shift would be evident as the silicene layer is composed of only a single layer of Si atoms. Therefore, based on the XPS results, it is safe to assume that the silicon atoms of the silicene layer are not reacting with Ca or F atoms at the interface. The small shift towards lower binding energies could be caused by a charge transfer from the Ca atoms to silicon. A similar effect has been observed also in the case of an Al layer deposited on silicene [78], albeit with a two times greater shift. An XPS scan of the F1s and Ca2p peaks is shown in Fig. 3.19 b. A measurement of the stoichiometry of the CaF₂ can thus be obtained by calculating the ratio between the intensities of the two peaks, calibrated with respect to their photoionization cross sections (σ) [111]:

$$\frac{N_F}{N_{Ca}} = \frac{I_F^*}{I_{Ca}^*} = \frac{I_F}{I_{Ca}} \cdot \frac{\sigma_{Ca}}{\sigma_F} = \frac{1146 \text{ cts}}{6 \cdot 10^{-2} \text{ Mb}} \cdot \frac{6.8 \cdot 10^{-2} \text{ Mb}}{637.5 \text{ cts}} \approx 2$$

As expected, the fluorine atoms are approximately two times more frequent than Ca atoms, confirming the quality of the grown layer. XPS spectra are clearly showing that no bonding takes place between the Si atoms of the silicene layer and Ca and F atoms. Additionally, even after the deposition of CaF₂, the position of the Si2p peak remains ≈ 0.5 eV shifted towards lower binding energies if compared to the position of the peak for bulk, sp³-hybridised silicon, suggesting that the silicon atoms are still in a two-dimensional configuration.

Additionally, an UPS experiment has been performed to probe the density of states below the Fermi level after the deposition of the CaF₂ layer. ARUPS in this case is not useful as the band structure of CaF₂ is expected to be rather flat and no useful information can be extracted from an energy/momentum plot. UPS is performed by using, once again, He I photons as the excitation source.

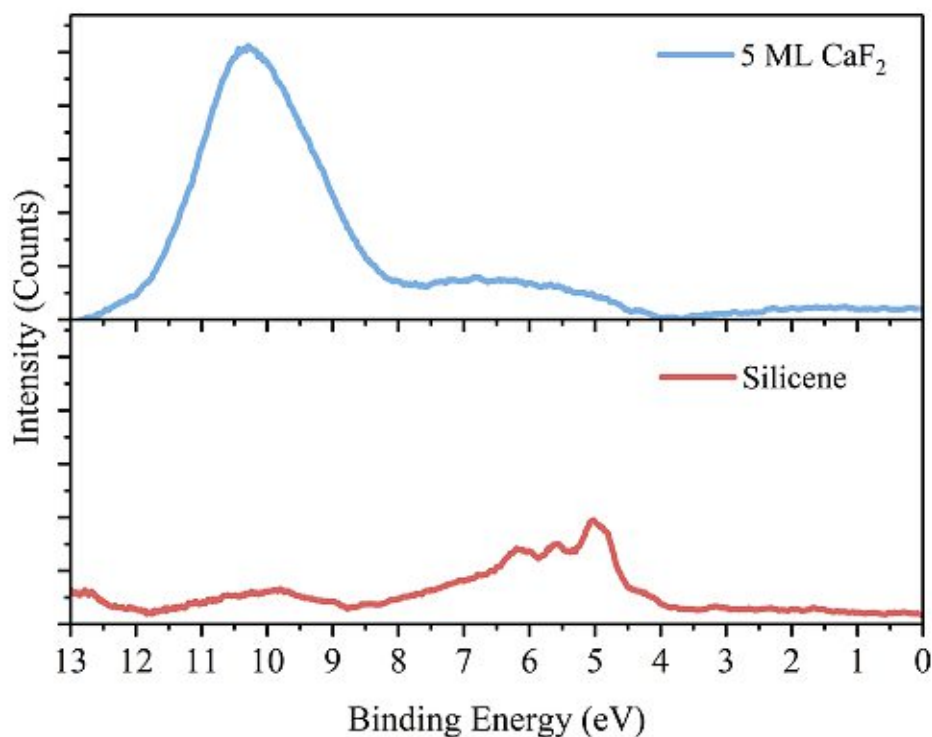


Figure 3.20: UPS spectra acquired using HeI photons as excitation source (21.2 eV). Below, red: Ag(111) substrate covered by 1 ML silicene. Above, blue: 5 ML CaF₂ deposited on 1 ML silicene/Ag(111).

Fig. 3.20 shows the UPS spectra collected for 1 ML silicene on Ag(111) (lower panel, red). In this plot the features visible in the 4-7 eV energy range are related to the low binding energy states of Ag(111), commonly observed when performing UPS [112]. When 5 ML CaF₂ are grown on top of silicene, a pronounced peak can be observed appearing in the energy region between 8 and 12 eV, associated to the F2p valence band of CaF₂, previously reported in literature [113, 114]. Interestingly, it has been observed that the F2p peak splits at a coverage higher than 2 ML [113]. This has been associated to the transition from 2D to 3D CaF₂ growth. This splitting cannot be observed here. The reason is unknown, however it could be related to the rather lower growth temperature of this sample, compared to the previous UPS studies. Nevertheless, the UPS spectrum clearly shows that no impurity states can be detected in the region between the F2p peak and the Fermi level. The visible bump in front of the F2p peak is related to the signal coming from the Ag(111) substrate, still detectable through the thin layer. This result is a good first indication that the CaF₂ grown on silicene will be able to retain its insulating properties. Future studies will have to focus on the determination of the insulation properties of the grown layer.

3.3.3 Vibrational Properties

In order to be able to perform Raman spectroscopy, the buried silicene layer needs to be protected from oxidation. Ultra-thin CaF_2 layers cannot act as a protective layer, as oxygen and water can diffuse through it [107]. Additionally, the encapsulation procedure used for silicene on $\text{Ag}(111)$ and $\text{Au}(111)$ cannot be followed here, as the oxidative species would be still able to diffuse through the CaF_2 layer around the few-layers graphene or hBN flake. By depositing a CaF_2 layer of sufficient thickness it is possible to increase the lifespan of the silicene layer even under ambient condition, as the diffusion time is increased. Therefore, a thicker layer of ~ 11 nm (20 ML) CaF_2 is deposited on top of silicene, using the same process outlined earlier, at the same substrate temperature. The interface properties may be expected to be the same as the ones obtained for 2/5 ML thick CaF_2 layers, as only the growth time is extended.

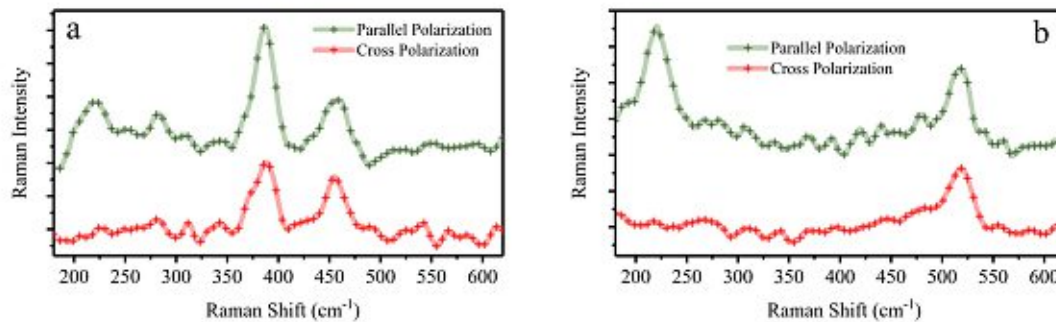


Figure 3.21: Raman spectrum, acquired in backscattering geometry, of: a) 1 ML silicene grown on $\text{Ag}(111)$ covered by a CaF_2 layer with a thickness of ~ 11 nm. b) 1 ML silicene grown on $\text{Ag}(111)$. In both cases, the spectra are acquired in parallel (green) and crossed (red) polarisation configurations.

The Raman spectrum, shown in Fig. 3.21 a, is acquired approximately 10 minutes after removal of the sample from the UHV system. The spectrum shows 4 peaks, located at ~ 216 cm^{-1} , 281 cm^{-1} , 385 cm^{-1} and 455 cm^{-1} . In cross polarisation configuration, only a slightly smaller Raman peak at 385 cm^{-1} and the unaltered peak at 455 cm^{-1} remain visible. The difference with the spectrum observed for silicene on $\text{Ag}(111)$, shown in the panel b, points to a modification of the structure of the 2D silicon layer. Interestingly, the 385 cm^{-1} is a peak observed in CaSi_2 crystals and assigned to the out-of-plane vibration of the Si nanosheets that alternate with Ca planes [115]. At the same time, the 216 cm^{-1} mode which was assigned to the out-of-plane vibrations in silicene/ $\text{Ag}(111)$ is still visible and shows a polarisation dependency, completely disappearing in cross polarisation configuration. The plausible in-plane vibrational mode, located at 455 cm^{-1} is different from the one detected in CaSi_2 structures, which is located at 420 cm^{-1} . The in-plane mode is redshifted if compared with the pristine silicene/ $\text{Ag}(111)$ structure. This can be a sign of a longer Si-Si bond, as evidenced in the case of silicene grown on $\text{Au}(111)$. The 281 cm^{-1} cannot be explained by referring it to known vibrational modes and could be related to a new Raman active mode appearing due to a change in the silicene structure triggered by the interaction with the CaF_2 top layer.

A possible explanation for the observed spectrum can be given by assuming that the Ca atoms in the CaF₂ layer are inducing a rearrangement of the silicon atoms. This structural modification is changing both the out-of-plane and in-plane vibration frequencies of the silicene layer. Possibly, the buckling height of the silicene layer changes to a value similar to what is observed in the Si planes in CaSi₂, as signalled by the appearance of a strong peak at 385 cm⁻¹. Due to energetic reasons, the in plane vibrational modes change too. Notably, this structural change is happening without the formation of Ca-Si bonds, as evidenced by the XPS data. Large differences in the in-plane vibrational modes indicate that the final structure is different from both the initial silicene/Ag(111) structure and from the silicon nanosheets observed in CaSi₂ structures. Most importantly, the structure maintains a 2D nature, as indicated by the absence of the 520 cm⁻¹ peak related to crystalline sp³ silicon and by the presence of out-of-plane vibrational modes.

3.3.4 Optical Properties

The grown stack of CaF₂/silicene has been analysed using an Alpha-SE spectroscopic ellipsometer (J.A. Woollam), with a spectral range going from 1.4 to 3.3 eV. The sample has been analysed, in reflection mode, with a fixed angle of incidence of 70°. A first acquisition has been performed just shortly after removing the sample from the UHV system, while a second one was collected after 2 days, when the silicene layer was already completely degraded and no Raman signal could be detected anymore.

The Psi (red) and Delta (blue) values for the 10 nm CaF₂/1 ML silicene/Ag(111) stack, before (light colours) and after oxidation (dark colours), are shown in Fig. 3.22 a. The variation upon silicene oxidation is clearly evident. The data acquired from the CaF₂/oxidised silicene/Ag(111) sample can be well fitted by using a rather simple two-layers optical model. Ellipsometry data of CaF₂ grown by MBE are usually modelled by using the Bruggeman effective medium [116] approximation, where a mixture of two material are considered. In this case the layer is composed by ~ 83 % of its volume by pure CaF₂ and the remaining ~ 17% by voids. The porosity level of the grown material is similar to what is reported in literature for MBE-grown CaF₂, where a void fractions of ~ 20% is measured [117]. Overall, the model is composed by an Ag substrate and a 11.6 nm thick Bruggeman layer, describing the CaF₂. The degraded silicene layer is not included in the model as it is known that when silicene on Ag(111) degrades, it dewets from the substrate, forming SiO₂ pillars that cannot be regarded as a layer in the optical model [54].

Subsequently, the fitted model was applied to the data of the CaF₂/1 ML silicene/Ag(111) sample. Obviously, this model cannot fit the unoxidised data. An additional "B-Spline" layer was added to the optical model, to parametrise the pristine silicene. This model calculates a basis spline through evenly spaced points in eV for both n and k, adapting it to the measured data. To ensure that the fitting process does not generate unphysical results, the Kramers-Kronig consistency is enforced, allowing the program to find only those results that satisfy the Kramers-Kronig relation. The optical parameters, n and k, resulting from the fitting process are shown in Fig. 3.22 b. Notably, the extinction coefficient k is much higher than the ones reported for diamond silicon or for amorphous silicon [118, 119]. The

absorbance (A) of the silicene layer can be derived from the extinction coefficient k using the Beer-Lambert law.

$$\frac{I}{I_0} = e^{-\frac{2\pi k(\lambda)}{\lambda} \cdot d} \quad (3.2)$$

$$A = \log_{10}\left(\frac{I_0}{I}\right) = \log_{10}(e) \cdot \frac{2\pi k(\lambda)}{\lambda} \cdot d \quad (3.3)$$

Where d is the thickness of the layer and λ the light wavelength. The absorbance is calculated using the extracted k values and a thickness of ~ 0.3 nm, which well approximate the thickness of a 2D layer. The obtained absorbance is plotted in Fig. 3.22 c in units of $\pi\alpha$, where α is the fine structure constant.

There, it is confronted with the absorbance of 1 ML of a-Si, which was derived from the tabulated k values. Notably, the absorbance obtained for the silicene layer is almost 3 times higher than the one of a-Si in the higher energy limit. Towards the infrared region, instead, the difference is much bigger: while the a-Si curve approaches zero, the absorbance of silicene slowly decreases, staying above 1. This behaviour is particularly of interest as 2D materials with an hexagonal structure such as silicene, graphene and germanene are expected to show an absorbance tending to $1 \cdot \pi\alpha$ in the infrared [120]. Therefore the derived absorbance indicates that the examined layer might still possess a honeycomb-like structure. At the same time, however, silicene is expected to show an absorption peak at 1.6 eV due to a strong transition strength at the saddle points of the valence and conduction bands [120], that cannot be observed here. The deviation from the expected behaviour of a freestanding silicene layer is, however, not surprising due to the structural modifications induced by the Ag(111) substrate and the CaF₂ insulation layer.

Overall, the data reported here clearly describe a layer with very different optical properties, compared to bulk diamond or amorphous silicon and with characteristic that are typical of a 2D honeycomb-structured material. The high absorbance in the visible range makes this material extremely interesting for photovoltaic application. A possible extension of this work should focus on the investigation of the optical and electrical properties of a silicon monolayer stacked between CaF₂ layers.

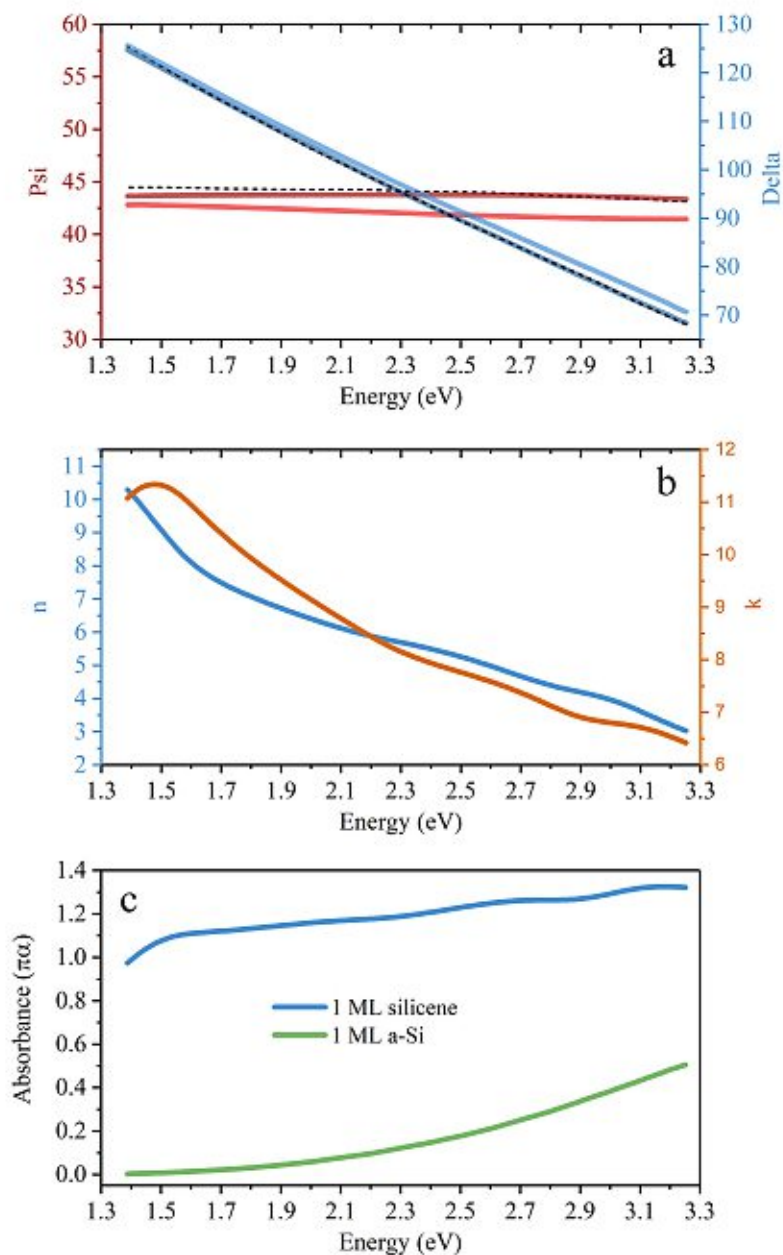


Figure 3.22: a) Psi (red) and Delta (blue) values for: 10 nm CaF₂/1 ML silicene/Ag(111) (light colours). 10 nm CaF₂/oxidised silicene/Ag(111) (dark colours); Dashed black lines represent the values from the adopted fitting model; b) optical parameters (*n* - blue, *k* - orange) of the pristine silicene layer extracted from the ellipsometry model ; c) absorbance derived from the extinction coefficient *k* of the silicene layer (blue) and of a 0.33 nm of a-Si (green).

Chapter 4

Summary and Outlook

In this work, several findings concerning the growth and characterisation of a two-dimensional phase of silicon have been presented.

Initially, the silicene growth on an Ag(111)/mica substrate has been investigated using a comprehensive set of experimental techniques. LEED and LEEM tools have been employed to show how 1 ML silicene - i.e. a single layer of Si atoms - grows on this substrate, at two different growth temperatures of 260°C and 300°C. The lower temperature regime gives rise to a mixture between two different phases, identified as 4×4 and $\sqrt{13} \times \sqrt{13}$ R13.9° reconstructions with respect to the Ag(111) crystal. At higher temperature a new phase is formed, showing a $2\sqrt{3} \times 2\sqrt{3}$ R30° reconstruction. LEEM micrograph showed a different growth behaviour, depending on the temperature. At lower temperatures, triangular islands are observed forming on the Ag(111) terraces and a full monolayer is obtained from their expansion and growth from the Ag(111) step-edges. At higher temperature the growth is seeded mainly from the step-edges, expanding circularly on the substrate. LEEM analysis shows also that, at higher growth temperature, the grown layer becomes unstable when surpassing the 1 ML coverage, triggering a $sp^2 \rightarrow sp^3$ hybridisation transition. Differently, at lower temperature, the growth can be sustained without observing a similar behaviour. Polarised Raman spectroscopy was used to characterise the vibrational properties of the silicene layer. To do so, the layer must be protected from oxidation, as the analysis is performed under ambient conditions. This has been achieved by capping the grown layer directly in UHV with few-layers graphene flakes, which are impermeable to H_2O and O_2 molecules. Raman spectra revealed two vibrational modes, at 216 cm^{-1} and 515 cm^{-1} . Polarised measurement showed that the lower frequency peak is totally symmetrical, allowing to assign it to out-of-plane vibrations. The higher frequency peak, instead, is the signature of in-plane vibrations. The observed spectrum confirmed the hexagonal nature of the silicene structure. Raman spectroscopy further revealed a structural change for samples with a silicon coverage between 1 ML and 2 ML, evidenced by the appearance of additional peaks. This data hint at the possibility of realising a multilayered silicene structure, with a structure different from the one of bulk diamond-like silicon.

XPS data revealed that the Si2p peak for 1 ML silicene is shifted by 0.4 eV to lower binding energies, with respect to the position of the same peak in bulk silicon, and can be regarded as a sign of the different hybridisation of the Si atoms. ARUPS experiments were employed to study the band structure of the grown layer along the $\Gamma \rightarrow K$ direction

of the Brillouin zone as silicene is expected to show a Dirac cone at the K point. The acquired data, however, showed no sign of a Dirac cone, detecting, instead, a seemingly linear band reaching the Fermi level. This hints at a possible hybridisation between the Si and Ag atoms at the interface, resulting in a degradation of the electronic properties of the silicene layer.

Clearly, the silicene layer obtained on an Ag(111) substrate shares many properties with freestanding silicene, deriving from their two-dimensional nature. The presented results show that, however, the interaction between Ag and Si atoms leads to a degradation of the electronic properties of silicene. For these reasons, Ag(111) can be regarded as the best platform for the investigation of the structural properties of a 2D silicon layer, while not being suitable for any electrical characterisation.

In the second part of this thesis, the growth of silicene on Au(111) is considered, as this material has been indicated as a viable substrate for the growth of a silicene layer with pristine electronic properties. 1 ML of silicon is deposited on Au(111) at a substrate temperature of 260 °C. Once again, the results are investigated using a vast number of experimental techniques. By acquiring a μ -diffraction pattern, the grown structure is analysed down to a small circular area with a diameter of ~ 185 nm. The acquired signal was successfully modelled by considering a surface layer composed by three different structures. Two structures are surface gold-silicides, the third is a silicene phase, rotated by 30° with respect to the Au(111) and with a lattice parameter of 4.1 Å, much longer than the expected value of 3.81 Å for a freestanding silicene layer. Such a longer lattice parameter allows to obtain a good lattice matching between Au(111) and silicene. To further examine the structure of this silicene layer, polarised Raman spectroscopy is used. Similarly to the case of Ag(111), the silicene layer needs to be protected from oxidation. This is achieved, once again, by encapsulation under few-layers graphene flake. Additionally, also few-layers hBN flakes are used, as the high transparency of this material guarantees a better signal to noise ratio in the Raman measurements. The observed spectrum is characterised by 3 main peaks, centred at 83 cm^{-1} , 100 cm^{-1} and at 435 cm^{-1} . The higher frequency peak is clearly composed by two modes and can be fitted by a combination of two Lorentzian functions, with centres at 429 and 437 cm^{-1} . The lower frequency modes, instead, are fitted by a single Lorentzian function. Polarised measurements showed that the 100 cm^{-1} peak is completely suppressed in cross polarisation configuration, while the 429 and 437 cm^{-1} ones are strongly reduced. This result is compared to first-principles calculations of a biaxially strained silicene layer, with a lattice parameter of 4.1 Å. The calculated Raman spectrum is characterised by two peaks, positioned at 98.6 cm^{-1} and at 447.3 cm^{-1} . The position of the calculated peaks agree well with the experimental observations. The polarisation dependency, however, does not fit the simulations. The splitting of the in-plane vibrational modes, observed in the experiments, reminds of the splitting of the graphene in-plane modes when uniaxial strain is applied, suggesting that the observed structure is slightly more strained along one specific direction of its lattice. The calculations are repeated for an additional 1% strain applied along the zig-zag direction of the silicene layer. With this modification, the out-of-plane mode shifts up to 102.9 cm^{-1} . At the same time the in-plane vibrational modes get redshifted and split up in two distinct peaks, as the degeneration is lifted, at 433.9 cm^{-1} and 439.5 cm^{-1} . Additionally, their polarisation dependency

changes, showing a clear intensity reduction in cross polarisation configuration. Overall, the calculations clearly show that the observed spectrum is related to a highly biaxially strained silicene layer, with a strain level of 7.6% along one direction and of 8.6% along the opposite one. XPS measurements revealed that the Si2p peak is shifted to lower binding energies if compared to intrinsic bulk sp^3 silicon. The shift, however, is less pronounced than in the case of silicene on Ag(111), possibly due to the presence of surface silicides. The measured peak shows a distinct asymmetry, with a longer tail towards higher binding energies, a characteristic that could be the signature of sp^2 -hybridised silicon atoms. ARUPS measurements are also performed, to probe the band structure of the grown layer. The scans are directed along the $\Gamma \rightarrow K$ and the $\Gamma \rightarrow M$ direction of Au(111) Brillouin zone. After the deposition of the silicon monolayer, a band appears clearly in both the spectra. Along the $\Gamma \rightarrow M$ direction, the band reaches a plateau at $k_M \approx 1.25 \text{ \AA}^{-1}$, at a binding energy level of $E_B \approx 0.5 \text{ eV}$. Along the $\Gamma \rightarrow K$ direction, the detected band is seemingly crossing the Fermi level at $k_K \approx 1.3 \text{ \AA}^{-1}$. Two possible interpretations are proposed: in the first, this result is considered to be related to a hybridisation effect with the Au substrate, similarly to what can be observed for Ag(111). The second interpretation stems from the observation that a biaxially strained silicene phase rotated by 30° on Au(111) can be described by using a unit cell with a lattice parameter 5 times bigger than the one of Au(111) and with a 0° rotation, due to the corresponding lattice sites between silicene and Au(111). Since the position of the k_K and k_M points could be related to a structure with a 5-times periodicity, the observed bands can be generated by such a larger structure.

The results presented in this second section clearly support the existence of a highly biaxially strained silicene phase, with strain levels higher than 7%. While its electronic properties are not completely understood yet, requiring additional experiments to clarify whether hybridisation with the Au atoms exists or not, this silicene phase is an exceptional platform for studying the effects of high strain in 2D silicon as, for example, the generation of hole-doped Dirac states, expected for strain levels higher than 5 % [91].

In the last section of this thesis, the possible integration of silicene and CaF_2 is investigated, in order to find a reliable process for the realisation of a dielectric layer directly interfaced with silicene. Crystalline CaF_2 is a formidable insulator, even for extremely thin layers ($\sim 2 \text{ nm}$), with a wide band gap of 12.1 eV and a high dielectric constant ($\epsilon = 8.43$). The lattice parameter of $\text{CaF}_2(111)$ is perfectly matching the one of silicene. A good epitaxial relation it is therefore expected, which could be exploited to form a perfect interface. Moreover, $\text{CaF}_2(111)$ is fluorine terminated, with no dangling bonds. For these reasons, CaF_2 is a promising material for the realisation of a gate insulator interface for silicene with low leakage currents. CaF_2 is deposited on a freshly grown monolayer silicene/Ag(111) at a temperature of $260 \text{ }^\circ\text{C}$ by thermal evaporation. LEED images are acquired after the deposition of 5 ML CaF_2 , evidencing a good epitaxial growth with preferred growth direction depending on the orientation of the silicene domains. In contrast to this, the growth of CaF_2 directly on Ag(111) results in a layer composed by randomly oriented domains. To investigate the conditions of the materials at the interface, XPS spectra are acquired before and after the deposition of 2 ML of CaF_2 . The calibrated F1s and Ca2p peaks show the expected 2:1 stoichiometry for the grown CaF_2 . The Si2p peak shifts

by only 0.09 eV upon deposition of CaF_2 , demonstrating that no Ca-Si or F-Si bonds are formed, which would shift the Si2p peak by 0.4 eV and -0.9 eV respectively. UV photoemission spectroscopy is used to probe the valence band of the grown CaF_2 . A peak can be detected in the region between 8 and 12 eV, which is associated to the F2p valence band. No additional impurities-related states can be detected between this band and the Fermi level, ensuring the good insulating properties of the grown layer.

By depositing 20 ML of CaF_2 it was possible to slow down the degradation of silicene, allowing to perform Raman analysis of the buried layer. The Raman spectrum is characterised by 4 peaks, centred at $\sim 216 \text{ cm}^{-1}$, 281 cm^{-1} , 385 cm^{-1} and 455 cm^{-1} . In cross polarisation configuration, the 216 cm^{-1} peak is completely suppressed while the 385 cm^{-1} one is largely reduced. The 385 cm^{-1} peak is detected also for Si nanosheets in CaSi_2 structures and corresponds to the out-of-plane vibration of the Si atoms. The in-plane vibrational mode, centred at 455 cm^{-1} , does not match the one detected in CaSi_2 . The out-of-plane mode for pristine silicene/Ag(111) is still visible at 216 cm^{-1} . These findings strongly suggest that the Ca atoms of the CaF_2 structure are inducing a rearrangement of the silicene structure. The observed structure is different from both the pristine silicene/Ag(111) structure and the planar Si structures observed in CaSi_2 . Most importantly, the observed spectrum shows that the buried structure maintains a two-dimensional nature. Finally, the silicene layer below 20 ML CaF_2 is analysed using spectroscopic ellipsometry. The n and k parameters of silicene are extracted by comparing the optical response of the pristine sample with the one of a degraded silicene layer. The absorbance of the silicene layer is derived from the extinction coefficient, for a spectral range going from 1.3 eV to 3.3 eV. The results show that the pristine silicene layer has a much higher absorption in the visible range, compared to an equivalent layer of amorphous silicon.

In conclusion, this work presents a comprehensive study of the properties of a 2D allotrope of silicon, commonly known as silicene. By using a large combination of experimental techniques, it aims at providing a comprehensive overview of the properties of this material and, at the same time, it proposes new processes that can be exploited, in the future, for the integration of silicene in next generation electronic devices. The main findings presented here can be summarised as follows:

1. Development of a novel approach for the passivation of highly reactive 2D materials by in situ encapsulation under few layer graphene or hBN flakes.
2. Growth and characterisation of single and multi layer silicene structures on Ag(111), with particular emphasis given to the study of the peculiar vibrational properties, signature of two-dimensional structures.
3. Growth and identification of a new silicene phase on Au(111), characterised by a high biaxial strain.
4. Development of a process for the realisation of an ultra-thin crystalline CaF_2 dielectric layer on silicene, able to preserve the two-dimensional nature of the buried layer.

The results presented in this thesis open up interesting topics for future analysis. Hereafter are presented some of the most important questions that still need to be answered:

1. The analysis of silicene on Au(111) has shown the presence of a highly biaxially strained phase. Future investigations should focus on the clear determination of the electronic properties of this phase, determining whether Dirac states can be observed. Particular attention should be dedicated to the search of p-doped Dirac states, which are expected to arise in biaxially strained silicene.
2. Future works should investigate the electronic properties of the ultra-thin crystalline CaF_2 gate layers grown on silicene, completely determining their insulation capabilities.
3. The silicene structure that can still be observed under CaF_2 sparks hope that a silicene phase could be obtained on a CaF_2 substrate. Future studies should focus on the possibility of realising a CaF_2 /silicene/ CaF_2 stack, which could represent one of the most promising approaches for the engineering of silicene- and, more generally, Xenes-based electronic devices.

List of abbreviations

Ag	Silver
ARUPS	Angle Resolved UV Photoemission Spectroscopy
Au	Gold
C	Carbon
CaF₂	Calcium Fluoride
CCD	Charge-coupled Device
CVD	Chemical Vapour Deposition
DFT	Density Functional Theory
EBE	e-Beam Evaporator
Ge	Germanium
h-BN	hexagonal Boron Nitride
HfS₂	Hafnium Disulfide
HOPG	Highly Oriented Pyrolytic Graphite
LEED	Low Energy Electron Diffraction
LEEM	Low Energy Electron Microscope
MBE	Molecular Beam Epitaxy

Mo	Molybdenum
MoS₂	Molybdenum Disulfide
NbS₂	Niobium Disulfide
NbSe₂	Niobium Diselenide
PES	Photoemission Spectroscopy
RHEED	Reflection High Energy Electron Diffraction
Si	Silicon
TaS₂	Tantalum Sulfide
TMD	Transition Metal Dichalcogenide
UHV	Ultra High Vacuum
UPS	UV Photoemission Spectroscopy
VSe₂	Vanadium Diselenide
W	Tungsten
WS₂	Tungsten Disulfide
XPS	X-ray Photoemission Spectroscopy

Appendix

MATLAB script for analysis and stitching of ARUPS data

```
1 %IMAGE FILE SETTINGS
2     image_file_name_i='silicene';
3     image_number_start=0;
4     image_number_end=45;
5     image_stepincrease=1;
6
7 %ENERGY SETTINGS
8     energy_start=2.3; % Binding Energy Start
9     energy_end=0; % Binding Energy End
10    energy_resolution=0.01; % Binding Energy Resolution (Step)
11    photon_energy=21.2; % Excitation Energy
12    work_function=5.31; %4.74 Ag(111) 5.31 Au(111) % Work
        Function of Substrate
13
14 %ROTATION SETTINGS
15    angle_start=30; % Starting Angle (on Manipulator)
16    angle_end=45; % Ending Angle (on Manipulator)
17    angle_step=1; % Rotation Step (usually 1 or 2 for manual
        rotation)
18
19 %LENS AND SLIT SETTINGS
20    slit_x=20; % horizontal physical size of chosen slit (mm)
21    slit_y=0.1;%75; % vertical physical size of chosen slit
22    lens_total_angle=20; % total angle for chosen lens mode (
        consider slit and iris clipping) – From Manual
23    energy_channels=300; % Number of energy channels chose for
        experiment
24    non_energy_channels=300; % Number of non energy channels (k
        in opposite direction as rotation) chose for experiment
25
26
27 %SAVE SETTINGS
28    slice_averaging=35; % average on non_energy_channels. Must
        be < non_energy_channels
```

```

29     save_slice=false; % if you want to save a slice along
        perpendicular direction
30     slice_position=0.1; % chosen position of slice , between -1
        and 1. Default 0, cuts in the middle
31     gamma=0.6; %1.4 %Change gamma of Final Image
32     c_in=[0 0.7]; %0.5 %Change Contrast of Final Image
33     c_out=[0 1]; %Change Contrast of Initial Data
34
35
36 %PHYSICAL CONSTANTS (Do not change!)
37     e_mass=9.10938E-31;
38     h_bar=1.05457E-34;
39     e_conv=1.60218e-19;
40
41     t = cputime;
42
43 %Calculation of needed variables
44     y_angle=lens_total_angle*slit_y/slit_x;
45     energy_steps=round((abs(energy_start-energy_end)/
        energy_resolution))+1
46     azimuth_angle_steps=(abs(image_number_start-image_number_end
        )/image_stepincrease)+1;
47     slices=round((angle_end-angle_start)/y_angle)
48     positions=round([1:((image_number_end-image_number_start)/
        image_stepincrease)-1]*((angle_step)/y_angle));
49
50
51 %Initialisation of needed variables
52     Image_Collection=zeros(energy_steps , non_energy_channels ,(
        image_number_end-image_number_start)/image_stepincrease);
53     Results_Matrix3D=zeros(energy_steps , non_energy_channels ,
        slices);
54     image_slice=(NaN(energy_steps , slices));
55
56
57     fclose('all');
58
59 %Load Data into Main Matrix
60
61     for azm_index = image_number_start:image_stepincrease:
        image_number_end
62         normal_index=azm_index-image_number_start+1; % starts
            from 1
63         sprintf('%0.2f %%', normal_index/azimuth_angle_steps*100)
64         file_name_o=sprintf('_%d', azm_index);

```

```

65     file_name_e=sprintf( '.xy' ,azm_index);%.1d (2)
66     file_name=strcat( image_file_name_i , file_name_o );
67     file_name=strcat( file_name , file_name_e )
68     Data=importdata( file_name );
69
70     Results_Matrix=zeros( energy_steps , non_energy_channels );
71     for ch_index=1:non_energy_channels
72         real_index=(ch_index-1)*energy_steps ;
73         Results_Matrix(1:energy_steps , ch_index)=flipud (
74             Data(real_index+1:real_index+energy_steps ,2) )
75         ;
76         Results_Matrix(1:energy_steps , ch_index)=
77             Results_Matrix(1:energy_steps , ch_index)+abs(
78                 min(Results_Matrix(1:energy_steps , ch_index)))
79         ;
80     end
81
82     %mean( Results_Matrix , ' All ' )
83     Results_Matrix= (Results_Matrix-min(Results_Matrix));
84     Results_Matrix= Results_Matrix./mean(Results_Matrix , ' All
85         ' );
86
87     %Results_Matrix= imadjust( mat2gray( Results_Matrix ) , c_in ,
88         c_out , gamma );
89     Image_Collection( : , : , normal_index)=Results_Matrix ;
90     image=uint16( Results_Matrix );
91     if (save_frames)
92         imwrite( image , sprintf( '%d.tif' , (normal_index-1)*
93             angle_step ) );
94     end
95 end
96
97 %Transfer Slices into Result Matrix
98
99 Results_Matrix3D( : , : , 1)=Image_Collection( : , : , 1 );
100 Results_Matrix3D( : , : , slices)=Image_Collection( : , : , (
    image_number_end-image_number_start)/image_stepincrease );

```

```

101     for slice_index = 1:length(positions)
102         Results_Matrix3D(:, :, positions(slice_index))=
            Image_Collection(:, :, slice_index+1);
103     end
104
105
106
107
108 %Average Slices
109
110     temp=zeros(energy_steps,1,slices);
111
112     for p=1:slice_averaging
113         temp(:,1,:)=temp(:,1,:)+double(Results_Matrix3D(:, round(
            non_energy_channels/2)+round(slice_position*
            non_energy_channels/2)-round(slice_averaging/2)+p,:))
            ;
114     end
115     temp(:,1,:)=temp(:,1,:)/slice_averaging;
116
117
118     image_slice(:,1)=temp(:,1,1);
119     image_slice(:,slices)=temp(:,1,slices);
120     for slice_index = 1:length(positions)
121         image_slice(:, positions(slice_index))=temp(:,1, positions(
            slice_index));
122
123     end
124
125
126
127 %Adjust Contrast
128
129
130     image_slice(:,1)=imadjust(mat2gray(image_slice(:,1)),c_in ,
            c_out ,gamma);
131     image_slice(:,slices)=imadjust(mat2gray(image_slice(:,slices)
            )),c_in ,c_out ,gamma);
132
133     for slice_index = 1:length(positions)
134         image_slice(:, positions(slice_index))=imadjust(mat2gray(
            image_slice(:, positions(slice_index))),c_in ,c_out ,gamma)
            ;
135
136     end

```

```
137
138
139 %Interpolate missing data and Plot
140
141
142     used_positions = unique(sort([positions,1,slices]));
143     CM = image_slice;
144     degi = angle_start;
145     degf = angle_end; %Degree limits
146     eng = energy_start; %Energy limits
147     b = size(CM,1); %Nr. of rows y direction
148     a = size(CM,2); %Nr. of rows x direction
149
150     x = [];
151     y = [];
152
153     for i = 1:slices
154
155         x(i) = ((degf-degi)/slices * (i-1))+degi;
156
157         i = i + 1;
158     end
159
160     for i = 1:b
161
162         y(i) = eng/b * (i-1);
163
164         i = i + 1;
165     end
166     x;
167
168
169     figure(1)
170     F1 = inpaint_nans(CM,3);
171
172
173
174     surf(x,y,F1, 'LineStyle', 'none');
175     az = 0;
176     el = -90; %90,30
177     view(az, el);
178     colormap('gray');
179     xlim([degi degf]);
180     ylim([0 eng]);
181     xlabel('Angle [deg]');
```



```

182     ylabel('Energy [eV]');
183     title('Band Slices');
184     saveas(gcf, 'Band - Slices.png')
185
186
187
188
189     F = inpaint_nans(CM,3);
190     imwrite(uint16(F), 'Result.tif')
191
192
193
194
195     figure(2)
196
197     surf(x,y,F, 'LineStyle', 'none', 'EdgeColor', 'none');
198     az = 0; %0,-45
199     el = -90; %90,30
200     view(az, el);
201     colormap('gray');
202
203     xlim([degi degf]);
204     ylim([0 eng]);
205     xlabel('Angle [deg]');
206     ylabel('Energy [eV]');
207     title('Band Interpolated');
208     saveas(gcf, strcat('Band - Interpolated_', num2str(
209         slice_position), '.png'))
210
211     imwrite(F, 'result_noaxis.tif')
212
213     %Calculate conversion between rotation and k space, apply image
214     stretch and plot
215
216     stretch_factor_max=sqrt((photon_energy-work_function))/sqrt
217         ((photon_energy-work_function)-energy_start);
218
219     x_f=(angle_end/angle_end)/stretch_factor_max;
220     x_i=(angle_start/angle_end)/stretch_factor_max-(angle_start/
221         angle_end);
222
223     I = imread('result_noaxis.tif');

```

```

223     udata = [0 1];   vdata = [0 1];
224
225     tform = maketform('projective',[ 0 0; 1 0; 1 1; 0 1],...
226                       [0 0; 1 0; x_f 1; x_i 1]);
227
228     [B,xdata,ydata] = imtransform(I,tform,'bicubic', ...
229                                   'udata',udata,...
230                                   'vdata',vdata,...
231                                   'size',size(I),...
232                                   'fill',128);
233
234
235
236     xnew = [];
237     ynew = [];
238
239     for i = 1:size(B,2)
240
241         xnew(i) = sin(deg2rad((((angle_end-angle_start)/size(B
242                               ,2) * (i-1))+angle_start)))*sqrt(2*e_conv*(
243                               photon_energy-work_function)/h_bar*(10^-10);
244
245     end
246
247     for i = 1:size(B,1)
248
249         ynew(i) = energy_start/size(B,1) * (i-1);
250
251     end
252
253     figure(3)
254
255     surf(xnew,ynew,B,'LineStyle','none','EdgeColor','none');
256     az = 0; %0,-45
257     el = -90; %90,30
258     view(az, el);
259     c = gray;
260     c = flipud(c);
261     colormap(c);
262
263     xlim([xnew(1,1) xnew(1,size(xnew,2))]);
264     ylim([0 energy_start]);
265     xlabel('$K_{//} [\AA^{-1}]$', 'Interpreter','latex','

```

```
Fontname', 'TimesNewRoman');
266 ylabel('Binding Energy [eV]', 'Interpreter', 'latex', 'Fontname
    ', 'TimesNewRoman');
267 % title(' - $\Gamma K$', 'Interpreter', 'latex', 'Fontname', '
    TimesNewRoman');
268 saveas(gcf, strcat('Band - Interpolated_', num2str(
    slice_position), '_Stretched.png'))
269
270
271
272 e = cputime-t;
273 sprintf('Finished all operations in %.2f s', e)
```

Bibliography

- [1] Moore, G. E. Cramming More Components Onto Integrated Circuits. *Proceedings of the IEEE* **86**, 82–85 (1998). <http://ieeexplore.ieee.org/document/658762/>.
- [2] Fischetti, M. V., Fu, B. & Vandenbergh, W. G. Theoretical Study of the Gate Leakage Current in Sub-10-nm Field-Effect Transistors. *IEEE Transactions on Electron Devices* **60**, 3862–3869 (2013).
- [3] Vogt, P. *et al.* Silicene: Compelling Experimental Evidence for Graphenelike Two-Dimensional Silicon. *Physical Review Letters* **108**, 155501 (2012). <https://link.aps.org/doi/10.1103/PhysRevLett.108.155501>.
- [4] Guzmán-Verri, G. G. & Lew Yan Voon, L. C. Electronic structure of silicon-based nanostructures. *Physical Review B* **76**, 075131 (2007). <https://link.aps.org/doi/10.1103/PhysRevB.76.075131>.
- [5] Zhao, J. *et al.* Rise of silicene: A competitive 2D material. *Progress in Materials Science* **83**, 24–151 (2016). <http://www.sciencedirect.com/science/article/pii/S0079642516300068>.
- [6] Drummond, N. D., Zólyomi, V. & Fal’ko, V. I. Electrically tunable band gap in silicene. *Physical Review B* **85**, 075423 (2012). <https://link.aps.org/doi/10.1103/PhysRevB.85.075423>.
- [7] Tao, L. *et al.* Silicene field-effect transistors operating at room temperature. *Nature Nanotechnology* **10**, 227–231 (2015). <https://www.nature.com/articles/nano.2014.325>.
- [8] Liu, C.-C., Feng, W. & Yao, Y. Quantum Spin Hall Effect in Silicene and Two-Dimensional Germanium. *Physical Review Letters* **107**, 076802 (2011). <https://link.aps.org/doi/10.1103/PhysRevLett.107.076802>.
- [9] Liu, F., Liu, C.-C., Wu, K., Yang, F. & Yao, Y. d+id’ Chiral Superconductivity in Bilayer Silicene. *Physical Review Letters* **111**, 066804 (2013). <https://link.aps.org/doi/10.1103/PhysRevLett.111.066804>.
- [10] Xu, C. *et al.* Giant magnetoresistance in silicene nanoribbons. *Nanoscale* **4**, 3111–3117 (2012). <https://pubs.rsc.org/en/content/articlelanding/2012/nr/c2nr00037g>.
- [11] Feynman, R. P. There’s Plenty of Room at the Bottom (California Institute of Technology, 1959).

- [12] Novoselov, K. S. *et al.* Electric Field Effect in Atomically Thin Carbon Films. *Science* **306**, 666–669 (2004). <https://science.sciencemag.org/content/306/5696/666>.
- [13] Hohenberg, P. C. Existence of Long-Range Order in One and Two Dimensions. *Physical Review* **158**, 383–386 (1967). <https://link.aps.org/doi/10.1103/PhysRev.158.383>.
- [14] Mermin, N. D. & Wagner, H. Absence of Ferromagnetism or Antiferromagnetism in One- or Two-Dimensional Isotropic Heisenberg Models. *Physical Review Letters* **17**, 1133–1136 (1966). <https://link.aps.org/doi/10.1103/PhysRevLett.17.1133>.
- [15] Mounet, N. *et al.* Two-dimensional materials from high-throughput computational exfoliation of experimentally known compounds. *Nature Nanotechnology* **13**, 246–252 (2018). <https://www.nature.com/articles/s41565-017-0035-5>.
- [16] Novoselov, K. S. *et al.* Two-dimensional gas of massless Dirac fermions in graphene. *Nature* **438**, 197–200 (2005). <https://www.nature.com/articles/nature04233>.
- [17] Nicolosi, V., Chhowalla, M., Kanatzidis, M. G., Strano, M. S. & Coleman, J. N. Liquid Exfoliation of Layered Materials. *Science* **340** (2013). <https://science.sciencemag.org/content/340/6139/1226419>.
- [18] Bae, S. *et al.* Roll-to-roll production of 30-inch graphene films for transparent electrodes. *Nature Nanotechnology* **5**, 574–578 (2010). <https://www.nature.com/articles/nnano.2010.132>.
- [19] Novoselov, K. S. *et al.* A roadmap for graphene. *Nature* **490**, 192–200 (2012). <https://www.nature.com/articles/nature11458>.
- [20] Lopes, J. M. J. MBE Growth of Graphene. In *Molecular Beam Epitaxy*, 395–409 (John Wiley & Sons, Ltd, 2019). <https://onlinelibrary.wiley.com/doi/abs/10.1002/9781119354987.ch24>.
- [21] Takeda, K. & Shiraishi, K. Theoretical possibility of stage corrugation in Si and Ge analogs of graphite. *Physical Review B* **50**, 14916–14922 (1994). <https://link.aps.org/doi/10.1103/PhysRevB.50.14916>.
- [22] Cahangirov, S., Topsakal, M., Aktürk, E., Şahin, H. & Ciraci, S. Two- and One-Dimensional Honeycomb Structures of Silicon and Germanium. *Physical Review Letters* **102**, 236804 (2009). <https://link.aps.org/doi/10.1103/PhysRevLett.102.236804>.
- [23] Pflugradt, P., Matthes, L. & Bechstedt, F. Silicene-derived phases on ag(111) substrate versus coverage: Ab initio studies. *Physical Review B* **89**, 035403 (2014). <https://link.aps.org/doi/10.1103/PhysRevB.89.035403>.
- [24] Dresselhaus, M. S., Dresselhaus, G. & Jorio, A. *Group theory: application to the physics of condensed matter* (Springer-Verlag, Berlin, 2008).

- [25] Aroyo, M. I. *et al.* Bilbao Crystallographic Server: I. Databases and crystallographic computing programs. *Zeitschrift für Kristallographie - Crystalline Materials* **221**, 15–27 (2006). <https://www.degruyter.com/view/journals/zkri/221/1/article-p15.xml>.
- [26] Tan, P. H. *et al.* The shear mode of multilayer graphene. *Nature Materials* **11**, 294–300 (2012). <https://www.nature.com/articles/nmat3245>.
- [27] Ashcroft, N. W. & Mermin, N. D. *Solid State Physics* (Holt, Rinehart and Winston, 1976).
- [28] Leggett, A. J. & Coish, B. Lecture 5: Graphene: Electronic band structure and Dirac fermions 12.
- [29] Kim, P. Graphene and Relativistic Quantum Physics. In Duplantier, B., Rivasseau, V. & Fuchs, J.-N. (eds.) *Dirac Matter*, Progress in Mathematical Physics, 1–23 (Springer International Publishing, Cham, 2017). https://doi.org/10.1007/978-3-319-32536-1_1.
- [30] Oughaddou, H. *et al.* Silicene, a promising new 2D material. *Progress in Surface Science* **90**, 46–83 (2015). <http://www.sciencedirect.com/science/article/pii/S0079681614000331>.
- [31] Kara, A. *et al.* A review on silicene — New candidate for electronics. *Surface Science Reports* **67**, 1–18 (2012). <http://www.sciencedirect.com/science/article/pii/S0167572911000483>.
- [32] Raman, C. V. & Krishnan, K. S. A New Type of Secondary Radiation. *Nature* **121**, 501–502 (1928). <https://www.nature.com/articles/121501c0>.
- [33] Gardiner, D. J. & Graves, P. R. (eds.) *Practical Raman Spectroscopy* (Springer-Verlag, Berlin Heidelberg, 1989). <https://www.springer.com/de/book/9783540502548>.
- [34] Wermelinger, T. & Spolenak, R. Stress Analysis by Means of Raman Microscopy. In Dieing, T., Hollricher, O. & Toporski, J. (eds.) *Confocal Raman Microscopy*, Springer Series in Optical Sciences, 259–278 (Springer, Berlin, Heidelberg, 2011). https://doi.org/10.1007/978-3-642-12522-5_12.
- [35] Cardona, M. & Ley, L. (eds.) *Photoemission in Solids I: General Principles*. Topics in Applied Physics (Springer-Verlag, Berlin Heidelberg, 1978). <https://www.springer.com/gp/book/9783662309193>.
- [36] Hertz, H. Über einen Einfluss des ultravioletten Lichtes auf die elektrische Entladung. *Annalen der Physik* **267**, 983–1000 (1887). <https://onlinelibrary.wiley.com/doi/abs/10.1002/andp.18872670827>.
- [37] Einstein, A. Über einen die Erzeugung und Verwandlung des Lichtes betreffenden heuristischen Gesichtspunkt. *Annalen der Physik* **322**, 132–148 (1905). <https://onlinelibrary.wiley.com/doi/abs/10.1002/andp.19053220607>.

- [38] Reinert, F. & Hüfner, S. Photoemission spectroscopy—from early days to recent applications. *New Journal of Physics* **7**, 97–97 (2005). <https://iopscience.iop.org/article/10.1088/1367-2630/7/1/097>.
- [39] Davisson, C. J. & Germer, L. H. Reflection of Electrons by a Crystal of Nickel. *Proceedings of the National Academy of Sciences* **14**, 317–322 (1928). <https://www.pnas.org/content/14/4/317>.
- [40] Kittel, C. *Introduction to Solid State Physics* (2018), 8th edn. <https://www.wiley.com/en-ps/Kittel%27s+Introduction+to+Solid+State+Physics%2C+8th+Edition%2C+Global+Edition-p-9781119454168>.
- [41] Mark, P., Levine, J. D. & McFarlane, S. H. Atomic Structure of the Si(111) 7x7 Surface. *Physical Review Letters* **5** (1977).
- [42] Wang, Z.-j. *et al.* Simultaneous N-intercalation and N-doping of epitaxial graphene on 6H-SiC(0001) through thermal reactions with ammonia. *Nano Research* **6**, 399–408 (2013). <https://doi.org/10.1007/s12274-013-0317-7>.
- [43] Wood, E. A. Vocabulary of Surface Crystallography. *Journal of Applied Physics* **35**, 1306–1312 (1964). <https://aip.scitation.org/doi/abs/10.1063/1.1713610>.
- [44] Park, R. L. & Madden, H. H. Annealing changes on the (100) surface of palladium and their effect on CO adsorption. *Surface Science* **11**, 188–202 (1968). <http://www.sciencedirect.com/science/article/pii/0039602868900666>.
- [45] Cho, A. Y. & Arthur, J. R. Molecular beam epitaxy. *Progress in Solid State Chemistry* **10**, 157–191 (1975). <http://www.sciencedirect.com/science/article/pii/0079678675900059>.
- [46] Jennings, S. G. The mean free path in air. *Journal of Aerosol Science* **19**, 159–166 (1988). <http://www.sciencedirect.com/science/article/pii/0021850288902194>.
- [47] SPECS. Leading Scientific Equipment for Surface Analysis. <https://www.specs-group.com/>.
- [48] WITec. WITec Raman Imaging. <https://www.witec.de/>.
- [49] Sojka, F., Meissner, M., Zwick, C., Forker, R. & Fritz, T. Determination and correction of distortions and systematic errors in low-energy electron diffraction. *Review of Scientific Instruments* **84**, 015111 (2013). <https://aip.scitation.org/doi/10.1063/1.4774110>.
- [50] Bauer, E. Low energy electron microscopy. *Reports on Progress in Physics* **57**, 895–938 (1994). <https://doi.org/10.1088/0034-4885/57/9/002>.
- [51] Havstad, M. A., Schilbach, M. A. & McLean, W. I. The optical constants and spectral specular reflectivity of highly oriented pyrolytic graphite (HOPG). Revision 1. Tech. Rep., Lawrence Livermore National Lab., CA (United States) (1993).

- [52] Qian, X., Ding, Z., Shin, J., Schmidt, A. J. & Chen, G. Accurate measurement of in-plane thermal conductivity of layered materials without metal film transducer using frequency domain thermoreflectance. *Review of Scientific Instruments* **91**, 064903 (2020). <https://aip.scitation.org/doi/10.1063/5.0003770>.
- [53] Tompkins, H. G. & Hilfiker, J. N. *Spectroscopic Ellipsometry: Practical Application to Thin Film Characterization* (Momentum Press, 2016).
- [54] Solonenko, D., Selyshchev, O., Zahn, D. R. T. & Vogt, P. Oxidation of Epitaxial Silicene on ag(111). *physica status solidi (b)* **256**, 1800432 (2019). <https://onlinelibrary.wiley.com/doi/abs/10.1002/pssb.201800432>.
- [55] Bunch, J. S., Verbridge, S. S. & Alden, J. S. Impermeable Atomic Membranes from Graphene Sheets. *Nano Lett.* **8**, 5 (2008).
- [56] Gupta, V., Kumar, A. & Ray, N. Rapid communication: Permeability of hydrogen in two-dimensional graphene and hexagonal boron nitride sheets. *Pramana* **91**, 64 (2018). <https://doi.org/10.1007/s12043-018-1638-6>.
- [57] Azeem, M., Jan, R., Farrukh, S. & Hussain, A. Improving gas barrier properties with boron nitride nanosheets in polymer-composites. *Results in Physics* **12**, 1535–1541 (2019). <http://www.sciencedirect.com/science/article/pii/S2211379718327323>.
- [58] Wei, J., Vo, T. & Inam, F. Epoxy/graphene nanocomposites – processing and properties: a review. *RSC Advances* **5**, 73510–73524 (2015). <https://pubs.rsc.org/en/content/articlelanding/2015/ra/c5ra13897c>.
- [59] NASA. Outgassing Data for Selecting Spacecraft Materials System. <https://outgassing.nasa.gov/>.
- [60] Moras, P., Menten, T. O., Sheverdyeva, P. M., Locatelli, A. & Carbone, C. Coexistence of multiple silicene phases in silicon grown on Ag(1 1 1). *Journal of Physics: Condensed Matter* **26**, 185001 (2014). <https://iopscience.iop.org/article/10.1088/0953-8984/26/18/185001/meta>.
- [61] Oura, K., Katayama, M., Zotov, A. V., Lifshits, V. G. & Saranin, A. A. Surface Analysis I. Diffraction Methods. In Oura, K., Katayama, M., Zotov, A. V., Lifshits, V. G. & Saranin, A. A. (eds.) *Surface Science: An Introduction*, Advanced Texts in Physics, 47–75 (Springer, Berlin, Heidelberg, 2003). https://doi.org/10.1007/978-3-662-05179-5_4.
- [62] Jamgotchian, H. *et al.* Silicene on ag(111) : domains and local defects of the observed superstructures. *Journal of Physics: Conference Series* **491**, 012001 (2014). <https://doi.org/10.1088%2F1742-6596%2F491%2F1%2F012001>.
- [63] Petrović, M., Hoegen, M. H.-v. & Meyer zu Heringdorf, F.-J. Equilibrium shape of single-layer hexagonal boron nitride islands on iridium. *Scientific Reports* **9**, 19553 (2019). <https://www.nature.com/articles/s41598-019-56000-1>.

- [64] Peimyoo, N. *et al.* Nonblinking, Intense Two-Dimensional Light Emitter: Monolayer WS₂ Triangles. *ACS Nano* **7**, 10985–10994 (2013). <https://pubs.acs.org/doi/10.1021/nm4046002>.
- [65] Kamal, C., Chakrabarti, A., Banerjee, A. & Deb, S. K. Silicene beyond monolayers—different stacking configurations and their properties. *Journal of Physics: Condensed Matter* **25**, 085508 (2013). <https://doi.org/10.1088/20953-8984/25/25/2F085508>.
- [66] Padova, P. D. *et al.* Evidence of Dirac fermions in multilayer silicene. *Applied Physics Letters* **102**, 163106 (2013). <https://aip.scitation.org/doi/abs/10.1063/1.4802782>.
- [67] Salomon, E., Ajjouri, R. E., Lay, G. L. & Angot, T. Growth and structural properties of silicene at multilayer coverage. *Journal of Physics: Condensed Matter* **26**, 185003 (2014). <https://doi.org/10.1088/20953-8984/26/26/2F185003>.
- [68] Resta, A. *et al.* Atomic Structures of Silicene Layers Grown on ag(111): Scanning Tunneling Microscopy and Noncontact Atomic Force Microscopy Observations. *Scientific Reports* **3**, 2399 (2013). <https://www.nature.com/articles/srep02399>.
- [69] Cahangirov, S. *et al.* Atomic structure of the $\sqrt{3} \times \sqrt{3}$ phase of silicene on ag(111). *Physical Review B* **90**, 035448 (2014). <https://link.aps.org/doi/10.1103/PhysRevB.90.035448>.
- [70] Kaltsas, D. & Tsetseris, L. Stability and electronic properties of ultrathin films of silicon and germanium. *Physical Chemistry Chemical Physics* **15**, 9710–9715 (2013). <https://pubs.rsc.org/en/content/articlelanding/2013/cp/c3cp50944c>.
- [71] Özçelik, V. O. & Ciraci, S. Local Reconstructions of Silicene Induced by Adatoms. *The Journal of Physical Chemistry C* **117**, 26305–26315 (2013). <https://doi.org/10.1021/jp408647t>.
- [72] Shirai, T. *et al.* Structure determination of multilayer silicene grown on ag(111) films by electron diffraction: Evidence for Ag segregation at the surface. *Physical Review B* **89**, 241403 (2014). <https://link.aps.org/doi/10.1103/PhysRevB.89.241403>.
- [73] Kawahara, K. *et al.* Atomic structure of “multilayer silicene” grown on ag(111): Dynamical low energy electron diffraction analysis. *Surface Science* **651**, 70–75 (2016). <http://www.sciencedirect.com/science/article/pii/S0039602816300462>.
- [74] De Padova, P. *et al.* Multilayer silicene: clear evidence. *2D Materials* **3**, 031011 (2016). <https://iopscience.iop.org/article/10.1088/2053-1583/3/3/031011>.
- [75] Acun, A., Poelsema, B., Zandvliet, H. J. W. & van Gastel, R. The instability of silicene on ag(111). *Applied Physics Letters* **103**, 263119 (2013). <https://aip.scitation.org/doi/full/10.1063/1.4860964>.

- [76] Bringans, R. D., Olmstead, M. A., Uhrberg, R. I. G. & Bachrach, R. Z. Interface formation of GaAs with Si(100), Si(111), and Ge(111): Core-level spectroscopy for monolayer coverages of GaAs, Ga, and As. *Physical Review B* **36**, 9569–9580 (1987). <https://link.aps.org/doi/10.1103/PhysRevB.36.9569>.
- [77] Hesse, R., Weiß, M., Szargan, R., Streubel, P. & Denecke, R. Improved peak-fit procedure for XPS measurements of inhomogeneous samples—Development of the advanced Tougaard background method. *Journal of Electron Spectroscopy and Related Phenomena* **205**, 29–51 (2015). <http://www.sciencedirect.com/science/article/pii/S0368204815001437>.
- [78] Molle, A. *et al.* Hindering the Oxidation of Silicene with Non-Reactive Encapsulation. *Advanced Functional Materials* **23**, 4340–4344 (2013). <https://www.onlinelibrary.wiley.com/doi/abs/10.1002/adfm.201300354>.
- [79] Díaz, J., Paolicelli, G., Ferrer, S. & Comin, F. Separation of the sp³ and sp² components in the C1 *s* photoemission spectra of amorphous carbon films. *Physical Review B* **54**, 8064–8069 (1996). <https://link.aps.org/doi/10.1103/PhysRevB.54.8064>.
- [80] Tsoutsou, D., Xenogiannopoulou, E., Golias, E., Tsipas, P. & Dimoulas, A. Evidence for hybrid surface metallic band in 4 x 4 silicene on ag(111). *Applied Physics Letters* **103**, 231604 (2013). <https://aip.scitation.org/doi/10.1063/1.4841335>.
- [81] Cahangirov, S. *et al.* Electronic structure of silicene on ag(111): Strong hybridization effects. *Physical Review B* **88**, 035432 (2013). <https://link.aps.org/doi/10.1103/PhysRevB.88.035432>.
- [82] Yan, J.-A., Stein, R., Schaefer, D. M., Wang, X.-Q. & Chou, M. Y. Electron-phonon coupling in two-dimensional silicene and germanene. *Physical Review B* **88**, 121403 (2013). <https://link.aps.org/doi/10.1103/PhysRevB.88.121403>.
- [83] Gori, P., Pulci, O., Vollaro, R. d. L. & Guattari, C. Thermophysical Properties of the Novel 2D Materials Graphene and Silicene: Insights from Ab-initio Calculations. *Energy Procedia* **45**, 512–517 (2014). <http://www.sciencedirect.com/science/article/pii/S1876610214000563>.
- [84] Solonenko, D. *et al.* 2d vibrational properties of epitaxial silicene on ag(111). *2D Materials* **4**, 015008 (2016). <https://doi.org/10.1088%2F2053-1583%2F4%2F1%2F015008>.
- [85] Aroyo, M. I. *et al.* Bilbao Crystallographic Server: I. Databases and crystallographic computing programs. *Zeitschrift für Kristallographie - Crystalline Materials* **221**, 15–27 (2006). <https://www.degruyter.com/view/journals/zkri/221/1/article-p15.xml>.
- [86] Curcella, A. *et al.* Multilayer silicene: clear evidence of Ag-terminated bulk silicon. *2D Materials* **4**, 025067 (2017). <https://doi.org/10.1088%2F2053-1583%2F4%2F025067>.

- [87] Stpniak-Dybala, A. *et al.* Planar Silicene: A New Silicon Allotrope Epitaxially Grown by Segregation. *Advanced Functional Materials* **29**, 1906053 (2019). <https://onlinelibrary.wiley.com/doi/abs/10.1002/adfm.201906053>.
- [88] Sadeddine, S. *et al.* Compelling experimental evidence of a Dirac cone in the electronic structure of a 2D Silicon layer. *Scientific Reports* **7**, 44400 (2017). <https://www.nature.com/articles/srep44400>.
- [89] Shpyrko, O. G. *et al.* Crystalline surface phases of the liquid Au-Si eutectic alloy. *Physical Review B* **76**, 245436 (2007). <https://link.aps.org/doi/10.1103/PhysRevB.76.245436>.
- [90] Shpyrko, O. G. *et al.* Surface Crystallization in a Liquid AuSi Alloy. *Science* **313**, 77–80 (2006). <https://science.sciencemag.org/content/313/5783/77>.
- [91] Kaloni, T. P., Cheng, Y. C. & Schwingenschlögl, U. Hole doped Dirac states in silicene by biaxial tensile strain. *Journal of Applied Physics* **113**, 104305 (2013). <https://aip.scitation.org/doi/10.1063/1.4794812>.
- [92] Ashtikar, M. S. & Sharma, G. L. Structural Investigation of Gold Induced Crystallization in Hydrogenated Amorphous Silicon Thin Films. *Japanese Journal of Applied Physics* **34**, 5520 (1995). <https://iopscience.iop.org/article/10.1143/JJAP.34.5520/meta>.
- [93] Angel, R. J., Murri, M., Mihailova, B. & Alvaro, M. Stress, strain and Raman shifts. *Zeitschrift für Kristallographie - Crystalline Materials* **234**, 129–140 (2019). <https://www.degruyter.com/view/journals/zkri/234/2/article-p129.xml>.
- [94] Gonze, X. *et al.* Recent developments in the ABINIT software package. *Computer Physics Communications* **205**, 106–131 (2016). <http://www.sciencedirect.com/science/article/pii/S0010465516300923>.
- [95] Gonze, X. & Vigneron, J.-P. Density-functional approach to nonlinear-response coefficients of solids. *Physical Review B* **39**, 13120–13128 (1989). <https://link.aps.org/doi/10.1103/PhysRevB.39.13120>.
- [96] Baroni, S., de Gironcoli, S., Dal Corso, A. & Giannozzi, P. Phonons and related crystal properties from density-functional perturbation theory. *Reviews of Modern Physics* **73**, 515–562 (2001). <https://link.aps.org/doi/10.1103/RevModPhys.73.515>.
- [97] Caldwell, W. B. *et al.* Self-Assembled Monolayers of Ferrocenylazobenzenes on Au(111)/Mica Films: Surface-Enhanced Raman Scattering Response vs Surface Morphology. *Langmuir* **10**, 4109–4115 (1994). <https://doi.org/10.1021/la00023a034>.
- [98] Lombardi, J. R. & Birke, R. L. A Unified Approach to Surface-Enhanced Raman Spectroscopy. *The Journal of Physical Chemistry C* **112**, 5605–5617 (2008). <https://doi.org/10.1021/jp800167v>.

- [99] Mohiuddin, T. M. G. *et al.* Uniaxial strain in graphene by Raman spectroscopy: G peak splitting, Grüneisen parameters, and sample orientation. *Physical Review B* **79**, 205433 (2009). <https://link.aps.org/doi/10.1103/PhysRevB.79.205433>.
- [100] Hanke, F. & Björk, J. Structure and local reactivity of the Au(111) surface reconstruction. *Physical Review B* **87**, 235422 (2013). <https://link.aps.org/doi/10.1103/PhysRevB.87.235422>.
- [101] Blume, R. *et al.* Characterizing Graphitic Carbon with X-ray Photoelectron Spectroscopy: A Step-by-Step Approach. *ChemCatChem* **7**, 2871–2881 (2015). <https://chemistry-europe.onlinelibrary.wiley.com/doi/abs/10.1002/cctc.201500344>.
- [102] Knox, K. R. *et al.* Spectromicroscopy of single and multilayer graphene supported by a weakly interacting substrate. *Physical Review B* **78**, 201408 (2008). <https://link.aps.org/doi/10.1103/PhysRevB.78.201408>.
- [103] Hayes, W. *Crystals with the fluorite structure - electronic, vibrational and defect properties* (Clarendon Press, Oxford, 1974). <https://www.sciencedirect.com/science/article/abs/pii/0022286076800646?via%3Dihub>.
- [104] Sugiyama, M. & Oshima, M. MBE growth of fluorides. *Microelectronics Journal* **27**, 361–382 (1996). <http://www.sciencedirect.com/science/article/pii/0026269295000623>.
- [105] Illarionov, Y. Y., Vexler, M. I., Fedorov, V. V., Sutturin, S. M. & Sokolov, N. S. Electrical and optical characterization of Au/CaF₂/p-Si(111) tunnel-injection diodes. *Journal of Applied Physics* **115**, 223706 (2014). <https://aip.scitation.org/doi/10.1063/1.4882375>.
- [106] Foster, A. S., Trevethan, T. & Shluger, A. L. Structure and diffusion of intrinsic defects, adsorbed hydrogen, and water molecules at the surface of alkali-earth fluorides calculated using density functional theory. *Physical Review B* **80**, 115421 (2009). <https://link.aps.org/doi/10.1103/PhysRevB.80.115421>.
- [107] Illarionov, Y. Y. *et al.* Ultrathin calcium fluoride insulators for two-dimensional field-effect transistors. *Nature Electronics* **2**, 230–235 (2019). <https://www.nature.com/articles/s41928-019-0256-8>.
- [108] Vexler, M. I. *et al.* Electrical characterization and modeling of the Au/CaF₂/nSi(111) structures with high-quality tunnel-thin fluoride layer. *Journal of Applied Physics* **105**, 083716 (2009). <https://aip.scitation.org/doi/10.1063/1.3110066>.
- [109] Boschker, J. E. *et al.* Coincident-site lattice matching during van der Waals epitaxy. *Scientific Reports* **5**, 18079 (2015). <https://www.nature.com/articles/srep18079>.
- [110] Himpsel, F. J. *et al.* Structure and bonding at the CaF₂/Si(111) interface. *Applied Physics Letters* **48**, 596–598 (1986). <https://aip.scitation.org/doi/10.1063/1.96478>.

- [111] Yeh, J. J. & Lindau, I. Atomic subshell photoionization cross sections and asymmetry parameters: $1 < z < 103$. *Atomic Data and Nuclear Data Tables* **32**, 1–155 (1985). <http://www.sciencedirect.com/science/article/pii/0092640X85900166>.
- [112] Umbach, E., Sokolowski, M. & Fink, R. Substrate-interaction, long-range order, and epitaxy of large organic adsorbates. *Applied Physics A* **63**, 565–576 (1996). <https://doi.org/10.1007/BF01567212>.
- [113] Karlsson, U. O., Himpsel, F. J., Morar, J. F., Rieger, D. & Yarmoff, J. A. Electronic structure of molecular beam epitaxy grown CaF₂ on Si(111). *Journal of Vacuum Science & Technology B: Microelectronics Processing and Phenomena* **4**, 1117 (1998). <https://avs.scitation.org/doi/abs/10.1116/1.583552>.
- [114] Pasquali, L. *et al.* Electronic properties of CaF₂ nanodimensional islands on Si(001): An MDS and UPS study. *Nuclear Instruments and Methods in Physics Research Section B: Beam Interactions with Materials and Atoms* **193**, 474–479 (2002). <http://www.sciencedirect.com/science/article/pii/S0168583X02008236>.
- [115] Arguilla, M. Q. *et al.* Optical properties and Raman-active phonon modes of two-dimensional honeycomb Zintl phases. *Journal of Materials Chemistry C* **5**, 11259–11266 (2017). <http://xlink.rsc.org/?DOI=C7TC01907F>.
- [116] Bruggeman, D. a. G. Berechnung verschiedener physikalischer Konstanten von heterogenen Substanzen. I. Dielektrizitätskonstanten und Leitfähigkeiten der Mischkörper aus isotropen Substanzen. *Annalen der Physik* **416**, 636–664 (1935). <https://onlinelibrary.wiley.com/doi/abs/10.1002/andp.19354160705>.
- [117] Rivory, J. *et al.* Study of CaF₂ growth on Si, a-Si O₂ by in-situ spectroscopic ellipsometry. *Thin Solid Films* **233**, 260–263 (1993). <http://www.sciencedirect.com/science/article/pii/004060909390103V>.
- [118] Aspnes, D. E. & Studna, A. A. Dielectric functions and optical parameters of Si, Ge, GaP, GaAs, GaSb, InP, InAs, and InSb from 1.5 to 6.0 eV. *Physical Review B* **27**, 985–1009 (1983). <https://link.aps.org/doi/10.1103/PhysRevB.27.985>.
- [119] Pierce, D. T. & Spicer, W. E. Electronic Structure of Amorphous Si from Photoemission and Optical Studies. *Physical Review B* **5**, 3017–3029 (1972). <https://link.aps.org/doi/10.1103/PhysRevB.5.3017>.
- [120] Bechstedt, F., Matthes, L., Gori, P. & Pulci, O. Infrared absorbance of silicene and germanene. *Applied Physics Letters* **100**, 261906 (2012). <http://aip.scitation.org/doi/10.1063/1.4731626>.

Curriculum Vitae

Daniele Nazzari, M.Sc.

Address: Vogelsanggasse 34A, 1050 Wien, Austria

Birth date: 21.04.1991

Email: daniele.nazzari@tuwien.ac.at

Education

2017 – 2021 PhD in Electrical Engineering

Center for Micro and Nanostructures

TU Wien, Vienna, Austria

Supervisor: Ao. Univ.Prof.Dr. Alois Lugstein

e-mail: alois.lugstein@tuwien.ac.at

Project: Growth of 2D silicon structures by molecular beam epitaxy

2014 – 2017 Master Degree in Physics

University of Milan, Milan, Italy

Supervisor: Dr. Michele Perego (IMM CNR)

e-mail: michele.perego@mdm.imm.cnr.it

Project: Inorganic nanostructures via sequential infiltration synthesis in self-assembled block copolymers templates

2010 – 2014 Bachelor Degree in Physics

University of Milan, Milan, Italy

Project: Realisation and characterisation of deformable optical devices

Employment

Since 2017 Project assistant

Center for Micro and Nanostructures

TU Wien, Vienna, Austria

List of Publications

2019 V. Ritter*, J. Genser*, **D. Nazzari***, O. Bethge, E. Bertagnolli and A. Lugstein – Silicene Passivation by Few-Layer Graphene - *ACS Applied Materials & Interfaces*
(* These authors contributed equally)

F. E. Caligiore, **D. Nazzari**, E. Cianci, K. Sparnacci, M. Laus, M. Perego, G. Seguini – Effect of the Density of Reactive Sites in P(S-r-MMA) Film during Al₂O₃ Growth by Sequential Infiltration Synthesis - *Advanced Materials Interfaces*

2018 E. Cianci, **D. Nazzari**, G. Seguini, M. Perego – Trimethylaluminum Diffusion in PMMA Thin Films during Sequential Infiltration Synthesis: In Situ Dynamic Spectroscopic Ellipsometric Investigation – *Advanced Materials Interfaces*

2017 M.A.C. Potenza, **D. Nazzari**, L. Cremonesi, I. Denti and P. Milani - Hyperspectral imaging with deformable gratings fabricated with metal-elastomer nanocomposites - *Review of Scientific Instruments*